

BOSTON UNIVERSITY
GRADUATE SCHOOL OF ARTS AND SCIENCES

Thesis

**CHARACTERISING THE SPATIAL VARIABILITY OF ALBEDO
IN A SEMI-DESERT LANDSCAPE FOR THE VALIDATION OF
SATELLITE DATA**

by

ANDREW H. HYMAN

BSc, University College London (University of London), 1996

Submitted in partial fulfillment of the
requirements for the degree of
Master of Arts
1998

Approved by

First Reader

Alan H. Strahler, PhD
Professor of Geography

Second Reader

Wolfgang Lucht, PhD
Research Assistant Professor of Geography

Third Reader

Xiaowen Li, PhD
Research Professor of Geography

Acknowledgments

Numerous members of faculty and fellow graduate students in the Department of Geography / Center for Remote Sensing at Boston University have provided invaluable support. In particular I would like to thank my committee Professor Alan Strahler, Dr Wolfgang Lucht and Dr Xiaowen Li.

This study would also not have been possible without the collaboration with Professor Mike Barnsley and Paul Hobson (University of Wales, Swansea) and Professor Jan-Peter Muller (University College London) and the assistance of various EOS personnel, in particular Dr Jeff Privette (NASA Goddard Space Flight Center), Dr Jim Conel and Dr Mark Helmlinger (NASA Jet Propulsion Laboratory), Dr Kurt Thome (University of Arizona) and Dr Gregory Asner (University of Colorado). I am especially grateful to Dr Thomas Schmugge (USDA / ARS Hydrology Laboratory) who spoke with me following a presentation at the American Geophysical Union Spring Meeting in Boston and as a result provided additional imagery which proved key to overcoming limitations with other data sources. Dr Marc Leroy (CNES) kindly facilitated provision of POLDER data.

Considerable thanks are due to Dr Mark Friedl and Dr Ray Dezzani (BU) and Professor Ralph D'Agastino (Department of Mathematics) for fielding a deluge of statistics questions and to my parents for their support and assistance. As ever, Jordan Borak provided his usual pearls of wisdom and thanks are also due to Dr Crystal Schaaf, Dr Trevor Tsang, Tony Soares, Nick Strugnell, John Hodges (BU) and Dr Philip Lewis and Mat Disney (UCL).

This research was funded under a NASA MODIS grant to Professor Alan Strahler, NAS 5-31369.

Attendance to present results from this study at IGARSS98, Seattle, WA, was also partially supported by a travel bursary from The Remote Sensing Society.

CHARACTERISING THE SPATIAL VARIABILITY OF ALBEDO IN A SEMI-DESERT LANDSCAPE FOR THE VALIDATION OF SATELLITE DATA

ANDREW H. HYMAN

ABSTRACT

This study describes data collection and analysis for Grassland PROVE, a pre-launch EOS field experiment in May 1997 at Jornada, NM. Firstly, I present linear mixture models relating ground based total shortwave and NIR albedometer measurements to scene elements derived from classified hemispherical photography for 44 sites on transects around the validation tower. Key factors that may bias analysis and require correction are soil moisture and solar zenith angle. Secondly, I use ground measurements to devise strategies for validating measurements acquired at the spatial scale of AVHRR and POLDER, one aspect of which is also narrowband to broadband albedo conversion. Ground based albedo estimates meet the ± 0.05 accuracy requirement for global climate modelling suggested by Henderson-Sellers and Wilson (1983) and are close to the ± 0.02 standard suggested by Sellers (1993). Through spatial modelling based on assigning typical albedos to classes derived through classification of 12 m resolution TMS data over the 1.1 km x 1.1 km area of an AVHRR pixel, it is shown quantitatively that the tower was, by chance, located in an area where heterogeneity is similar to that at a coarser resolution. Spatial modelling through classification is advised at other locations. These results provide the first step in establishing appropriate strategies for albedo validation for MODIS.

Table of Contents

[illegible]

4.1.2.	Hemispherical photography	25
4.1.3.	Ancillary field measurements	26
4.1.3.1.	GPS measurements	26
4.1.3.2.	Atmospheric characterisation	27
4.2.	Remote Sensing Data	27
4.2.1.	LANDSAT TM (Level 9)	27
4.2.2.	AVIRIS	28
4.2.3.	Daedalus AADS-1268 Thematic Mapper Simulator	29
4.2.4.	NOAA AVHRR	29
4.2.5.	POLDER	32
5.	Data Processing Methodology	37
5.1.	Hemispherical Photography Classification	37
5.2.	BRDF Model Description	41
5.3.	Derivation of Broadband Albedo from Narrow Band Measurements	42
5.3.1.	Theoretical basis	42
5.3.2.	Implementation	45
6.	Results and Discussion	51
6.1.	Assessing the Spatial Variability Using Ground Measurements	51
6.1.1.	Qualitative Evaluation	51
6.1.1.1.	Correction for Soil Moisture Effects	53
6.1.2.	Quantitative Evaluation	54
6.2.	Deriving albedo at satellite spatial scale	60
6.2.1.	AVHRR 1.1km broadband albedo through narrowband to broadband albedo conversion	60

6.2.1.1. AVHRR 1.1km broadband albedo values and comparison to mean of transect measurements	60
6.2.1.2. Spatial modelling of albedo at coarse resolution from ground measurements through land cover classification and comparison to AVHRR derived values	62
6.2.2. 10 x 10 AVHRR broadband albedo map	65
6.2.3. PODLER broadband albedo through narrowband to broadband conversion	67
6.2.4. Summary: multiple scale albedo comparison	69
7. Conclusions and Lessons Learned	78
Appendix A: Figures	84
References	111

List of Tables

Table 1.1: MODLAND Hierarchical Test Site Scheme	5
Table 4.1: Spatial response of the albedometer	35
Table 4.2: Waveband characteristics of the Daedalus AADS-1268 Thematic Mapper Simulator	36
Table 6.1: Regression model coefficients using albedo values without corrections for either solar zenith angle or soil moisture effects	73
Table 6.2: Regression model coefficients using albedo values corrected for solar zenith angle effects,, but not for soil moisture effects	73
Table 6.3: Regression model coefficients using albedo values corrected for solar zenith angle and soil moisture effects	73
Table 6.4: Observed and predicted total shortwave and NIR broadband albedo for seven sites at the end of the long east transect	74
Table 6.5: Comparison of mean broadband albedo from the 44 transect sample sites and broadband albedos derived from AVHRR for the pixel containing the tower and those below, to the right and below right. Diffuse and direct irradiance used in the calculation of the AVHRR broadband albedos have been derived using the <i>high</i> aerosol optical thickness estimate	75
Table 6.6: Comparison of mean broadband albedo from the 44 transect sample sites and broadband albedos derived from AVHRR for the pixel containing the tower and those below, to the right and below right. Diffuse and direct irradiance used in the calculation of the AVHRR broadband albedos have been derived using a <i>low</i> aerosol optical thickness estimate	75

Table 6.7: Proportional cover of three land cover classes and broadband albedo values calculated using the land cover classification method for nine 1.1.km x 1.1km cells within a 2.2km x 2.2km area centred on the AVHRR pixel containing the tower at the transition site	76
Table 6.8: Typical albedo values assumed to characterise the three land cover classes used to derive broadband albedo at the satellite scale using the land cover classification approach	76
Table 6.9: Summary broadband albedo statistics for the values derived from land cover classification for the 9 1.1km x 1.1km cells extracted from the TMS data	76
Table 6.10: Broadband albedo generated for the POLDER pixel containing the tower at the transitional site with atmospheric characterisation for low and high aerosol optical thickness	77
Table 6.11: Broadband albedo generated for the 10x10 AVHRR grid	77
Table 6.12: Broadband albedo generated for the POLDER pixel by constraining the AVIRIS reflectance curve for low and high aerosol optical thickness conditions	77

List of Figures

Figure 1.1: Schematic illustrating the continuous flux tower instrumentation that is planned for most Core Validation Test Sites and the periodic but less frequent transect sampling.....	84
Figure 2.1: Diurnal variation in albedo over four surfaces at two sites in south-western Niger	85
Figure 3.1: Location of Jornada Experimental Range (JRN)	86
Figure 3.2a: View of the study site from the top of the transitional tower with the dirt road running north into the photograph	87
Figure 3.2b: View of the study site from the top of the transitional tower with the dirt road running south into the photograph	87
Figure 3.2c: View of the study site from the top of the tower looking to the south west	88
Figure 3.3: False colour composite derived from 4m resolution Thematic Mapper Simulator data using bands 7,5,3 (TM equivalent 4,3,2)	88
Figure 4.1: Spatial response function of albedometer with respect to a flat surface	89
Figure 4.2: Albedometer instrument setup	90
Figure 4.3: Derivation of solar zenith angle correction model by fitting a curve	91
Figure 4.4: Spatial response function of albedometer overlaid on a hemispherical photograph	92
Figure 5.1a: Hemispherical photograph (top) and classified image (bottom) of site 9 on the north transect which is characteristic of a high vegetation location	93
Figure 5.1b: Hemispherical photograph (top) and classified image (bottom) of site 6 on the north transect which is characteristic of a low green live vegetation location	94

Figure 5.2: Four different types of projection that characterise fisheye lenses	95
Figure 5.3: Plot of radial distance measured using high accuracy surveying equipment against distance derived from a hemispherical photograph for a camera calibration rig	96
Figure 5.4: Definition of terms used in the derivation of the equation to determine R_{180} , the radius of the hemisphere / scene measured in pixels on a hemispherical photograph for a lens with a 180° FOV	97
Figure 5.5: Simplified spectral reflectance curves for (a) vegetation and (b) non-vegetation surface showing location of LANDSAT bands and proportional weighting factors	98
Figure 5.6: Reflectance spectra for mesquite live vegetation (mesquite) and soil recorded by Greg Asner (University of Colorado) using an ASD Fieldspec® FR Portable Spectroradiometer	99
Figure 6.1: Total shortwave and NIR broadband, solar zenith angle corrected, albedo measurements along the north transect for the 22 nd , 23 rd and 26 th May 1997	100
Figure 6.2a: Total shortwave and NIR broadband albedo measurements without solar zenith angle correction along the grassland transect for three times on 27 th May 1997	101
Figure 6.2b: Total shortwave and NIR broadband, solar zenith angle corrected, albedo measurements along the grassland transect for three times on 27 th May 1997	101
Figure 6.3a: Observed versus predicted total shortwave broadband albedo for data without either solar zenith angle or soil moisture corrections applied	102
Figure 6.3b: Observed versus predicted total shortwave broadband albedo for data with corrections applied for solar zenith angle effects, but not for the influence of soil moisture	102
Figure 6.3c: Observed versus predicted total shortwave broadband albedo for data with corrections for both solar zenith angle and soil moisture effects	102

Figure 6.4a: Observed versus predicted NIR broadband albedo for data without either solar zenith angle or soil moisture corrections applied	103
Figure 6.4b: Observed versus predicted NIR broadband albedo for data with corrections applied for solar zenith angle effects, but not for the influence of soil moisture	103
Figure 6.4c: Observed versus predicted NIR broadband albedo for data with corrections for both solar zenith angle and soil moisture effects	103
Figure 6.5: Observed and predicted values of total shortwave and NIR broadband albedo for seven locations at the end of a 1km transect to the east of the tower	104
Figure 6.6: Identification of numbering of the nine 1.1km x 1.1km cells within a larger 2.2km x 2.2km area centered on the AVHRR pixel containing the tower. Cells are numbered at the upper left.	105
Figure 6.7: Classified 2.2km x 2.2km area centered on the AVHRR pixel containing the tower. The classification is performed on 12m resolution TMS data. The three classes are: blue: shrubs and soil, red: grass, yellow: grass and soil	106
Figure 6.8: 10 x 10 1.1km x 1.1km AVHRR total shortwave broadband albedo map	107
Figure 6.9: LANDSAT TM histogram equalised band 4,5,3 false colour composite with 1.1km AVHRR grid overlayed	108
Figure 6.10: Summary graph of total shortwave broadband albedo values at various spatial scales	109
Figure 6.11: Total shortwave, visible and near-infrared values at various spatial scales	110

List of Abbreviations / Acronyms

5S	Simulation of the Satellite Signal in the Solar Spectrum
6S	Second Simulation of the Satellite Signal in the Solar Spectrum
AERONET	Aerosol Robotic Network
AMBRALS	Algorithm for MODIS Bidirectional Reflectance Anisotropy of the Land Surface
ARM	Atmospheric Radiation Measurement (DOE program)
ARS	Agricultural Research Service
ASAS	Advanced Solid State Array Spectroradiometer
ASD	Analytical Spectral Devices, Inc.
ASTER	Advanced Spaceborne Thermal Emission and Reflection Radiometer
ATBD	Algorithm Theoretical Basis Document
ATM	Airborne Thematic Mapper
AVHRR	Advanced Very High Resolution Radiometer
AVIRIS	Airborne Visible/Infrared Imaging Spectrometer
BOREAS	Boreal Ecosystem-Atmosphere Study
BSRN	Baseline Surface Radiation Network
BU	Boston University
CART	Cloud and Radiation Testbed
CMDL	Climate Monitoring and Diagnostics Laboratory
DoE	United States Department of Energy
EDT	Eastern Daylight Savings Time

BRDF	Bidirectional Reflectance Distribution Function
CAGE	Civil, Agricultural, and Geological Engineering
CCAR	Colorado Center for Astrodynamics Research
CIA	Central Intelligence Agency
CNES	Centre National d'Etudes Spatiales
CU	University of Colorado
DAAC	Distributed Active Archive Center
EOS	Earth Observing System
EROS	Earth Resources Observation System
EXACT	Exact Atmospheric Correction Technique
FAPAR	Fraction of Absorbed Photosynthetically Active Radiation
FIFE	First ISLSCP Field Experiment
FOV	Field of View
GCM	Global Climate Model
GOES	Geostationary Operational Environmental Satellite
GPS	Global Positioning System
GMT	Greenwich Mean Time
GSFC	Goddard Space Flight Center
HAPEX	Hydrological - Atmospheric Pilot Experiment
IDS	Interdisciplinary Science
IFOV	Instantaneous Field of View
IGARSS	International Geoscience and Remote Sensing Symposium
IPW	Image Processing Workbench

ISLSCP	International Satellite Land-Surface Climatology Project
JPL	Jet Propulsion Laboratory
LAC	Local Area Coverage
LAI	Leaf Area Index
LANDSAT TM	Land Remote-Sensing Satellite Thematic Mapper
LBA	Large Scale Biosphere-Atmosphere Experiment
LTER	Long-Term Ecological Research
MDT	Mountain Daylight Savings Time
MIR	Mid-Infrared
MISR	Multi-angle Imaging Spectroradiometer
MODLAND	MODIS Land
NASA	National Aeronautics and Space Administration
NIR	Near-Infrared
NLAPS	National LANDSAT Archive Production System
NMSU	New Mexico State University
NOAA	National Oceanic and Atmospheric Administration
ORNL	Oak Ridge National Laboratory
NPP	Net Primary Production
PARABOLA	Portable Apparatus for Rapid Acquisition of Bidirectional Observations of Land and Atmosphere
POLDER	Polarization and Directionality of Earth's Reflectances
RMSE	Root Mean Square Error
rps	Revolutions per Second

SAFARI	South African Fire-Atmosphere Research Initiative
S/A	Selective Availability
SEBEX	Sahelian Energy Balance Experiment
SURFRAD	Surface Radiation Budget Network
TOA	Top of the Atmosphere
TMS	Thematic Mapper Simulator
TRACE-A	Transport and Atmospheric Chemistry near the Equator-Atlantic
UCL	University College London
URL	Uniform Resource Locator
USDA	United States Department of Agriculture
UTM	Universal Transverse Mercator
WMO	World Meteorological Organization

1. INTRODUCTION

1.1 MODIS Land Validation

The first platform, AM-1, of NASA's Earth Observing System (EOS) is slated for launch in 1999. A number of sensors will be carried onboard this platform including the Moderate Resolution Imaging Spectroradiometer (MODIS). For studies of the land surface, the MODIS Land (MODLAND) Science Team is producing a suite of science data products, namely: surface reflectance, land surface temperature, albedo / land surface bidirectional reflectance function (BRDF), vegetation indices, leaf area index (LAI) / fraction of photosynthetically active radiation (FPAR), fire, snow, lake, ice and sea cover, land cover / land cover change, and net photosynthesis / net primary production (NPP) (Justice *et al.*, 1998). A key scientific objective in the post-launch era, following initial sensor calibration, is validation of the data products by the MODLAND team (Privette *et al.*, 1997a).

The primary validation approach to ascertain the uncertainty inherent in MODLAND products will be based on comparisons with in-situ field data, with aircraft data and to data and products from other space-borne sensors (e.g. AVHRR, MISR). Provision of in-situ data will be via a hierarchical test site scheme as described in *table 1.1* (Privette *et al.*, 1997a). Primary validation is based on the Tier 3 and 4 sites equipped with continuous flux above-canopy instrumentation mounted on a fixed tower to provide both canopy scale radiometric and meteorological variables. In addition, measurements of LAI and FPAR along transects radiating from the tower are planned at less frequent temporal intervals. *Figure 1.1* provides a schematic illustration of the system (Privette *et al.*, 1997a).

As identified by Privette *et al.* (1997a), two primary challenges must be addressed in determining appropriate sampling strategies for validation. The key problem, aside from attaining adequate sampling of biophysical variables which exhibit spatial and temporal variance, is accurate measurement of these variables at the spatial scale of MODIS pixels which ranges from 250m-1km at nadir depending on the waveband. This necessitates use of globally distributed test sites and identification of strategies to synergize ground-based point measurements with higher resolution aircraft data (e.g. TM, AVIRIS) and to spatially scale data and parameters to the coarser spatial resolution of MODIS.

MODLAND has co-ordinated a variety of pre-launch field campaigns. These include the Prototype Validation Exercises (PROVE) for evaluation of instrumentation and sampling strategies appropriate for validation of remote sensing products derived at satellite spatial resolutions, prototyping of remote sensing algorithms, and interdisciplinary co-ordination at proposed global validation test sites (Kannenbergh, 1997; Privette *et al.*, 1997a). Two experiments were undertaken during 1997, Grassland PROVE and Forest PROVE, of which the former is the focus of interest in this study. More than 40 MODIS, MISR, ASTER, USDA-ARS, LTER, AERONET, EOS IDS, ORNL DAAC, POLDER, CU/CCAR researchers and personnel participated in data collection for Grassland PROVE. The Boston University team in collaboration with colleagues from University College London and University of Wales, Swansea collected measurements to address albedo related validation questions.

1.2 Study Objectives

In the context of MODIS validation, this study addresses two objectives. Firstly, field observations of the spatial variability of albedo in the semi-desert landscape at Jornada are evaluated. Models are formulated relating the total and NIR broadband albedo derived from the albedometers to the proportion of endmember scene element / land cover components at each sample site along five transects. Land cover component proportions are obtained through classification of coincident hemispherical photography. Through the analysis, a methodology is formulated for characterising the spatial variability of the landscape from point measurements including the identification of key factors that, unless accounted for, may introduce significant bias in scaling to coarser satellite spatial resolutions.

Secondly, albedo is derived at the 1.1km x 1.1km scale of AVHRR and at the 6km x 7km scale of POLDER through narrow to broadband albedo conversion to investigate techniques to scale ground measurements to coarser resolutions for satellite data product validation. Two methods are evaluated for deriving satellite scale albedo estimates from ground measurements. In the first instance, the mean of 44 ground based point measurements on four 100m transects to the north, south, east and west of the tower is calculated. In the second instance, the ground based albedo measurements are used to provide *typical* albedos for three land cover classes identified in the landscape. These typical albedo values are weighted by the proportional coverage of the land cover classes derived from an unsupervised classification of high resolution, 12m, Thematic Mapper Simulator data of a 1.1km x 1.1km area around the tower. The study evaluates a narrow to broadband albedo conversion scheme for AVHRR which is based on adjusting a high resolution AVIRIS reflectance profile by the red and NIR AVHRR spectral albedos which is then

weighted by downwelling solar irradiance. A 10 x 10 1.1km resolution broadband albedo map is then derived from AVHRR data to examine albedo variations and compared to the value calculated from POLDER. In deriving POLDER broadband albedo, the spectral albedo profile to be weighted by downwelling irradiance is derived both by splining the four spectral albedo values and, as for AVHRR, by adjusting the AVIRIS reflectance spectrum. The various methods and techniques at the different spatial scales and comparisons of values between scales are discussed and suggestions for developing a strategy for validation of the MODIS albedo product presented.

Grassland PROVE as the name indicates was a prototyping exercise. This study therefore concludes with a key lessons learned section which complements the description of methods, results and discussion in other sections by identifying and stressing factors that limited analysis and which require careful consideration for validation work in the EOS-era.

Table 1: MODLAND Hierarchical Test Site Scheme Source: Privette *et al.* (1997a)

	Tier	Approx. Number of Sites	Sample Area (km²)	Description of Instrumentation and Sampling	Example Sites/ Networks
1	Intensive Field Campaign Sites; International Field Campaign Programs	5	1,000	Intensive sampling of all relevant land and atmospheric parameters, including boundary layer gas exchange; often over land cover gradients	FIFE, BOREAS, HAPEX- Sahel, TRACE-A, SAFARI, LBA
2	Fully Instrumented Sites	5	100	Full suite of radiation and flux measurements; ground, tower and aircraft measurements	ARM/CART sites
3	Biome Tower Sites	20-30	100	Long term, select instrument packages for process studies; ground and tower measurements; all major ecosystems and climatic regions	Harvard Forest - Temperate Deciduous Forest Site
4	Globally Distributed Test Sites	60	25	Limited surface and atmosphere characterization; select instrument suites at different sites; widely distributed variable sampling frequencies (intermittent to continuous) capture seasonal or interannual variability, climatology; permanent sites	LTERS, NOAA CMDL, BSRN and SURFRAD networks
5	Instrument Calibration Sites	<5	10	Well-instrumented for vicarious calibration; unique reflectance and emittance properties of uniform, typically non-vegetated surfaces; ground and aircraft measurements may include geometric calibration site(s)	White Sands, Railroad Playa

2. BACKGROUND

2.1 *Albedo*

2.1.1 *Definitions of Albedo*

Spectral albedo is the dimensionless ratio of the solar radiation reflected by a surface in all directions within the surrounding hemisphere to the solar radiation incident on the surface given by:

$$\alpha(\Lambda) = \frac{E \uparrow (\Lambda)}{E \downarrow (\Lambda)} = \frac{\int_0^{2\pi} \int_0^{\pi/2} L \uparrow (\theta_v, \phi_v; \Lambda) \sin \theta_v \cos \theta_v d\theta_v d\phi_v}{\int_0^{2\pi} \int_0^{\pi/2} L \downarrow (\theta_i, \phi_i; \Lambda) \sin \theta_i \cos \theta_i d\theta_i d\phi_i} \quad (1)$$

where:

$\alpha(\lambda)$ is spectral albedo in a given waveband Λ ,

$\theta_i, \phi_i, \theta_v, \phi_v$ are illumination and view zenith and azimuth angles respectively,

$E \uparrow (\Lambda)$ is upwelling radiant energy flux from the surface in waveband Λ ,

$E \downarrow (\Lambda)$ is downwelling radiant energy flux in waveband Λ , which consists of both the direct (solar beam) and diffuse irradiance

$L \uparrow (\theta_v, \phi_v, \Lambda)$ is upwelling radiance in direction θ_v, ϕ_v in waveband Λ ,

$L \downarrow (\theta_i, \phi_i, \Lambda)$ is downwelling radiance in direction θ_i, ϕ_i in waveband Λ .

It is important to recognise that surface albedo is not an intrinsic property of the earth surface. Upwelling radiance is not just a function of the surface BRDF, but also of solar zenith angle and the angular distribution of downwelling irradiance which varies with atmospheric state (Strahler *et al.*, 1996). In addition wetness and season influence albedo (LaFleuer *et al.*, 1997).

Related measures have been defined which do not depend on atmospheric state. Directional hemispherical reflectance, $\bar{\rho}$, is the integral of the BRDF over the exitance hemisphere with direct beam irradiance from a given solar zenith angle. This quantity is termed “black-sky” albedo and may be defined as:

$$\bar{\rho}(\theta_i; \Lambda) = \frac{2}{\pi} \int_0^{\pi} \int_0^{\pi/2} \rho(\theta_i, \theta_v, \phi; \Lambda) \sin\theta_v \cos\theta_v d\theta_v d\phi \quad (2)$$

where ϕ is the relative azimuth angle between view and illumination directions.

The second measure, bihemispherical reflectance, $\bar{\bar{\rho}}$, weights all irradiance positions equally generating an albedo measure under conditions of perfectly diffuse illumination. This quantity is termed “white-sky” albedo and may be defined as:

$$\bar{\bar{\rho}}(\Lambda) = 2 \int_0^{\pi/2} \bar{\rho}(\theta_i; \Lambda) \sin\theta_i \cos\theta_i d\theta_i \quad (3)$$

2.1.2 Importance of albedo

Knowledge of earth surface albedo is important for climate and climate change studies at a range of spatial scales given the feedback mechanisms between the amount of solar energy absorbed by the surface and the climate system (Li and Garand, 1994; Lewis *et al.*, 1998; Wanner *et al.*, 1997). Land surface albedo is a key parameter in modelling radiative transport in the atmosphere, which in turn is key to understanding climate and vegetation dynamics. The reflective properties of the land surface, as described by albedo, define the lower boundary condition for the flux of radiation through the atmosphere, and characterise the vegetation component of the Earth's biosphere. Anthropogenic land-cover change such as harvesting, deforestation and desertification may also be monitored using surface albedo (Li and Garand, 1994). Consequently, albedo is an important product to be delivered from the data acquired by MODIS.

Surface albedo is one of the key radiative uncertainties in existing global circulation models (GCMs) (Liang *et al.*, 1998). Determination of net surface shortwave fluxes is influenced more severely by the uncertainty in land surface albedo compared to that associated with cloud albedo (Zhang *et al.*, 1995). Climate modelling requires a global albedo product with an absolute accuracy of ± 0.05 according to Henderson-Sellers and Wilson (1983) and ± 0.02 according to Sellers (1993). However, a global albedo data set meeting either of these accuracy requirements has not been available to the climate modelling community (Liang *et al.*, 1998).

2.1.3 Measuring albedo

To date, various methods have been employed to derive global albedo. Ground based measurements may be made at individual locations using upward and downward facing pyranometer / albedometers. This approach has the advantage of providing high quality data at excellent temporal resolution (LaFleur *et al.*, 1997). However, it is limited by the smallness of the area observed by the point measurements (Ohmura and Gilgen, 1993; LaFleur *et al.*, 1997) and the spatial heterogeneity of albedo, which often occurs at a fine spatial scale (Starks *et al.*, 1991; Ohmura and Gilgen, 1993). Spatial heterogeneity of either vegetation or topography limits the utility of point based measurements since, if the surrounding surface characteristics are not homogenous, the observed albedo may not be extended to be representative of a larger area (Starks *et al.*, 1991; Minnis *et al.*, 1997). While an appropriate sampling scheme for a heterogeneous landscape could theoretically be defined, the cost of acquiring sufficient instrumentation becomes prohibitive (Starks *et al.*, 1991). Thus, the traditional approach has been to associate typical albedo values to surface types derived from a global land cover classification (Li and Garand, 1994). This approach may be limited by many factors which include the representativeness of the characteristic land cover classes, classification accuracy and failure to account for latitudinal and seasonal variability and BRDF effects when assigning a *typical* albedo value to a land cover class. At the global scale, satellite remote sensing is the only feasible technique to obtain reliable and accurate estimates of surface albedo including frequent temporal observation (Li and Garand, 1994; Lewis *et al.*, 1998). This approach assumes that with clear skies, the primary influence on top of the atmosphere (TOA) albedo is surface albedo (Li and Garand, 1994).

2.1.4 *Selected previous broadband albedo observations and comparisons*

Studies have been published in the literature for a wide variety of study sites. Several studies have been reported for the polar regions. DeAbreu *et al.* (1994) compare ground based albedo measurements to broadband albedos derived from NOAA 11 and 12 AVHRR Local Area Coverage (LAC) data corrected for atmospheric effects (using 5S) and anisotropy, for arctic sea ice surfaces. Broadband albedo was derived from narrowband AVHRR channel 1(visible) and 2 (NIR) reflectance using a linear regression model. Ground-based measurements were made both at a fixed tower site and along orthogonal transects to assess spatial variability of surface albedo at the scale (1km x 1km) of a AVHRR pixel. Tower site surface albedo was derived using Eppley Precision Spectral Pyranometers in the 285-2800nm range and spatial albedo measurements were made using a Middleton CN-9 Pyranometer in the 300-2600nm range and a Li-COR Terrestrial Pyranometer in the 400-1200nm range.

Albedo variation was correlated with snow fall and ice crystal precipitation. In addition, a large degree of variability was observed along the transects, an observation which the authors use to illustrate the considerations and difficulties in acquiring ground based albedo validation data. Although some variations could be attributed to natural variability, for example due to small linear snow drifts, various sources of error can be identified with the procedure of transect sampling which requires the instruments to be set up multiple times along the transects.

These sources of error include variations in instrument height, orientation to the solar principal plane, shadowing and sensor levelling and most importantly variation given changes in irradiance due to atmospheric variability leading to unstable irradiance conditions during the course of

measuring the transects. Uncertainties are also present with regard to the corrections for atmospheric, viewing geometry and sensor spectral response applied to the AVHRR data. Despite these uncertainties, comparisons of albedo derived from AVHRR with correction for viewing geometry and atmospheric effects to surface tower site albedos are positive.

Haefliger *et al.* (1993) and Stroeve *et al.* (1997) document albedo comparisons over the Greenland ice sheet. Haefliger *et al.* (1993) report broadband albedo values of the ice sheet measured using pyranometers mounted at 1.5m and 27m above the surface of 84.3% and 82.2% respectively. The lower albedo for the higher instrument is attributed to the field camp falling within the field of view and to surface roughness observed at scales of metres and greater. In comparison, broadband albedo derived from a Geophysical Environmental Research (GER) portable field spectrometer which characterises the surface in 875 spectral bands in the range 300-2500nm was 82.9%. The high resolution spectrometer data was further processed using a radiative transfer code, LOWTRAN 7, to account for atmospheric scattering and absorption. Using radiosonde profiling to provide parameters required by the code, AVHRR channel 1 and 2 TOA narrowband albedo values were estimated with an accuracy of 1.3% and 9.1% respectively. In a similar fashion, surface narrow-band albedo estimates were derived from AVHRR TOA albedo. Channel 1 and 2 accuracies were of a similar order or magnitude, 1.7% and 11.7% respectively. The errors are attributed to either inaccurate aerosol modelling or satellite sensor drift due to degradation.

Further research on the Greenland ice sheet is discussed by Stroeve *et al.* (1997). Albedo values were obtained from the AVHRR sensor for the year 1990, 1991 and 1993. Ground based measurements were acquired using a pair of pyranometers to observe upwelling and downwelling

radiative flux, and a Geophysical Environmental Research (GER) portable field spectrometer for spectral albedo and a sun photometer to derive total atmospheric depth. The AVHRR data was atmospherically corrected using 6S (Second Simulation of the Satellite Signal in the Solar Spectrum) (Vermote *et al.*, 1997).

A linear relationship between measured surface broadband albedo and atmospherically corrected AVHRR channel 1 (visible) and 2 (near-infrared) reflectance data was defined using regression analysis for a 35 sample data set containing measurements for snow types ranging from fine-grained new snow to coarse-grained melting snow. The relationship exhibited a root mean square error of 0.66% and $R^2=0.985$. In other words 98.5% of the variation of broadband albedo is explained by the model.

However, this model did not account for the anisotropic nature of snow reflectance. To correct for this deficiency the authors derive a snow BRDF and relate snow surface reflectance to snow surface albedo. Comparisons between broadband albedo derived from AVHRR and surface measurements exhibit good agreement, to within 5%, before snow melt when water ponding on the ice sheet becomes a confounding factor. For example, given point-ground measurements at the camp cover a limited area and do not include melt ponds, the presence of a melt pond in 20% of a AVHRR pixel can lead to a 11% underestimation of broadband albedo. Sensitivity analysis indicates that a change in AVHRR calibration coefficients by 10% has a 6.8% influence on broadband albedo, a 10% change in surface channel albedo weights also has a 6.8% influence and a 10% change in the surface anisotropic reflectance factor has a 5.9% influence.

Lafleur *et al.* (1997) report a study in a subarctic landscape along the western coast of Hudson Bay near Churchill, Manitoba, Canada. Measurements were made along a transect encompassing Hudson Bay and its intertidal zone, open tundra, tundra-forest transition and open forest. The terrain was generally flat with many small lakes and ponds and peaty top soils underlain by permafrost. Six sites were sampled along the transect: open forest, sedge meadow, mixed tundra, beach ridge, shrub forest and lake. Eppley Labs pyranometers operating in the 280-2800nm range were used to measure upwelling and downwelling radiation and derive 30-min average albedos. The remotely sensed data used for comparison was LANDSAT TM imagery. Broadband albedo values were derived using the equations defined by Brest and Goward (1987) having calculated surface reflectance assuming nadir viewing and Lambertian reflectance. The radiative transfer code LOWTRAN was used to derive path radiance, vertical transmission and shortwave irradiance to calculate reflectance.

Ground based measurements acquired in 1991 were compared to concurrent LANDSAT TM imagery for all sites except mixed tundra. Considerable variation in albedo was exhibited along the transect. Average TM albedo from a 3x3 window centred on the ground stations exhibited a 0.01% mean difference to the pyranometer values. Measurements to assess the diurnal variation in albedo for these sites showed that for solar zenith angles less than 60°, albedo is fairly constant varying in the range 0 to 0.04. For solar zenith angle greater than 60°, albedo rapidly increases.

Mid-latitude studies are reported by Barker Schaaf and Strahler (1994), Popp (1995), Minnis *et al.* (1997) and Li and Garand (1994). Broadband albedo derived from directional radiance data acquired by the airborne Advanced Solid State Array Spectroradiometer (ASAS) was compared to temporally continuous pyranometer data by Barker Schaaf and Strahler (1994). Directional

ASAS data for a variable height spruce forest site in Maine was processed using the Li-Strahler geometric-optical BRDF model to derive model spectral hemispherical reflectances. Red and NIR albedos derived from the model were combined using the coefficients derived by Brest and Goward (1987) for LANDSAT data (*see equation 18*). Despite the simplicity of the approach, the authors report the full spectrum albedos to be quite close in magnitude to the pyranometer values. However, only six albedos were derived corresponding to ASAS overpass times. While those between 11am and 2pm (EDT) do indeed exhibit very similar values to the pyranometer derived data, the modelled values fail to mirror the increase in albedo for higher solar zenith angles earlier in the day.

Popp (1995) describes a new atmospheric correction program EXACT (Exact Atmospheric Correction Technique) and demonstrates its utility to derive spectral albedo from satellite measurements. Ground albedometer measurements are compared to data from LANDSAT TM, NOAA AVHRR and Daedalus ATM data acquired during the LOTREX-HIBE 1989 campaign at Hildesheimer Börde, Germany. Albedo values derived using EXACT are shown to be in good agreement with the albedometer measurements for an area of flat terrain. Errors in albedo are less than 0.01 for both visible and NIR TM channels and up to 0.032 in the MIR. For AVHRR, accuracies are better than 0.033 for AVHRR channel 1 and 0.005 for AVHRR channel 2. The ATM data exhibits an error of below 0.031.

Minnis *et al.* (1997) investigated the diurnal variation of surface albedo for the prairies and pastures of a Southern Great Plains site near Lamont, Oklahoma to determine whether dew influences surface albedo sufficiently to affect measurements from space. Surface broadband albedos in the range 300-3000nm were measured using upward and downlooking Eppley PSP

radiometers at half-hourly intervals. Bidirectional reflectance functions and an empirical narrowband-to-broadband relationship were used to derive broadband albedo from GOES radiance data. Although the authors identify flaws in the bidirectional reflectance functions, consideration of both the ground-based and satellite measurements shows clear evidence that broadband albedo values are higher in the morning than in the afternoon under clear conditions. The authors conclude that a 10% influence on broadband albedo may be attributed to dew which forms when winds are light and skies are clear. When conditions are windy or aerosol optical thickness is high, the effects of dew are not clear.

Li and Garand (1994) describe a validation approach developed using co-located satellite radiometer measurements from the Earth Radiation Budget Experiment sensor (ERBE) and tower observations in regions of plain agricultural land at the Boulder Atmospheric Observatory (BAO) at Boulder, Colorado and at a site near Saskatoon, Canada. At nadir the satellite based measurements have a FOV of 35km which is approximately that of the pyranometer mounted on the BAO tower at a height of 300m for the maximum viewing angle of 89° . Despite this coverage, the authors caution that the cosine response of the instrument results in the signal recorded being most sensitive to the reflective properties of the landscape viewed around nadir. Measurements at the Saskatoon tower were for an instrument height of 10m and thus covered a much smaller area. In an attempt to increase the representativeness of these measurements at the satellite spatial scale, observations were made for conditions of uniform snow cover.

The observed surface albedos for the two sites were compared to estimated surface albedos. Both instantaneous and daily mean surface albedos were derived from ERBE data. This was achieved through application of a simple linear relationship between satellite-measured TOA albedo and

surface albedo correcting for spectral and angular effects using a simple parameterisation based on three inputs: TOA albedo, solar zenith angle and total precipitable water. Comparisons of the simultaneous satellite derived and surface albedos agree favourably for both sites which were contrasting in both land cover and atmospheric conditions. Two error measures were reported, a bias error of 0.93% representing the mean difference between the estimated and observed albedo and a random error of 3.07% representing the root-mean-square error of the differences from which bias error is subtracted. The random error of 3.07% is interpreted as of moderate magnitude. The authors attributed it, at least in part, to the different effective field of views of the pyranometers and satellite radiometers and to errors in geolocation such that the tower could occur in any part of a pixel or possibly even in an adjacent pixel.

Low latitude studies are reported by Allen *et al.* (1994) and Lewis *et al.* (1998). Allen *et al.* (1994) describe ground-based measurements of albedo for two contrasting sites near Niamey, Niger for the Sahelian Energy Balance Experiment (SEBEX). Measurements were made over a 15 month period from July 1989 to October 1990. The first site had been left fallow in 1983 and subsequently saw regeneration of natural vegetation producing a landscape of annual herbs and grasses with scattered shrubs of height 2-3m and an occasional tree of height 5-10m. The second site is tiger-bush, a forest-type characterised by dense bands of 2-4m shrubs and 4-8m trees in strips 10-30m wide by 100-300m long surrounded by bare crusted soil. The closed canopy restricts annual herbs and grasses to the edges of the strips.

Allen *et al.* (1994) measured incoming and reflected shortwave radiation using Kipp and Zonen solarimeters. Downward facing instruments were used to measure the albedo of two component surfaces at each site, namely herbs and bushes at the fallow site and soil and bushes at the tiger-

bush site. Diurnal variation in albedo is reported for typical clear and cloudy days in December 1989 (*figure 2.1*). The rank order of albedo is the same for both conditions. Tiger-bush soil exhibits the highest albedo and the bushes the lowest. Fallow herbs and bushes show intermediate values of albedo. The rank order reflects the quantity of plant material which traps radiation due to multiple scattering and absorption. Consequently, tiger-bush soil which is devoid of vegetation has the highest albedo. The tiger-bush bushes, despite being largely leafless, exhibit a low albedo because the woody stems and branches trap solar radiation. Daily mean albedo was derived by calculating the sum of the component albedos weighted by their fractional area coverage. Under cloudy conditions, albedo variation is flattened by the effects of diffuse solar radiation. This contrasts to clear days for which albedo is high at dawn and dusk (high solar zenith angle) and minimal at solar noon (lowest solar zenith angle). For a typical clear day in the dry seasons, March 1990, Allen *et al.* (1994) report albedo increases of up to 0.2 between solar zenith angles of 10 and 80 degrees. Between 10 and 60 degrees solar zenith angle, the maximum observed albedo increase for the components is 0.06.

Lewis *et al.* (1998) invert linear kernel-driven models of surface BRDF against data acquired by ASAS for a range of cover types in Niger as part of the HAPEX-Sahel field campaign. Broadband albedo is calculated from spectral bihemispherical and directional hemispherical reflectance terms derived from inversion. Ground-based point sample measurements made at hourly intervals by Allen and others (Disney, *pers. comm.*) exhibited good agreement with the values derived from ASAS except at extreme solar zenith angles. The deviation between groundbased and ASAS broadband albedos may be attributable to a variety of factors. Firstly, the proportion of diffuse illumination may not be accurately estimated given that the radiative transfer code (6S) used to correct the ASAS imagery is not valid for solar zenith angles greater than 70 degrees. Secondly, it

is important to select appropriate coefficients for the linear weighting of the ASAS spectral albedos to calculate broadband albedo. Errors may be introduced through overestimation of the importance of the contribution of the near-infrared to broadband albedo at high solar zenith angles. In addition, Lewis and Barnsley (1994 in Lewis *et al.* 1998) also note that assumption of isotropic diffuse approximation may introduce errors in calculating albedo for high solar zenith angles.

3. STUDY SITE

Grassland PROVE took place from May 20-30, 1997 at the USDA-ARS/LTER Jornada Experimental Range, a desert grassland in Dona Ana county, 23 miles north of Las Cruces, New Mexico (32.5°N, 106.8°W) (*figure 3.1*). The range consists of an extremely flat valley of approximately 800km² bounded to the east and west by mountains. Land cover may be categorised into three broad types, namely grassland, transitional (mixed grass and shrubs) and shrubland of which, given time constraints, the first two were visited for this study. The shrubs growing on the sandy soils in the vicinity of the tower at the transition site are honey mesquite (*Prosopis glandulosa*) and soaptree yucca (*Yucca elata*) with the dominant grass being black grama (*Bouteloua eriopoda*) (Dick-Peddie, 1993). The categories reflect slow land cover change from grasses to shrubs which is probably occurring following overgrazing at the beginning of the century. The climate is semiarid and as a result vegetation cover throughout the valley is sparse with an average leaf area index (LAI) of 0.5. The occurrence of just a few unpaved roads, data towers, water wells, and fences means that manmade structures will provide a minimal contribution to remote sensing data (Kannenber, 1997; Rahman *et al.*, 1997).

Figure 3.2 presents three overview photographs of the study area. In *Figure 3.2a* the view is north along a local dirt road. Ground cover is characterised by a shrub (mesquite / yucca) and soil mix with some grass. By contrast the ground cover to the south of the tower has a higher coverage of grass with less, but still a significant presence of mesquite and yucca (*figure 3.2b*). *Figure 3.2c* looking to the southwest reveals a fenced section which has similar ground cover to that south of the tower but which is largely devoid of shrubs and which graduates to a sparse grass and soil mix towards the west. To place these photographs further into the spatial context of the landscape,

figure 3.3 presents a Daedalus AADS-1268 Thematic Mapper Simulator (TMS) 7,5,3 (NIR, red, green bands) (LANDSAT TM equivalent bands 4,3,2) false colour composite image with the tower location indicated by the crosshair. The TMS image has not been geometrically corrected and therefore the distortions are unknown, but as a guide to the dimensions the y-dimension of the image is approximately 2km. The three land covers classes, “shrubs and soil” (SS), “grass,” (G), and “grass and soil” (GS) are distinguishable on the image.

4. DATA COLLECTION METHODOLOGY

4.1 *Field measurements*

4.1.1 *Albedo*

Upwelling radiant energy flux from the surface ($E\uparrow(\lambda)$) and downwelling radiant energy flux ($E\downarrow(\lambda)$), over a viewing angle of 2π steradians were measured using Kipp and Zonen CM14 albedometers. The CM14 albedometer consists of two CM11 pyranometers, one oriented to measure direct and diffuse downwelling irradiance (Wm^{-2}) and the other inverted to measure solar radiation reflected from the surface. The CM11 pyranometer specifications meets the requirements of "secondary standard," the most stringent accuracy class specified in ISO 9060 for instruments to measure solar radiation as defined by the World Meteorological Organisation (WMO) (Kipp and Zonen, 1997). The ratio of measured energies, assuming an isotropic radiation field is given by:

$$D = \frac{1}{\pi} \int_0^{2\pi} \int_0^{\frac{\pi}{2}} C(\theta) \cos\theta \sin\theta d\theta d\phi \quad (4)$$

where $C(\theta)$ is the cosine response function (*i.e.* the ratio of the actual response of the instrument to the ideal cosine response) (Grainger *et al.*, 1993).

Assuming an ideal cosine response¹, *i.e.*, the response of the albedometers for an *isotropic radiation field* decreases in proportion to the cosine of the angle of incidence, and azimuthal symmetry, the spatial influence on the albedometer has been determined. Assuming an ideal cosine response ($C(\theta)=1$), integrating *equation 4* with respect to θ provides an expression that describes the response in any given zenith plane, assuming azimuthal symmetry:

$$D = \frac{1}{2\pi} \int_0^{2\pi} [\sin^2 \theta]_0^{\frac{\pi}{2}} d\phi \quad (5)$$

For the sake of completeness, the reader may wish to note that *equation 5* evaluates to:

$$D = \frac{1}{2\pi} \int_0^{2\pi} d\phi = \frac{1}{2\pi} [\phi]_0^{2\pi} = 1 \quad (6)$$

Variation in $\sin^2 \theta$ explains the sensitivity of the albedometer to the signal from points at a given zenith angle. For example, 80% of the signal is derived from points in a field of view extending from nadir to a zenith angle of 63.4° . *Table 4.1* and *figure 4.1* present the spatial response function of the albedometer. The concentric circles are plotted at 10% increments. The observed pattern results from the combined effects of the cosine response of the albedometer and the sine function which originates from spherical geometry considerations. The corresponding distance on the ground has been calculated using simple trigonometry by multiplying the height of the tripod by the tangent of the zenith angle.

¹ For the CM11 pyranometers, the cosine response given as a percentage deviation from ideal at 10 degrees solar elevation on a clear day meets the WMO classification secondary standard of $< \pm 3\%$ (Kipp and Zonen, 1997). Actual mean cosine error for the clear dome at zenith angle $40^\circ = -0.8\%$, at $60^\circ = -0.5\%$, at $70^\circ = -1.5\%$ and measured at $80^\circ = 0\%$.

Broadband albedo was measured for two wavebands. Total shortwave broadband albedo (305-2800nm)² was derived from an albedometer fitted with clear domes and NIR broadband albedo range (695-2800nm) was derived from an albedometer fitted with red domes. Both albedometers were mounted concurrently on a black tripod at a height of 4.1 metres above the surface (*figure 4.2*). A data logger was used to record at least five measurements at each location. Albedo measurements were taken at 10m sampling intervals along 4 short (100m) transects radiating (north, south, east and west) from the tower at the transitional site. Several of these transects were sampled on more than one occasion both under similar and differing solar conditions. Measurements were also made along a longer 1km transect. At the separate grassland site, albedo measurements were made along a 150m transect at 10m intervals for three different solar zenith angles on a single day.

Albedo measurements were also acquired by researchers from the Jet Propulsion Laboratory (JPL) using a total shortwave broadband Kipp and Zonen CM14 albedometer. A semidiurnal time series acquired at a fixed location at the transitional site near the tower has been used to derive a model to correct our albedo measurements for solar zenith angle effects. Having cleaned the JPL albedometer time series to remove obvious outliers resulting from brief episodes of cloud cover, a model of the form:

$$\text{albedo} = \beta_0 + \beta_1 \sin(\beta_3 t) \quad (7)$$

² The specifications of the total shortwave pyranometers for spectral range are 305-2800nm (50% points) and 335-2200nm (95% points). In other words, sensitivity on the shoulders of the spectral range at 305nm and 2800nm is 50%. At 335nm and 2200nm sensitivity is 95% (Kipp and Zonen, 1997).

where β_x are regression coefficients and t is decimalised Greenwich Mean Time, was fitted to the data (*figure 4.3*). Similar trends of albedo as a function of time / solar zenith angle were observed by Barker Schaaf and Strahler (1994) for a spruce forest stand in Howland, Maine and by Allen *et al.* (1994) for fallow and tiger bush sites in the Sahel and by Lafleur *et al.* (1997) for several surfaces in the subarctic near Churchill, Manitoba. The model of the solar angle dependency of albedo has been used to correct all albedo measurements to a common baseline, namely 12 noon MDT (18:00 GMT).

4.1.1.1 Calculation of visible broadband albedo from albedometer measurements

Visible broadband albedometer can be derived from the total shortwave and NIR broadband measurements. Given that the upwelling radiance for the total shortwave can be expressed as:

$$\int_{305}^{2800} E \uparrow (\Lambda) d\Lambda = \alpha_{total} \int_{305}^{2800} E \downarrow (\Lambda) d\Lambda \quad (8)$$

The left hand side of *equation 8* can be broken down into the contributions of the visible and NIR to the total shortwave signal:

$$\begin{aligned} \int_{305}^{2800} E \uparrow (\Lambda) d\Lambda &= \int_{305}^{695} E \uparrow (\Lambda) d\Lambda + \int_{695}^{2800} E \uparrow (\Lambda) d\Lambda \\ &= \alpha_{visible} \int_{305}^{695} E \downarrow (\Lambda) d\Lambda + \alpha_{NIR} \int_{695}^{2800} E \downarrow (\Lambda) d\Lambda \end{aligned} \quad (9)$$

Rearranging *equations 8 and 9*, the formula to calculate the visible broadband albedo from the total shortwave and NIR measurements is:

$$\alpha_{visible} = \frac{\alpha_{total} \int_{305}^{2800} E \downarrow(\Lambda) d\Lambda - \alpha_{NIR} \int_{695}^{2800} E \downarrow(\Lambda) d\Lambda}{\int_{305}^{695} E \downarrow(\Lambda) d\Lambda} \quad (10)$$

Downwelling irradiance in the total shortwave, visible and NIR may be obtained by selecting the corresponding wavelength limits for a given set of atmospheric conditions using 6S.

4.1.2 Hemispherical Photography

Hemispherical photography provides a circular image which is a projection of a hemisphere of directions onto a plane. The nadir point occurs at the centroid of the photography and with a 180° field of view, the horizon appears at the edge. Azimuth angles are true (Rich, 1990).

Hemispherical photographs were acquired using a Minolta X-300 SLR camera. Lens constructs were a Pentavision MC Automatic 1:2.8 f-28mm 520 FOV No. 913139 and a Jessops x0.42 semi-fish-eye adapter with a series III macro adapter ring. The combination of these constructs provides hemispherical photography with a 150° field of view. Focal length was set at infinity. Photography was taken at each of the sites sampled for albedo to characterise the ground cover observed by the albedometers. The camera was mounted on the same tripod at the same height above the ground surface as the albedometers. Given that both the albedometers and camera could not be mounted at the same time, photography was acquired separately from the albedo measurements.

The hemispherical photographs were scanned onto PhotoCD to convert the images to digital format. Standard colour film was used for the photograph and consequently the digital images

consist of red, green and blue channels. The scanned scenes have been processed at a resolution of 1024 lines by 1536 samples.

Figure 4.4 presents the albedo response function overlaid onto a hemispherical photograph. The area between any adjacent pairs of concentric circles accounts for a 10% contribution to the signal of the albedometer. Although the field of view of the photography is only 150 degrees, in excess of 90% of the area contributing to the signal recorded by the albedometer is captured.

4.1.3 Ancillary field measurements

4.1.3.1. GPS measurements

To determine the locations of the transects and tower, measurements were made using a Trimble GeoExplorer II Global Positioning System receiver (Trimble Navigation Limited, 1996a). A second set of GPS measurements were obtained from the Trimble Pathfinder GPS Community Base Station at the Civil, Agricultural, and Geological Engineering (CAGE) facility at New Mexico State University (NMSU) located in Las Cruces, NM (The GPS data is archived at: <http://cagesun.nmsu.edu/gps>). The field data was differentially corrected with the base station data using the Trimble Pathfinder Office software package (Trimble Navigation Limited, 1996b). Differential correction removes the effects of Selective Availability (S/A) which is employed by the Department of Defense and otherwise limits the position accuracy of a single GPS receiver to 100 metres (Trimble Navigation Limited, 1996a). This provided point locations with accuracies to within a few centimetres.

4.1.3.2 *Atmospheric characterisation*

Aerosol optical depth at 550nm was derived from measurements taken from two sources. A team from the University of Arizona, lead by Kurt Thome, collected data on the 23rd May 1997 at the Jornada site using a Reagan Sunphotometer which has ten, 10nm bandwidth spectral channels centred at: 370nm, 400nm, 440nm, 520nm, 610nm (for ozone), 670nm, 780nm, 870nm, 940nm (for water vapour) and 1030nm. Optical depth was obtained from the slope of a Langley plot, a semilogarithmic plot of the instrument output versus air mass (Bruegge *et al.*, 1992). Aerosol optical depth measurements were also acquired from Cimel Sunphotometer instruments operated by JPL and GSFC personnel. Measurements are made in eight, 10nm bandwidth, bands centred at 340nm (for ozone), 378nm (for ozone), 440nm, 499nm, 613nm, 870nm, 940nm (for water vapour) and 1020nm. Optical depth is derived as for the Reagan Sunphotometer (Holben *et al.*, 1998). In order to derive aerosol optical depth at 550nm, which is a required input to the radiative transfer code, 6S, the negative slope of the log-log plot of aerosol optical depth versus wavelength (Ångstrom Coefficient), was used to interpolate between the two closest measured values to 550nm.

4.2 *Remotely sensed data*

4.2.1 *LANDSAT TM (Level 9)*

The LANDSAT Thematic Mapper (TM) is a cross-track scanning instrument with seven spectral bands in the range 450-12500nm with a radiometric resolution of 8 bits. The spatial resolution is 30m, except for the thermal band which is 120m. Bands 1 to 5 and 7 consist of an array of 16

detectors with bands widths of (1) blue-green: 450-520nm, (2) green: 520-600nm, (3) red: 630-690nm, (4) near-IR: 1550-1750nm, (5) mid-IR 1: 1550-1750nm, (7) mid-IR 2: 2080-2350nm.

Band 6, the thermal-IR band, consists of an array of four detectors and has a band width of thermal-IR 10400-12500nm (Markham and Barker, 1985).

Imagery for this study is LANDSAT 5 TM acquired on 25th May 1997 at 17:08 GMT processed to Level 9 by the National LANDSAT Archive Production System (NLAPS) at the EROS Data Center. Level 9 is "precision corrected." This consists of radiometric and geometric correction using the satellite model and platform / ephemeris information. The systematic orbit and attitude models are refined using ground control points to derive a precision spacecraft model producing an image which is rotated and aligned to a Universal Transverse Mercator projection.

4.2.2 AVIRIS

The Airborne Visible/Infrared Imaging Spectrometer (AVIRIS) is a hyperspectral optical sensor with 224 contiguous spectral bands in the range 400nm to 2500nm with a nominal bandwidth of 10nm. The sensor is operated from a NASA ER2 aircraft at an altitude of 20km with an instantaneous field of view (IFOV) of 1mrad providing pixels with 20m spatial resolution (Vane *et al.*, 1993). AVIRIS imagery was acquired for several north-south transects over the Jornada site on May 27th 1997. The data was supplied having been processed to correct for atmospheric effects using 6S (Asner, *pers. comm.*).

4.2.3 *Daedalus AADS-1268 Thematic Mapper Simulator*

The United States Department of Energy (DoE) Citation flew with the Daedalus AADS-1268 Thematic Mapper Simulator (TMS) instrument over Jornada on June 19th 1997 for a project following the Grassland PROVE field campaign co-ordinated by Thomas Schmugge (USDA/ARS Hydrology Laboratory). The sensor consists of a rotating mirror which directs light via a set of mirrors and a dichroic lens to two detectors (Richards, 1993). The sensor provides 7 bands which replicate those of the orbiting LANDSAT TM sensor and four additional wavebands (*table 4*) and is characterised by an IFOV of 2.5 mrad, and a total scan angle of 86°. Data were acquired at two resolutions. 12m resolution imagery was obtained with the aircraft and at an altitude of 4877m and a scan speed of 12.5rps at approximately 17:15 GMT and with 4m resolution with the aircraft at an altitude of 1524m and a scanspeed of 25.0rps at approximately 16:45 (GMT).

4.2.4 *NOAA AVHRR*

The NOAA Advanced Very High Resolution Radiometer (AVHRR) is a five channel scanning radiometer that provides data with a ground resolution of 1.1km at nadir becoming coarser at higher scan angles across the 2400km swath width. The radiometric resolution is 10 bits. The five channels are centred at channel 1: 0.63µm (red), channel 2: 0.86µm (NIR), channel 3: 3.73µm (MIR), channel 4: 10.7 µm (thermal) and channel 5: 11.8 µm (thermal). Measurements from the red and NIR channel are used in this study.

AVHRR imagery of Jornada was acquired from both the polar-orbiting morning descending NOAA-12 satellite and the afternoon ascending NOAA-14 satellite. Pre-processing was performed by Jeff Privette (NASA GSFC). The images were nudged through the use of ground control points to a common CIA map (simple conic projection) consisting of water features defined as vectors so that the rivers and lakes in the images overlaid those in the CIA map. Nearest neighbour resampling was used. The images were visually assessed and quality tags were associated with each image based on visual assessments of images in the infrared band (channel 2) and one of the thermal bands (channel 4). Of 136 daytime AVHRR scenes acquired during May and early June, 20 were assigned a good data quality flag over the Jornada Experimental Range.

During subsequent processing, suspicions arose that the AVHRR pixel thought to contain the tower following registration to the CIA map had been misidentified during pre-processing at GSFC. Various comparisons with the higher resolution imagery and in particular to the accurately geolocated Level 9 TM data confirmed these concerns. As a result, the AVHRR pixel two pixels to the north of the original choice was selected. It is believed that the tower is located towards the southern edge of the new pixel. The two pixel misregistration error in the north-south direction, but not in the east-west direction, may be attributable to the north-south orientation of water features such as the Rio Grande in the CIA map such that the GCPs fixed the east-west location of the AVHRR images more accurately.

The AVHRR sensor does not have a facility to perform on-board calibration of the visible and near-infrared channels. As, for example, Brest and Rossow (1992) report, the calibration coefficients derived during pre-launch testing of sensors cannot be used reliably post-launch.

Post-launch calibration is necessary to compensate for the post-launch degradation due to outgassing, launch associated contamination and the harsh environment in space (Rao and Chen, 1995). Using the south-eastern part of the Libyan desert as a radiometrically stable calibration target, relative annual degradation rates for the visible and near-infrared channels of NOAA-7 are 3.6% and 4.3% respectively, of NOAA-9 are 5.9% and 3.5% respectively, of NOAA-11 are 1.2% and 2.0% respectively (Rao and Chen, 1995) and of NOAA-14 are 7.7% and 10.5% respectively (Rao and Chen, 1996). In the case of the NOAA-14 sensor, spurious effects due to the use of pre-launch calibration coefficients, which are removed using post-launch calibration values, have been noted for NDVI products derived from NOAA-14 (Rao and Chen, 1996).

Unfortunately, at the time of writing, post-launch calibration coefficients were unavailable for NOAA-12. NOAA estimates of NOAA-12 degradation are of the order of 3%, which given the sensor has been operating since 1991, may lead to the introduction of considerable errors into the analysis if this data were used having performed calibration using pre-launch coefficients. In addition, given that the solar zenith angles of the NOAA-12 observations were high enough to be near the upper limit of the reliable range of the BRDF code, the decision was made to only process NOAA-14 observations in this study.

Atmospheric correction of the AVHRR data was performed by Jeff Privette (NASA GSFC) using the 6S radiative transfer code. Aerosol optical depth at 550nm, as required by 6S, was derived from measurements from the CIMELs within five minutes of the satellite overpass, and for times when data were not available, a second-order equation based on the time-of-day was used to interpolate an estimate. Similarly values for water vapour were each derived from measurements at the time of overpass or interpolated. Ozone values were derived from the data collected by Kurt

Thome's (University of Arizona) group and a continental aerosol model was assumed. Surface albedo for atmospheric correction was estimated by Greg Asner (University of Colorado) by convolving average ASD Fieldspec® FR Portable Spectroradiometer reflectance spectra collected to simulate AVHRR values. Other assumptions were homogeneous ground cover and no directional effects. The latter assumption was made having also performed runs to test the use of accounting for BRDF effects within 6S (Privette, *pers. comm.*).

4.2.5 POLDER

The Polarization and Directionality of the Earth's Reflectance (POLDER) instrument aboard the Japanese Advanced Earth Observing System (ADEOS) platform records data for nine spectral bands in the spectral region 400-1050nm at a spatial resolution of 6km x 7km at nadir. The radiometric resolution is 12 bits. The CCD sensor array is of size 242 by 548 photoelements, corresponding to a rectangular field of view of 86 degrees in the along track direction and 102 in the across-track direction. A rotating filter wheel consisting of 16 filters is used to acquire measurements for six non-polarised bands centred at 443nm, 490nm, 565nm, 763nm, 765nm and 910nm, three polarised channels centred at 443nm, 670nm and 865nm each at three polarisation directions, and a dark current measurement. The band width is 20nm except for the bands centred at 765nm, 865nm and 763nm which have bandwidths of 40nm, 40nm and 10nm respectively. The POLDER across-track swath width of 2200km provides near-complete daily coverage of the entire earth except for polar regions. In any pass, a given point of the surface remains in the field of view for about 12 frames. This provides one swath through the BRDF. The target will be observed again approximately a day later, but with an altered ascending longitude which provides

a new set of 12 snapshots. Taken together, observations from successive orbits provide more complete sampling of the BRDF (Deschamps *et al.*, 1994).

POLDER data was supplied by Marc Leroy (CNES) in both Level 1 and Level 2 format. Level 1 products provide measurements that are geocoded and radiometrically corrected to give normalised radiances which are converted to a quantity termed ‘reflectance’ through division by the cosine of the solar zenith angle. Level 2 products provide directional surface reflectances for four bands through atmospheric correction of the Level 1 product. However, the 4 bands of Level 2 data include both nonpolarised and polarised channels, of which the latter are not of use in this study, and it was therefore decided to atmospherically correct the Level 1 data.

Level 1 data including the tower study area were supplied for the 21st through 27th May while Level 2 data was only provided for the 23rd, 25th and 27th after cloud clearing but it was felt this may have been too severe (Leroy, pers. comm.) On the basis of visual inspections of Level 1 imagery from all dates, it was decided to process images from the 22nd, 23rd and 25th May and to exclude imagery from the 27th which exhibited clouds in close proximity to the study area. Non-polarised data for bands centred at 490nm, 565nm, 675nm and 910nm were selected for atmospheric correction.

The atmospheric correction was performed using 6S. A US standard 62 atmospheric model and a continental aerosol model were selected. Aerosol optical thickness was derived from the measurements made by Kurt Thome’s Reagan sunphotometer on the 23rd 45 minutes before the POLDER overpass and from the GSFC Device 59 CIMEL sunphotometer approximately five minutes prior to the overpass on the 25th. Aerosol optical thickness measurements were not

available for May 22nd, so an average of those for the 23rd and 25th was taken. As for the AVHRR correction, a homogenous surface exhibiting no directional effects was assumed while ground reflectance corresponding to the mean spectral value of sand was selected. Comparison of the 6S corrected values for the 765nm band to the atmospherically corrected Level 2 POLDER data indicates excellent agreement which provides confidence that the various assumptions made in using 6S did not produce unreasonable reflectance values.

Table 4.1: Spatial response of the albedometer. See also *figures 4.1* and *4.4*.

Zenith Angle (θ)	Percentage of Total Signal	Distance in Metres from Tripod ($4.14 * \tan \theta$)
18.4	10	1.39
26.5	20	2.06
33.2	30	2.71
39.2	40	3.38
45.0	50	4.14
50.8	60	5.08
56.8	70	6.33
63.4	80	8.27
71.6	90	12.4

Table 4.2: Waveband characteristics of the Daedalus AADS-1268 Thematic Mapper Simulator

Channel	Wavelength range (μm)	Corresponding LANDSAT TM band
1	0.42-0.45	
2	0.45-0.52	TM1
3	0.52-0.60	TM2
4	0.605-0.625	
5	0.63-0.69	TM3
6	0.695-0.75	
7	0.76-0.90	TM4
8	0.91-1.05	
9	1.55-1.75	TM5
10	2.08-2.35	TM7
11	8.5-13.0 (low gain)	TM6
12	8.5-13.0 (high gain)	TM6

5. DATA PROCESSING METHODOLOGY

5.1 *Hemispherical Photography Classification*

Hemispherical photography acquired for all locations on the transitional site and grassland short transects was classified using a semi-automated classification scheme in order to determine the proportion of defined endmember land cover component classes. Qualitatively these may be described as live vegetation, dead woody vegetation, grey vegetation (dormant grass, litter etc.) and soil. Prior to classification, a mask was generated to extract the circular part of the photograph corresponding to the scene and determine its centroid. A second mask layer was then created through manual digitisation to exclude the tripod and the two researchers standing at its base from analysis. Regrettably human presence in the photography was unavoidable due to the short camera trigger cord and the instability of the tripod in the occasionally gusty wind conditions. However, the contribution to the signal from nadir is zero given the $\sin\theta\cos\theta$ dependency of albedo. Also, it was shown experimentally through two independent tests in the field at Jornada and after the campaign at Boston University, that the influence of the presence of the researchers in the photography is minimised by the spatial response function of the albedometers, although this is clearly a source of error.

Image processing was undertaken using the Image Processing Workbench (IPW) (Frew, 1990; Woodcock *et al.*, 1993). A principal components transformation was applied to the masked photography. The first principal component is effectively a brightness image with positive weightings for each band, the second component is a contrast of green band with the red and blue and the third component contrasts the red band with the green and blue. The rearrangement of the information content of the photography using the transformation enhances the ability to

discriminate land cover component endmember states in the scene. Visually, viewing the three principal component images as a false colour composite, with principal components in ascending order on the red, green and blue channels respectively, clearly discriminates live vegetation, which appears light green, from dead woody and dormant grass cover, which appears purple, and soil, which exhibits an orangey hue.

The spectral separation in the image permits live vegetation and soil to be classified using a Bayesian supervised maximum likelihood classifier (Richards, 1993). These areas were added to the mask and a further principal components transformation performed. Training areas were defined for dead vegetation and a Bayesian classifier used to identify pixels of this class throughout the scene. Having masked these newly classified pixels, the same process was repeated to classify grey vegetation including grass and non-green parts of the yucca plants. Considerable time was spent tuning the classification scheme by redefining training areas to maximise classification accuracy. Once defined, the processing stream was run automatically for all sites on the short transects at the transitional site.

Regrettably the scale of analysis precludes the use of a confusion matrix to assess and quantify classification accuracy. Accuracy assessments were based on visual comparison of the classified images to the digitised photographs. When discrepancies were noticed, the training statistics were modified and the classification rerun. Several examples are presented in *figures 5.1a* and *5.1b* for the reader to perform his or her own visual assessment of classification accuracy.

In order to calculate the proportion of each land cover component and its influence on the albedometer measurement it is not possible to simply sum the number of pixels belonging to each class from the classified hemispherical photography.

The fisheye camera lens is characterised by an orthographic projection (*figures 5.2 and 5.3*):

$$r = R_{180} \sin (\theta) \quad (11)$$

where r is the radial distance of a point from the image centre measured in pixels on the photography

R_{180} is the radius of the hemisphere / scene measured in pixels on the photography (Boulianne *et al.*, 1997).

However, given that the field of view of the fisheye lens is only 150 degrees, R_{180} cannot be measured directly on the photography. Consultation of *figure 5.4* indicates that R_{150} may be calculated very simply from

$$R_{180} = \frac{R_{150}}{\sin (75)} \quad (12)$$

Thus *equation 11* may be rewritten:

$$r = \frac{R_{150} \sin (\theta)}{\sin (75)} \quad (13)$$

Equation 13 enables the zenith angle of any pixel in the image to be calculated. Nadir is taken as the point directly beneath the albedometer dome. With reference to *figures 5.3*, θ is calculated from:

$$\theta = \sin^{-1}\left(\frac{r \sin(75)}{R_{150}}\right) = \sin^{-1}\left(\frac{\sqrt{(x - x_0)^2 + (y - y_0)^2} \sin(75)}{R_{150}}\right) \quad (14)$$

For each pixel, $\cos(\theta)$ is calculated and a weights image constructed which attributes a weighting to each pixel consistent with the cosine response of the pyranometer.

The weights image and classified map are overlaid and weighted class proportions calculated. Rather than each classified pixel having a equal contribution, i.e. weight of one, in the summing process, the running total for each land cover component is incremented by the cosine of the zenith angle for each pixel. The final totals are converted to proportions (p), but for a binomial distribution, the variance is a function of the mean. To compensate, a $\sin^{-1}(\sqrt{p})$ transformation has been applied which stretches the tails of the distribution and compresses the middle (Sokal, 1973).

The weighted land cover component proportions are associated with the corresponding albedo measurements for each sample site. The regression procedure in the statistical software package, SAS, (SAS Institute Inc., 1989) has been used to fit a model of the following form to the data taking either total shortwave or NIR broadband albedo measurements as the dependent variable and the transformed weighted land cover component proportions as the independent variables:

$$\text{albedo} = \beta_1 p_{\text{soil}} + \beta_2 p_{\text{dead woody vegetation}} + \beta_3 p_{\text{grey vegetation}} + \beta_4 p_{\text{live vegetation}} + \text{error} \quad (15)$$

where p_x is the weighted proportion of the land cover component. Coefficient values (β s) are derived using least-squares estimation. The intercept term is omitted from the model because, if the classified components represent the true endmember classes in the scene, the model to derive albedo should be a mixture model of these. Although, due to the inherent multicollinearity, a more statistically significant model may be fitted using a subset of the endmembers, from a theoretical perspective, all elements in the scene control albedo and should be retained in the model. As described earlier, data acquired from a fixed location Kipp and Zonen CM14 albedometer, operated at Jornada by MISR personnel, have been used to derive correction factors to amalgamate data acquired for all transects compensating for solar zenith angle effects. This enables a single regression model to be derived for the study site.

5.2 *BRDF Model Description*

The foundation of the MODIS BRDF / albedo product is a semiempirical, kernelbased modelling approach (Roujean et al, 1992) developed by Wolfgang Lucht called AMBRALS (Algorithm for MODIS bidirectional reflectance anisotropy of the land surface). The mathematical form of this type of model is given by (Roujean et al, 1992):

$$R(\theta_i, \theta_v, \phi, \Lambda) = f_{\text{iso}}(\Lambda) + f_{\text{geo}}(\Lambda) \cdot k_{\text{geo}}(\theta_i, \theta_v, \phi) + f_{\text{vol}}(\Lambda) \cdot k_{\text{vol}}(\theta_i, \theta_v, \phi) \quad (16)$$

where R is reflectance, k_{geo} and k_{vol} are kernel functions and f are the weights of the model parameters. The kernels are a function of viewing and illumination geometry. They describe basic

BRDF shapes into which the full BRDF may be decomposed. Thus, the BRDF is modelled as a linear superposition of kernel shapes which have been defined to represent different types of scattering (Wanner *et al.*, 1997).

BRDF model inversion for this study has been performed on the reflectance distributions using AMBRALS. Model inversions in this study have been forced to use the RossThick and LiSparse kernels because these kernels allow the most diverse range of possible BRDF shapes. Privette *et al.* (1997b) performed inversions of 10 models on BOREAS PARABOLA data. By ranking each of the models by the accuracy of estimated quantities of nadir reflectance and spectral albedo, it was found that the RossThick-LiSparse model together with a non-linear model developed by Rahman *et al.* (1993) were the most accurate of those tested.

5.3 *Derivation of broadband albedo from narrowband measurements*

5.3.1 *Theoretical basis*

The theoretical basis of narrowband to broadband albedo conversion is division of a spectral albedo curve into sections of uniform reflectance for which a narrowband measurement may be associated. Broadband albedo may be derived by weighting the narrowband albedo values by the proportion of total solar irradiance encompassed by the wavelength range of each section (Kriebel, 1978; Brest and Goward, 1987; Strahler *et al.*, 1996). The derivation of broadband albedo (α) may be represented mathematically as a discretisation of the full integral by (Kriebel, 1978):

$$\alpha = \frac{\sum_{\Delta\lambda} \alpha(\lambda) E \downarrow(\lambda) \Delta\lambda}{\sum_{\Delta\lambda} E \downarrow(\lambda) \Delta\lambda} \quad (17)$$

It is important to recognise that solar irradiance varies as a function of solar zenith, atmospheric state and surface reflectance and consequently a single broadband albedo is not characteristic of a surface type.

Brest and Goward (1987) apply this method to nadir LANDSAT measurements. Their work provides a clear demonstration of the procedure. Note, Lambertian reflectance is assumed in their work so nadir spectral reflectance is taken as equivalent to narrowband albedo. *Figure 5.5* presents simplified spectral reflectance curves for both vegetated and non-vegetated surfaces. The vegetation curve is divided into visible, NIR and MIR spectral intervals for which the associated proportion of solar irradiance based on solar irradiation spectral distribution for a typical spring day defined by Boer (1977) have been calculated. These weighting factors are used to calculate surface albedo using a three-part weighted average of surface reflectance characterised by a LANDSAT band ($\rho_{\text{band } x}$) of the form:

$$\alpha = 0.526\rho_{\text{band4}} + 0.362\rho_{\text{band7}} + 0.112(0.5)\rho_{\text{band7}} \quad (18)$$

No LANDSAT MSS band coincides with the MIR, however ignoring this spectral interval would lead to erroneously high albedo. Therefore, it was estimated that reflectance in this region is half that in the NIR characterised by band 7.

The more uniform spectral reflectance of the non-vegetated surface permits division into two spectral intervals, visible and a combined NIR and MIR. A two part weighted average may be used to calculate albedo without the weighting factor of 0.5 for the MIR as in *equation 18*:

$$\alpha = 0.526\rho_{band4} + 0.474\rho_{band7} \quad (19)$$

Similarly, Irons *et al.* (1988) derive total shortwave broadband albedo for big bluestem grass. In this study Lambertian reflectance is not assumed and spectral measurements at multiple view directions are made using a truck-mounted Barnes Model 12-1000 Modular Multiband Radiometer (MMR) for seven bands between 450nm and 2350nm. The shortwave spectrum (300-3000nm) is divided into ten spectral regions. For seven of these regions, spectral bidirectional reflectance factors are calculated as an average of MMR derived reflectance factors weighted by the associated downwelling solar irradiance. Three regions not characterised by MMR data are assumed to have negligible influence due to their associated low total downwelling irradiance. Total shortwave broadband albedo is then calculated through numerical integration of the bidirectional reflectance factors over the viewing hemisphere.

This method has also been shown to provide broadband albedo estimates for bare soil as well as grass discrete waveband, bidirectional, ground-based radiometer measurements using both numerical integration and integration of an empirical model fit that are comparable to pyranometer derived values (Ranson *et al.*, 1991). However, Starks *et al.* (1991) report that albedo estimates from bidirectional reflectance data using this method exhibit a systematic overestimation trend when compared to pyranometer measurements. It is suggested of the various potential sources of error that much of the bias may be attributable to only acquiring data in the

solar principal plane. The influence of inappropriate weighting coefficients could not be quantified. More promising results were reported by Wanner *et al.* (1997) who describe the method that will be used to derive albedo from MODIS data. Albedos in the seven bands were splined with tie points to get broadband albedo. Potential accuracies using the seven MODIS land bands for three different cover types to derive total, visible and infra-red broadband albedo are within 1 or 2%.

5.3.2 Implementation

In this study, broadband albedos were derived for both AVHRR and POLDER using the weighted average method. Imagery acquired by the NOAA-14 AVHRR sensor from several orbits provided a data set with eight observations with varying view and illumination geometry which provided the basis to characterise the surface BRDF. Similarly, during each overpass of the study site, POLDER acquires images which sample a swath through the viewing hemisphere. In order to adequately characterise the surface BRDF and obtain reliable results from the inversion process, POLDER observations from three passes with clear sky conditions over Jornada obtained over the duration of the field campaign have been amalgamated into a single data set.

Spectral directional hemispherical reflectance (black sky albedo) and bihemispherical reflectance (white sky albedo) have been derived for each waveband (red and NIR channels for AVHRR, blue, green and two NIR channels for POLDER) for a given solar zenith angle through model inversion using AMBRALS to derive the model parameters. AMBRALS was then run in forward mode to obtain black sky albedo for a solar zenith angle of 18.3° , that of solar noon on May 26th

1997 and the baseline time for the albedometer measurements. Spectral albedo may be approximated using a weighted sum of these parameters:

$$\alpha(\Lambda) = (1 - d(\Lambda, \theta_i))\bar{\rho}(\Lambda, \theta_i) + d(\Lambda, \theta_i)\bar{\bar{\rho}}(\Lambda) \quad (20)$$

where $d(\Lambda, \theta_i)$ is the proportion of diffuse illumination (Lewis, 1995; Lewis *et al.*, 1998). This approximation assumes the sensitivity of surface albedo to the directional distribution of sky irradiance is negligible, which Lewis and Barnsley (1994 in Lewis *et al.* 1998) report is reasonable except for large solar zenith angles. The proportion of direct and diffuse irradiance for each waveband has been obtained using the 6S (Second Simulation of the Satellite Signal in the Solar Spectrum) atmospheric radiative transfer code (Vermote *et al.*, 1997). Spectral albedos were calculated for two values of aerosol optical depth at 550nm derived from the May 26th Cimel Sunphotometer Device 59 data (see §4.1.3.2). An aerosol optical depth measurement acquired at 11:50 is the closest to local noon, the baseline time taken for the albedo measurements. However, given that that aerosol optical thickness on the 26th during the day was typical of the higher values encountered during the field campaign, calculations were also made for a typical minimum value of aerosol optical depth. In this way, an assessment of the sensitivity of broadband albedo derivation to aerosol optical thickness was undertaken. An US Standard 62 atmosphere and a continental aerosol model were used and for atmospheric correction only it was assumed that the surface was a Lambertian reflector.

The spectral albedo values were used to generate an albedo profile over the shortwave spectrum by a different methods for each of the sensors. For AVHRR, the availability of only red and NIR spectral albedo values precluded the derivation of an albedo profile by splining. Taking a similar

approach to that of Brest and Goward (1987), a value for broadband albedo could be derived by deriving two ratios, that of solar irradiance integrated over all wavelengths in the visible portion of the electromagnetic spectrum to solar irradiance integrated over all wavelengths and that of solar irradiance integrated over all wavelengths in the NIR and MIR portion of the electromagnetic spectrum to solar irradiance integrated over all wavelengths. For this study the visible portion of the spectrum is 305nm and 695nm and the NIR / MIR portion from 695nm to 2800nm. These ratios could be used to weight the red and NIR spectral albedos respectively.

An approach of this type has been used by several authors. Saunders (1990) assumed weights of 0.5 for both the visible and NIR channels to derive a broadband albedo with an undisclosed wavelength range from AVHRR narrowband bidirectional surface reflectance values. He *et al.* (1987) cited in Di and Rundquist (1994) and Laine and Heikinheimo (1996) use weights of 0.322 and 0.678 for the visible and NIR AVHRR reflectances respectively to estimate broadband albedo in the range 580nm to 1100nm. While the more limited wavelength range used in the definition of broadband albedo in the latter studies may increase the applicability of the technique, this approach is highly unsatisfactory from a theoretical point of view given that it assumes the reflectance curve can be characterised by two flat profiles in the visible and NIR/MIR.

Instead, a 224 band hyperspectral AVIRIS reflectance profile (atmospherically corrected using 6S by Greg Asner (University of Colorado)) was extracted from the vicinity of the tower site and adjusted to fit the AVHRR spectral albedos. The profile was smoothed using a median filter and then remaining erroneous values in regions affected by water absorption were manually removed. A continuous profile in the range 305nm to 2800nm was generated by fitting a spline taking a

1nm increment using IDL (Research Systems, Inc., 1995) with tie points defined at the minimum and maximum wavelengths.

In using the AVIRIS reflectance curve, it is assumed that the characteristics of spectral albedo are the same as those of reflectance. This approximation should be closer to the unknown truth than the approaches described above which attempt to characterise the upwelling spectrum using a single observation in each of the visible and NIR portions of the electromagnetic spectrum. The tower site at Jornada is located near the edge of an AVIRIS flightline and would therefore have been viewed at an angle of approximately 14° . Due to the $\cos(\theta)\sin(\theta)$ dependency of albedo (*see equation 1*) reflectance at 45° has the greatest influence on albedo. At a view angle of $\sim 14^\circ$ a greater percentage of soil and a smaller percentage of vegetation would be seen compared to an observation at 45° . It would therefore be expected that the reflectance profile observed at $\sim 14^\circ$ by AVIRIS would overestimate spectral albedo given that soil reflectance is greater than that of vegetation in both the visible and NIR portions of the electromagnetic spectrum (*figure 5.6*).

In order to use the AVIRIS reflectance curve as a guide to extrapolation and interpolating the two narrowband AVHRR albedo values to the respective broadband range, AVIRIS reflectances at the midpoint of the red AVHRR channel (630nm) and of the NIR channel (912.5nm) were compared to the AVHRR red and NIR spectral albedos. A pair of simultaneous equations were defined to derive a constraining function to stretch and translate the AVIRIS spectral albedo curve to fit both AVHRR spectral albedo values:

$$\begin{aligned} \text{AVIRIS}_{\rho(\text{red})} &= m * \text{AVHRR}_{a(\text{red})} + c \\ \text{AVIRIS}_{\rho(\text{NIR})} &= m * \text{AVHRR}_{a(\text{NIR})} + c \end{aligned} \tag{21}$$

Solving for m and c , the translation factor is given by:

$$\begin{aligned} \text{AVIRIS}_{\rho(\Lambda)} = & \left(\frac{\text{AVHRR}_{a(\text{NIR})} - \text{AVHRR}_{a(\text{red})}}{\text{AVIRIS}_{\rho(\text{NIR})} - \text{AVIRIS}_{\rho(\text{red})}} \right) \text{AVHRR}_{a(\Lambda)} \\ & + \text{AVHRR}_{a(\text{red})} - \left(\frac{\text{AVHRR}_{a(\text{NIR})} - \text{AVHRR}_{a(\text{red})}}{\text{AVIRIS}_{\rho(\text{NIR})} - \text{AVIRIS}_{\rho(\text{red})}} \right) \text{AVIRIS}_{\rho(\text{red})} \end{aligned} \quad (22)$$

The AVIRIS reflectance curve was adjusted using this function to derive the albedo profile to be weighted by the downwelling irradiance.

For POLDER, the albedo profile was generated by fitting a spline using IDL based on POLDER spectral albedos at 490nm, 565nm, 765nm and 910nm. Two tie points at either end of the spectral region were defined to constrain the spline to sensible values at the limits after consulting other spectra used in data analysis collected using various instruments at Jornada. Values of albedo were calculated along the spline at 1nm intervals.

The solar irradiance curve was integrated and converted to the proportion of total solar irradiance for a given solar angle $W(\lambda, \theta_i)$ for 1nm spectral intervals in the range 305-2800nm.

Theoretically, broadband albedo may then be calculated by integrating over the desired portion of solar spectrum:

$$\begin{aligned}
\alpha &= \int_{solar} W(\Lambda, \theta_i) [\bar{\rho}(\Lambda, \theta_i)(1 - d(\Lambda, \theta_i)) + d(\Lambda, \theta_i) \bar{\bar{\rho}}(\Lambda)] d\Lambda \\
\alpha &= \int_{solar} W(\Lambda, \theta_i) \alpha(\Lambda) d\Lambda
\end{aligned} \tag{23}$$

This integral is estimated by a weighted summation over a finite number of wavebands as presented in the discretised form by Kriebel (1978) (*see equation 17 above*). In this study the summation is performed using values for 1nm waveband intervals calculated as described. The integration has been performed for the total, visible and NIR portions of the solar spectrum to provide broadband albedos for each of these cases for both AVHRR and POLDER. The solar irradiance spectrum used in this study is from Analytical Spectral Devices, Inc (1996) for clear sky and good visibility conditions approximately one hour before local noon on April 23rd 1996 at the Cloud and Radiation Testbed central facility in the Southern Great Plains. Unfortunately, no concurrent co-located downwelling spectral irradiance distribution was measured at Jornada.

6. RESULTS AND DISCUSSION

6.1 *Assessing the spatial variability using ground measurements*

6.1.1 *Qualitative evaluation*

Figure 6.1 plots total shortwave and NIR broadband albedo for the north transect acquired on three days at approximately the same time and corrected to noon values using the solar zenith angle correction model. Small but consistent variations in albedo may be observed. Lower albedos e.g. site 6, are associated with higher proportions of vegetation cover (*see also figure 5.1(a)*) and higher albedos, e.g. site 9, are associated with sites dominated by bare soil (*see also figure 5.1(b)*). Despite the small range in albedo, similar trends along the transect for all three days provide confidence that the key controlling factor is the proportion of different land cover components rather than random fluctuations. Similar qualitative evaluations apply to the south, east, west and grassland transects.

The measurements acquired at the grassland site illustrate the importance of applying a solar zenith angle correction to albedo. *Figure 6.2(a)* shows total shortwave and NIR albedo measurements acquired for the 16 sites on the grassland transect at three different times on May 27th. For both the total shortwave and NIR, albedo values are higher for the measurements acquired between 09:00 and 10:00 compared to those recorded between 10:30 and 11:15 which are in turn higher than those taken between 12:30 and 13:00. The range of values for a given location is up to 0.015 which is approximately the variation along the transect, excluding location 15.

Figure 6.2(b) shows the total shortwave and NIR broadband measurements for the grassland transect having corrected for solar zenith angle effects. The correction clearly removes a significant amount of variability due to solar zenith angle effects, but the curves do not exhibit perfect agreement for various reasons.

Firstly, the model was derived from JPL measurements for a site exhibiting a typical mixture of soil, grass and vegetation at the transitional site, whereas the proportion of dormant grass was considerably higher for most sites at the grassland site. It has also been assumed that the model derived using the total shortwave broadband measurements can be applied to the NIR broadband albedo measurements in the absence of similar semi-diurnal measurements with a red-dome instrument.

Secondly, as also identified by DeAbreu *et al.* (1994) remaining sources of error include differing atmospheric conditions, along with variations in instrument height, orientation to the solar principal plane, albedometer levelling as well as inexact repositioning of the tripod for repeat measurements and differences in shadowing. In addition, when conditions were gusty, it was necessary for a researcher to stand at the base of the tripod to provide stability. However, consideration of the spatial response function of the albedometer overlaid on a hemispherical photograph (*figure 4.4*) suggests that only small percentage of the signal was influenced by the human presence. Despite these remaining sources of error, *figures 6.2(a)* and *6.2(b)* clearly illustrate the importance of either collecting measurements at a similar time of day, or if this is not possible, that a solar zenith angle dependence model should be applied to the data to correct to a common baseline and the data required for defining that model need to be acquired in the field.

However, solar zenith angle effects do not explain the significantly lower magnitude of both the total shortwave and NIR broadband albedo values for the north transect acquired on May 23rd compared to those acquired on the 22nd and 26th (*figure 6.1*). The lower magnitudes of albedo for the north transect on the 23rd may be attributed to the influence of rainfall the previous afternoon. Precipitation data indicate that a total of 1.6mm of precipitation fell in early-mid afternoon on May 22nd (Privette, *pers. comm.*). Despite the rapid drying expected given the effects of wind, solar radiation and normal vapour pressure deficit in the desert environment, *figure 6.1* clearly indicates that the previous day's rainfall influenced soil brightness in late morning. Albedo measurements of the south and east transects which were also acquired on the 23rd are similarly reduced in magnitude. The west transect, measured on the 26th is not influenced by precipitation effects.

6.1.1.1 Correction for soil moisture effects

To successfully amalgamate measurements from all four transects for quantitative modelling necessitated correcting the observed values from the south and east transects for both solar zenith angle effects and soil moisture effects. Fortunately, albedo measurements were made for a site on the south transect on the 26th May at a similar time to the measurements of the south and east transects on the 23rd. A scaling factor was defined as the difference between the measurements for the two days and applied to all sampling points on the south and east transects. Although the effect of soil moisture could be evaluated for all sites on the north transect, these measurements were taken later in the morning. Using a correction factor based on the mean of these differences may have underestimated the necessary correction given the similar time of measurement and the expected rapid drying effects in the desert. Indeed, comparison of the mean difference for both

the total shortwave and NIR albedos indicate that the correction factor based on the single site on the southern transect was greater in both the shortwave (3.05 compared to 1.79) and NIR (3.81 compared to 2.63). Despite the inherent errors due to estimating a correction factor for all points on the south and east transect from the single site, it was felt that this correction factor was more appropriate to apply than the average of difference of the measurements from the north transect given that the south and east transects were typically characterised by a higher occurrence of grey grass than found on the north transect.

6.1.2 *Quantitative evaluation*

The resultant data set, with corrections for soil moisture and solar zenith angle effects, was used to derive a linear mixture model between broadband albedo and the weighted land cover component proportions of the form given in *equation 15*. The grassland transect was not included in the quantitative modelling due, to apparently inadvertent use of different camera settings which prevented these images being classified into the same land cover component classes used for the photographs acquired at the transitional site. Two other data sets, the first with neither solar zenith angle nor soil moisture corrections and the second with solar zenith angle, but not soil moisture corrections were also processed to illustrate the influence of the corrections for modelling broadband albedo.

Attempts to apply the linear mixture model to the uncorrected and solar zenith angle corrected data produced poor model fits. The graphs of observed versus predicted total shortwave and NIR albedo (*figures 6.3(ab)* and *6.4(ab)*) show a clear bias such that the model consistently overpredicts sites characterised by lower albedo values and underpredicts sites characterised by a

higher albedo. Although *figures 6.2(ab)* illustrated the need to perform a correction for solar zenith angle effects for measurements made at the grassland site, clearly an additional factor introduced a much greater bias into the albedo measurements.

Consultation of the model coefficients (*tables 6.1 and 6.2*) used to derive the plots in *figures 6.3(ab)* and *6.4(ab)* indicates that only those associated with soil and live vegetation are significant at the 95% significance level. Although from a statistical viewpoint the coefficient for grey vegetation is not significantly different from zero, from a theoretical perspective, albedo is influenced by all the proportions of endmembers in the scene and therefore this variable should be retained in the linear mixture model. Therefore, its negative magnitude is worrisome given that the model would predict a negative albedo for a site dominated by grey vegetation.

The use of the data set with corrections for both solar zenith angle and soil moisture effects provided much more satisfactory results. Highly significant (Overall F-test: $p < 0.001$) models were formed for both total shortwave and NIR broadband albedo. Model coefficients are given in *table 6.3*. These indicate that the most important controlling factor is soil. Grey (dormant) and live vegetation cover are also important determinants of albedo, but less influential than soil. The amount of woody vegetation has a small influence.

All parameters have positive coefficients and all are significant in the total shortwave and NIR models except the proportions of woody vegetation. This variable only has a small presence at most sample sites. In addition, with a sample size of 44 and for a model with four explanatory variables, there may be poor statistical power. As mentioned above, given that from a theoretical perspective, albedo is influenced by all the proportions of endmembers in the scene, this variable

has been retained in the linear mixture model. Although the coefficient may not be significantly different from zero, it is still the best estimator of the true underlying estimate that would emerge with more extensive sampling. *Figures 6.3(c)* and *6.4(c)* show observed versus predicted total shortwave and NIR broadband albedo respectively. The R^2 is 0.70 for the total shortwave and 0.69 for the NIR model. The linear mixture model of soil, grey (dormant) vegetation, woody vegetation and live vegetation explains 70% and 69% of the variation in total shortwave and NIR broadband albedos respectively. The RMSEs suggests that the total shortwave albedo may be predicted to ± 0.014 and NIR albedo to ± 0.025 .

An independent test of the predictive ability of the linear mixture models was performed using measurements acquired for sites located at the end of a 1km transect to the east of the tower. These seven sites exhibit various proportions of the endmember classes varying from soil dominated to sites with a significant amount of vegetation. The weighted land cover component proportions derived from the classified images were used as inputs to linear mixture models to derive the total shortwave and NIR broadband albedo with coefficient values as given in *table 6.3*. Observed and predicted values of albedo are given in *table 6.4* and plotted in *figure 6.5*.

For the total shortwave broadband albedos, the predicted albedos are within 0.02 of the observed. For the two sites with the highest proportion of soil, the predictions are less accurate and underpredicted. However, the observed albedos for both these sites fall outside the range used to formulate the model. In addition, in *figure 6.3(c)* it was observed that sites with higher albedos were underpredicted. Extrapolating this trend to slightly higher values suggests that an underprediction bias would be expected.

The NIR broadband albedos are predicted less accurately, although this observation is not unexpected given the higher RMSE associated with this linear mixture model and the greater scatter around the $y=x$ line in *figure 6.4(c)*. *Figure 6.5* shows that while the model has predicted albedo with errors of up to 0.0138, the relative magnitude of albedos for all seven locations is correct. This suggests that the NIR broadband albedo model may be used to identify the relative change in albedo as a function of the proportions of land cover components but not necessarily the absolute magnitude. In other words, the model could be used to determine whether a particular location had a greater proportion of a given cover type, although the absolute magnitude would be uncertain.

Although not a conclusive validation, these observations provide confidence that the model could be applied to derive estimates of total shortwave albedo for locations for which the proportions of the component classes are known. These, for example, could be extracted by performing spectral unmixing on hyperspectral data such as that provided by AVIRIS. The main limitation is likely to be that the predicted total shortwave albedo of sites which contain a high proportion of soil are likely to be underestimated. Thus, an important recommendation for future field work is measurement of pure endmember sites.

Further discussion and analysis of the model formulation process and data sets provides additional insights, potential explanations and cautions. Given that the albedo measurements have partially overlapping fields of view, it was possible that spatial autocorrelation may have been present in the data. Moran's I for the total shortwave residuals ($I=0.096355$, $z=0.756$, $p=0.225$) indicates that the analysis is not complicated by spatial autocorrelation. However, the NIR residuals do exhibit spatial autocorrelation ($I=0.39949$, $z=2.674$, $p=0.004$). This factor is a

possible explanation of the apparently poorer predictive ability of the NIR albedo given that confidence intervals for prediction will be invalid in the presence of spatial autocorrelation. Its occurrence for the NIR, but not for the total shortwave albedo may be due to increased influence of multiple scattering by vegetation in the former.

Consideration of the relative magnitude of regression coefficients for both models indicates that while the proportion of soil is clearly the dominant controlling factor, the relative influence of the live vegetation coefficient is greater for the NIR model. For the shortwave albedo, the signal is driven by soil with visible wavelengths as the dominant influence. In the NIR, where live vegetation has a higher reflectance than in the visible, I suggest bushes in overlap areas between transect sites may have a proportionally greater influence and thus spatial autocorrelation is observed. The bushes are variable in space at a similar scale to the separation of the sampling sites while that of soil is at a finer or coarser scales.

Other factors also limit the explanatory power of the linear mixture models. Various sources of error were discussed in the qualitative modelling results section (§6.1.1). For both models, high albedo, soil dominated sites exhibit an underprediction bias. Further errors specific to the quantitative modelling may have introduced inaccuracies. Firstly, errors will have been introduced through modelling of solar zenith angle using a diurnal cycle from a single site characterised by higher proportions of the other endmember classes. In addition, given that JPL were only operating a total shortwave broadband albedometer, it was necessary to assume that the trend in NIR albedo was identical. Bias may also have been introduced due to definition of the translation factor to compensate for soil moisture defined using a single site on the southern transect which was subsequently applied to all sites on the south and east transects.

Thirdly, the portions of the photographs occupied by the researchers and tripod were set to unclassified as the ground cover in these locations was obscured. Although intuitively, one might believe the assumption that the obscured areas would be predominantly soil, visual assessment of the photographs suggested that such an assumption could not necessarily be upheld. Consequently, the mask areas were set to unclassified. In addition, approximately ten percent of the land area viewed by the albedometers was not captured in the hemispherical photography given that the 150° FOV of the fisheye lens in comparison with the 180° FOV of the albedometer. Finally, the tripod may not have been set up exactly at the same location or at the same height for both albedo measurements and photography and hence the view captured by the photographs may not have exactly coincided with that seen by the albedometers. Clearly all these factors will have introduced a bias into the proportions of land cover components input to the linear mixture model.

Furthermore, the endmember class proportions are biased to an unquantified degree by the necessity of human presence in the photography. Regrettably the shortness of the camera trigger cord necessitated standing at the base of the tripod to take the photographs leading to unclassified pixels in the land cover component images. In addition, a further potential endmember land cover class and a known important element controlling reflectance measurements, shadow, could not be quantified since hemispherical photography was acquired at different times from albedo measurements.

6.2 *Deriving albedo at satellite spatial scales*

6.2.1 *AVHRR 1.1km broadband albedo through narrowband to broadband albedo conversion*

6.2.1.1 *AVHRR 1.1km broadband albedo values and comparison to mean of transect measurements*

Total shortwave, visible and NIR broadband albedos were derived for the AVHRR pixel containing the tower at the transition site and several surrounding pixels using the narrowband to broadband albedo conversion scheme outlined above (§5.3). *Tables 6.5 and 6.6* present AVHRR broadband albedos derived using low and high estimates of aerosol optical thickness associated with the transect measurements for the tower pixel, pixels immediately below, right and below right of the tower pixel and for the mean of the 44 short north, south, east and west transect sites. Derivation of the AVHRR broadband albedos requires atmospheric parameterisation to derive the proportions of direct and diffuse irradiance, for which aerosol optical thickness is the key variable being derived from ancillary ground measurements.

A comparison of *tables 6.5 and 6.6* indicates that the choice of aerosol optical thickness has a small influence on the derived broadband albedo with differences occurring in the third decimal place. Thus, for broadband albedos derived using either a low or high AOT estimate, comparison of the mean broadband albedos of the transect sites to that derived for the AVHRR tower pixel show excellent correspondence. The mean broadband albedos of the four AVHRR pixels also compare favourably to the mean of transect measurements deviating at most by 0.080. However,

given that the tower is located towards the bottom of the AVHRR pixel it may be more appropriate to compare the mean of a 2.2km x 2.2km cell which has the tower approximately at the centre, in particular to allow for co-location error. Taking this approach, the total shortwave and visible broadband albedo values derived from AVHRR compare slightly less favourably, but are still in excellent agreement with all comparisons within 0.01 of the mean albedo from the transect measurements. Looking at the other three pixels in the 2.2km x 2.2km area, none of the broadband albedo values derived for these deviate from the ground measurements by more than 0.02.

These results suggest that albedo validation at the satellite spatial scale may be possible through characterisation of the validation site based on sufficient ground based sampling to derive the mean albedo that is detected at the 1.1km scale from space. The results also suggest that derivation of broadband albedo does not require a rigorous atmospheric characterisation, although to minimise error it would clearly be desirable for ground based sampling to take place at the same time as the satellite overpass and under stable clear sky conditions such that not only is the aerosol optical thickness known, but it is more or less constant for all surface measurements.

The mean albedos from the transect measurements compare extremely favourably with the values derived from the narrowband to broadband conversion of the AVHRR data. However, it would be imprudent not to further investigate other factors to examine whether the mean of the transect broadband albedo measurements provides appropriate validation values or whether the excellent association observed is somewhat by chance.

6.2.1.2 Spatial modelling of albedo at coarse resolution from ground measurements through land cover classification and comparison to AVHRR derived values

In choosing a location to validate measurements at the satellite spatial scale, it is vital to select a site that is either homogenous, such that a single measurement from a tower can accurately characterise the albedo over the entire footprint, or to derive a strategy to capture and account for spatial variations in albedo within a heterogeneous landscape. *Figure 3.3* presents a TMS bands 7,5,3 (TM equivalent 4, 3, 2) false colour composite image with the tower location indicated by the crosshair. The TMS image has not been geometrically corrected and therefore the distortions are unknown, but as a guide to the dimensions the y-dimension of the image is approximately 2km. The variation in land cover in the immediate vicinity of the tower suggests that the landscape is not homogenous and derivation of surface albedo at the 1.1km spatial scale of MODIS from point ground measurements should consider typical albedos of different land cover types in the vicinity of the tower to avoid bias in spatially scaling point ground measurements.

In order to capture the spatial variability of albedo at high resolution within a coarse resolution pixel it had been intended to use the linear mixture model derived from the ground measurements (§6.1). Proportions of the four scene elements in each pixel would have been obtained through spectral unmixing based on pure endmember spectra. However, this approach was not possible to implement on several accounts. The original intention had been to perform the spectral unmixing on the accurately georegistered 30m resolution level 9 LANDSAT TM, but the presence of cloud and cloud shadow directly over and in the vicinity of the tower precluded analysis. AVIRIS 20m resolution data was considered as an alternative, but the flight lines were flown such that the tower site appears at the very edge of one scene and the adjacent flight line was flown too far

west to overlap. Finally, although the TMS data is cloud / cloud shadow free and imaged with the tower in the centre of the flight line it was not possible with the resources and time available to geocorrect the data to be able to co-locate the ground measurements with specific pixels in the images.

Given that a pixel level spectral unmixing approach was not possible, an alternative land cover classification based spatial modelling approach was undertaken using the 12m resolution TMS data based on assigning typical albedos to land cover classes. This approach does not suffer from the limitations identified in §2.1.3 which are valid at regional and global scales rather than the local scale under consideration for the analysis presented in this study.

A 2.2km x 2.2km area of the TMS data with the AVHRR pixel containing the tower in the central 1.1km x 1.1km portion (*figure 6.6*) was selected as the area of interest and classified using the unsupervised classification function in ERDAS IMAGINE (ERDAS, 1997). This employs the ISODATA algorithm which performs clustering based on a minimum spectral distance to create clusters. The process was initialised with arbitrary cluster means for a ten dimensional feature space defined by TMS bands 1 through 10. Twenty clusters were generated which were then amalgamated into three classes, "shrubs and soil," "grass" and "grass and soil" reflecting the relative dominance of mesquite / yucca, grass and soil cover (*figure 6.7*). Assignment of each of the ten clusters to the three classes were made through visual assessment of various false colour composite images derived from the 4 metre resolution TMS data (*figure 3.3*), the partially overlapping portion of the AVIRIS imagery and photographs of the study area taken from the top of the tower (*figure 3.2a-c*).

Classification of the 2.2km x 2.2km area permitted a sensitivity analysis to be performed and provides an evaluation of the sensitivity of albedo to misregistration between the various measurement scales. The relative proportions of the three land cover classes have been extracted for nine 1.1km x 1.1km areas of interest as defined in *figure 6.6*. Area 5 corresponds to the central 1.1km x 1.1km and areas 1-4 and 6-9 correspond to various 0.5km displacements. *Table 6.7* presents the proportions of each land cover class extracted for each of the nine 1.1km x 1.1km areas together with the broadband albedos derived from these figures.

In order to calculate broadband albedo at the 1.1km and 2.2km resolution, *typical* albedos were assigned to the three classes in the classified TMS scene derived from the albedometer measurements (*table 6.8*). The “shrub and soil” class was characterised by the mean of the measurements from the short north and west transects. Measurements from the short south and east transects were excluded given the occurrence of grassy areas in these directions. The albedo selected for the “grass” class was taken as the mean of several locations at the midpoint of the 1km long east transect which traverses a grassy plateau. Ground based measurements were not made for the “grass and soil” class and an estimated albedo was assigned. Examination of the TMS hyperspectral profiles of the three classes indicates that the “grass and soil” class is located approximately midway between the other classes. A mean albedo of the two known classes was therefore assumed.

In deriving visible broadband albedo as outlined in §4.1.1.1 low and high aerosol optical thickness cases were considered, but as *table 6.7* shows, the influence of this atmospheric characterisation as before is small, in the third decimal place. For the central cell (5), all three broadband albedos compare favourably with those derived through narrowband to broadband

conversion, although those derived from the land cover classification are consistently slightly lower. Total shortwave, visible and NIR broadband albedo estimates that are within 0.011 of those derived using narrowband to broadband conversion for the AVHRR tower pixel (*see column three, tables 6.5 and 6.6*). The final column in *tables 6.5 and 6.6* also present the mean of four AVHRR pixel in a 2.2km x 2.2km block to derive albedo estimates through the narrowband to broadband conversion to compensate for geolocation errors. Comparisons of these values to albedos derived through the land cover classification approach for the central cell indicate deviations of 0.019 or less.

Table 6.7 also presents broadband albedos derived using the land cover classification approach for eight other 1.1km x 1.1km pixels with various 0.5km displacements to test the sensitivity of the method to the assumed location of the AVHRR pixel. *Table 6.9* provides summary statistics for the nine 1.1km x 1.1km cells. The mean albedos for the cells exhibit only small deviations from the broadband albedo values calculated for the central cell (5). The variance of the broadband values indicates that derivation of albedo estimates using the land cover classification method should provide estimates of total shortwave, NIR and visible broadband albedo within 0.016, 0.023, 0.009 respectively at the 95% confidence level when locating the 1.1km x 1.1km AVHRR cell anywhere within a 2.2km x 2.2km centred on the AVHRR pixel believed to contain the tower site.

6.2.2 10 x 10 AVHRR broadband albedo map

Having shown that the broadband albedos derived from AVHRR compare favourably to ground based point measurements, a total shortwave albedo map at 1.1km resolution was generated through narrowband to broad band conversion to examine the spatial variability at a coarser

spatial scale. The tower pixel is located in the AVHRR pixel in the third row down, fifth column from the left (*figure 6.8*). Explanations for the spatial pattern can be made through consideration of a LANDSAT TM false colour composite which is presented with a 1.1km grid overlay (*figure 6.9*). As for the AVHRR broadband albedo map, the pixel containing the tower is in row three, column five, conveniently obscured by the cloud shadow!

For example, it is known that the area to the south east of the tower is characterised by a mixture of grassland and shrubs in contrast to the shrub and soil mixture to the immediate north and west of the tower. Measurements along a transect in a grassland area returned mean total shortwave albedo of 0.1801 and 0.2537 in the NIR which is noticeably lower than the mean albedo in the vicinity of the tower. From the TM false colour composite, it can be observed that the pixel in the sixth row down and penultimate column is almost totally characterised by a grey-green hue. This pixel is also associated with the lowest total shortwave broadband albedo in this extract. Pixels in its vicinity which also contain a high grassland cover also exhibit lower albedos with the magnitude determined by the amount of grass cover. The higher albedos of the 2 by 3 area at the top right of the image clearly correspond to an area whose scene elements provide a contrasting spectral signature and consequently prove to be a distinct feature on the albedo map.

However, it should be stressed that care is needed in using the false colour composite to explain the trends in the albedo map. Total shortwave broadband albedo is derived based on the entire spectrum from 305-2800nm, while the colour composite is generated using three bands which sample a small proportion of these wavelengths. As a consequence, for example, the pixel to the immediate south of the tower appears to have a grey-green tinge and while there is significant grass cover here in contrast to the north and west of the tower, as illustrated in the site

photographs (*figure 3.2c*) there is a graduation to sparse grass and soil to the west which cannot be identified in this false colour composite. Consequently although the TM image suggests that the pixel to the immediate south of that containing tower should have a lower albedo, the increasing amount of bare soil to the west as the grass become more sparse may be responsible for producing the slightly higher albedo for this pixel. Despite the limited qualitative evaluation of the broadband albedo map that is possible based on the TM false colour composite, it appears that despite all the assumptions and approximations made to derive AVHRR broadband albedo, the values are capturing genuine spatial trends in the landscape.

6.2.3 *POLDER broadband albedo through narrowband to broadband albedo conversion*

POLDER broadband albedos were derived through narrow to broadband albedo conversion for the pixel calculated to contain the tower at the transition site. Once again, *table 6.10* shows that negligible differences may be observed between values calculated for low and high aerosol optical thickness conditions. Although POLDER total shortwave albedo differs by less than 0.02 for albedos calculated using the various methods and measurements above, the visible and NIR broadband albedos exhibit a significantly different relationship. POLDER visible broadband albedo is noticeably higher and NIR broadband albedo noticeably lower than previously observed.

However, the POLDER sensor, with its 6km x 7km resolution at nadir, views a considerably larger footprint than both the ground measurements around the tower and the 1.1km resolution of an AVHRR pixel. To provide a estimate of broadband albedo at a larger spatial scale, the average albedos of the 10x10 AVHRR grid shown in *figure 6.9* were computed (*table 6.11*). The

POLDER visible broadband albedo exhibits excellent agreement to the values derived from the 10x10 AVHRR grid, however the POLDER total shortwave and NIR broadband albedos are significantly lower, differing by up to 0.044.

One possible reason for these observations is that the spline fitted to the POLDER spectral albedos may not characterise the spectral albedo curve effectively. The spline was fitted to spectral albedos at 490nm, 565nm, 765nm and 910nm with estimated tie points at 305nm and 2800nm. Thus, the spline is constrained by values in the lower part of the spectrum and hence the visible broadband albedo is well characterised but the spectral albedo curve in the NIR appears to be underestimated which consequently also leads to the total shortwave albedo being underestimated.

To investigate this hypothesis, a conceptually similar process to that outlined in §5.3.2 was employed. As undertaken for AVHRR, the AVIRIS reflectance profile was adjusted using a function of the form $y=mx+c$. Since four POLDER spectral albedos are available to constrain the AVIRIS curve, the stretch (m) and translation (c) factors were obtained by performing a least squares regression with AVIRIS and POLDER as the dependent and independent variables respectively. The broadband albedos produced using this approach are presented in *table 6.12* and as observed previously little difference is observed between the values derived for low and high estimates of aerosol optical thickness. Deriving broadband albedo in this way as provides values that are within 0.01 for total shortwave, NIR and visible broadband albedo for the 10x10 AVHRR block (*cf tables 6.11 and table 6.12*). This analysis suggests that the spline generated based on the four POLDER spectral albedos fails to sufficiently characterise the spectral albedo profile and hence provides underestimates of total shortwave and NIR broadband albedo. A better

approximation is obtained through applying a stretch and translation to the hyperspectral AVIRIS reflectance profile which is closer to the unknown truth of the spectral albedo curve than derived through fitting a spline to the four measured POLDER spectral albedos.

6.2.4. *Summary: multiple scale albedo comparison*

Figures 6.10 and 6.11 summarise graphically the broadband albedos at various scales presented above. *Figure 6.10* also places the observed total shortwave values in the context of the range associated with a variety of land cover classes derived from the literature, excluding snow and ice.

The albedo values plotted in column one of *figure 6.10* are derived in all but one case from ground based albedometer measurements. Mean daily clear sky summertime albedos are extracted for six surfaces from figure 5 in LaFleur *et al.* (1997). The mean daily total shortwave broadband albedos are: lake 0.055, sedge tundra 0.112, open spruce and tamarack forest 0.12, birch/willow (shrub) forest 0.161, beach ridge 0.163 and mixed tundra 0.173. Values are also taken from Allen *et al.* (1994) who report total shortwave broadband albedo for two contrasting semiarid Sahelian environments in Niamey, Niger. The agricultural fallow, consisting of a ground layer of annual herbs and grasses, scattered shrubs and occasional trees, exhibited an annual mean albedo of 0.22 with minimum and maximum monthly mean albedos of 0.177 and 0.242 respectively. A contrasting open natural forest (tiger bush), consisting of dense bands of dense vegetation and areas of bare crusted soil, exhibited an annual mean albedo of 0.25 with minimum and maximum monthly albedos of 0.212 to 0.269 respectively. Finally, the range of surface albedos estimated from ERBE data for the brightest desert, the Sahara (Li and Garand, 1994), is plotted.

These albedo values, associated with various non snow and ice surfaces, represent a range of total shortwave broadband albedo values that could be derived for a site whose characteristics are unknown other than that snow and ice cover is absent. The minimum and maximum total shortwave broadband albedos at Jornada form a subset of this broad range and exhibit comparable values to those observed in the broadly similar landscapes of Niger. Lowest total shortwave albedo was associated with grass dominated sites and the highest where soil cover was predominant. The range of total shortwave broadband albedo associated with the constituent land cover classes is 0.08 and clearly attempting to characterise the Jornada landscape at a coarser spatial scale than that of a single ground based albedometer measurement could be significantly biased.

The mean and one standard deviation of the 44 total shortwave broadband measurements made along the short transects at the tower site are plotted in column 3 of *figure 6.10*. Mean values without error bars are plotted for the total shortwave, visible and NIR in *figure 6.11*. Comparison with the points plotted in columns 5 and 6 indicate that the mean of the measurements around the tower characterise albedo derived at a variety of spatial scales in the landscape from AVHRR and POLDER. Bias in the values derived from using the spectral albedo profile derived through splining the POLDER measurements is apparent in column 6 of *figure 6.11* such that the total shortwave and NIR albedos are underestimated and the visible is overestimated.

Returning to column 5, the values plotted from left to right are derived for just the AVHRR pixel containing the tower, the 2x2 AVHRR block and the 10x10 AVHRR block. The error bars in *figure 6.10* for the total shortwave broadband albedo 10x10 AVHRR block represent one standard

deviation and comparison of the hue of the tower pixel to the rest of the image in *figure 6.8* suggests that the comparison at the coarser spatial scale is favourable given that the mosaic of shrubs and soil and grass around the tower produces an albedo which approximately midway between the minimum and maximum observed over the larger area.

This qualitative evaluation is quantifiable, at least at the 1.1km x 1.1km and 2.2km x 2.2km scale, on the basis of the mean derived from the land cover classification method using typical albedos of three land cover classes to derive albedo. In other words, through spatial modelling it is possible to show quantitatively that the transect measurements which sampled sites in both the shrub and soil and the grass areas, provide a good approximation to the spatial variability at coarser scales in this landscape. If the tower site had been located in a region of higher albedo as observed to the south of *figure 6.8* or possibly even in the shrub and soil area to the immediate west of the tower (*see figure 3.3*), it is unlikely to have compared as favourably to the mean of the landscape at coarser resolutions.

It is worthwhile stressing that validation, defined in the strictest sense, is impossible because ground based measurements can only at best provide an good estimate of the unknown truth of the albedo at satellite spatial resolutions. It is not inconsistent with this perspective however to conclude that the results from this analysis suggest that favourable comparisons are attainable between ground based samples and coarse scale satellite measurements. These favourable comparisons provide a first step towards defining a validation approach to derive a confidence estimate in the albedos derived from MODIS and therein, by definition, a validation of the operation of the retrieval algorithms. If similar findings to those reported in this study are achieved in other landscapes, such as forest and agriculture, confidence may be placed in the

satellite derived values. In other locations, the location of the tower site may not capture the heterogeneity of the landscape, as was the case for Jornada, and thus spatial modelling through land cover classification may be essential to model variation in albedo over a larger area. In doing this, it would therefore be essential to survey the landscape away from the tower to identify component land cover classes and make sufficient measurements to characterise each with a reliable typical albedo.

Table 6.1: Regression model coefficients using percent albedo values without corrections for either solar zenith angle or soil moisture effects. * significant at the 95% significance level

Variable	Total Shortwave Parameter Estimate	NIR Parameter Estimate
Soil	18.7319*	26.9154*
Grey (dormant) vegetation	-1.0100	-1.2063
Woody vegetation	2.2694	2.2751
Live vegetation	9.6038*	13.5174*

Table 6.2: Regression model coefficients using percent albedo values corrected for solar zenith angle effects, but not for soil moisture effects. * significant at the 95% significance level

Variable	Total Shortwave Parameter Estimate	NIR Parameter Estimate
Soil	18.3382*	26.5217*
Grey (dormant) vegetation	-0.8117	-1.008
Woody vegetation	2.2120	2.2257
Live vegetation	8.3932*	12.3068*

Table 6.3: Regression model coefficients using percent albedo values corrected for solar zenith angle and soil moisture effects. * significant at the 95% significance level

Variable	Total Shortwave Parameter Estimate	NIR Parameter Estimate
Soil	17.6671*	25.8978*
Grey (dormant) vegetation	6.8581*	6.1305*
Woody vegetation	0.3108	0.4462
Live vegetation	5.9482*	10.0310*

Table 6.4: Observed and predicted total shortwave and NIR broadband albedo for seven sites at the end of the long east transect.

Site identifier	Observed total shortwave albedo	Predicted total shortwave albedo	Observed NIR albedo	Predicted NIR albedo
1	0.2385	0.2373	0.3366	0.3385
2	0.2350	0.2380	0.3359	0.3398
3	0.2204	0.2202	0.3240	0.3144
4	0.2538	0.2398	0.3558	0.3420
5	0.2572	0.2496	0.3652	0.3588
6	0.2351	0.2350	0.3438	0.3355
7	0.2293	0.2276	0.3322	0.3241

Table 6.5: Comparison of mean broadband albedo from the 44 transect sample sites and broadband albedos derived from AVHRR for the pixel containing the tower and those below, to the right and below right. Diffuse and direct irradiance used in the calculation of the AVHRR broadband albedos have been derived using the *high* aerosol optical thickness estimate.

Mean albedo	44 Transect Measurements	AVHRR tower pixel	Below AVHRR tower pixel	Right of AVHRR tower pixel	Below right AVHRR tower pixel	Mean of AVHRR pixels
Total shortwave	0.2209	0.2242	0.2321	0.2276	0.2244	0.2271
Visible	0.1244	0.1272	0.1436	0.1381	0.1290	0.1345
NIR	0.3106	0.3114	0.3115	0.3080	0.3101	0.3102

Table 6.6: Comparison of mean broadband albedo from the 44 transect sample sites and broadband albedos derived from AVHRR for the pixel containing the tower and those below, to the right and below right. Diffuse and direct irradiance used in the calculation of the AVHRR broadband albedos have been derived using a *low* aerosol optical thickness estimate.

Mean albedo	44 Transect Measurements	AVHRR tower pixel	Below AVHRR tower pixel	Right of AVHRR tower pixel	Below right AVHRR tower pixel	Mean of AVHRR pixels
Total shortwave	0.2209	0.2227	0.2296	0.2253	0.2226	0.2251
Visible	0.1244	0.1260	0.1409	0.1355	0.1273	0.1324
NIR	0.3106	0.3096	0.3093	0.3058	0.3082	0.3082

Table 6.7: Proportional cover of three land cover classes and broadband albedo values calculated using the land cover classification method for nine 1.1km x 1.1km cells within a 2.2km x 2.2km area centred on the AVHRR pixel containing the tower at the transition site (cell 5).

Cell	Proportion of			Total shortwave	Broadband albedo		
	“Grass”	“Shrub and soil”	“Grass and soil”		NIR	Visible (low AOT)	Visible (high AOT)
1	0.006	0.989	0.005	0.2254	0.3223	0.1221	0.1211
2	0.390	0.603	0.007	0.2101	0.3008	0.1134	0.1124
3	0.611	0.385	0.004	0.2014	0.2886	0.1084	0.1075
4	0.001	0.990	0.009	0.2255	0.3225	0.1221	0.1211
5	0.233	0.756	0.012	0.2162	0.3095	0.1169	0.1159
6	0.425	0.570	0.004	0.2087	0.2990	0.1126	0.1117
7	0.073	0.771	0.156	0.2197	0.3144	0.1188	0.1179
8	0.244	0.659	0.097	0.2141	0.3065	0.1157	0.1147
9	0.388	0.597	0.015	0.2100	0.3007	0.1133	0.1124

Table 6.8: Typical albedo values assumed to characterise the three land cover classes used to derive broadband albedo at the satellite scale using the land cover classification approach.

Land cover class	Total shortwave broadband albedo	NIR broadband albedo
Shrubs and soil	0.2257	0.3228
Grass	0.1860	0.2670
Grass and soil	0.2058	0.2949

Table 6.9: Summary broadband albedo statistics for the values derived from land cover classification for the nine 1.1km x 1.1km cells extracted from the TMS data.

Broadband albedo	Mean	Standard Deviation	Minimum	Maximum
Total shortwave	0.2146	0.0080	0.2014	0.2255
NIR	0.3071	0.0113	0.2886	0.3225
Visible (low AOT)	0.1159	0.00461	0.1084	0.1221
Visible (high AOT)	0.1151	0.0045	0.1075	0.1211

Table 6.10: Broadband albedo generated by spling for the POLDER pixel containing the tower at the transitional site with atmospheric characterisation for low and high aerosol optical thickness.

Broadband albedo	Low aerosol optical thickness	High aerosol optical thickness
Total shortwave	0.2069	0.2065
Visible	0.1491	0.1486
NIR	0.2670	0.2667

Table 6.11: Broadband albedo generated for the 10x10 AVHRR grid shown in *figure 6.8*.

Broadband albedo	Low aerosol optical thickness	High aerosol optical thickness
Total shortwave	0.2230	0.2318
Visible	0.1415	0.1434
NIR	0.3095	0.3111

Table 6.12: Broadband albedo generated for the POLDER pixel by adjusting the AVIRIS reflectance curve for low and high aerosol optical thickness conditions.

Broadband albedo	Low aerosol optical thickness	High aerosol optical thickness
Total shortwave	0.2230	0.2224
Visible	0.1340	0.1335
NIR	0.3030	0.3022

7. CONCLUSIONS AND LESSONS LEARNED

This study has presented an evaluation of instrumentation and sampling strategies for validation of albedo at satellite spatial scales in the context of the Grassland PROVE initiative. As the name of the campaign implies, the field experiment at Jornada was very much a prototyping exercise. Many important lessons were learned. Firstly, some simple improvements could have been made to basic planning, preparation and record keeping.

The crucial importance of comprehensive field notes and cross-referencing aids, and the frustration associated with problems with analysis once back in the office was very much learnt through this study. Considerable problems were encountered relating the hemispherical photography to the coincident albedometer measurements. This was due to poor and inconsistent field notes associated with the photography which lead to misidentification of many of the hemispherical photograph locations. These were only finally resolved by very careful scrutiny of the, often terse, qualitative descriptions of the transects locations. The paucity of notes prevented several sites that it had been hoped to include in the analysis from being cross referenced. A simple scheme by writing a identifier such as “East 1” on a whiteboard attached to the tripod could have provided a unique reference in each photograph and prevented confusion. The cross referencing would also have been simplified with more comprehensive qualitative descriptions of each location.

In addition, the acquisition of panoramic photographs along the length of the transects would also have been a useful permanent record of the variability in the land cover components. With the greater availability and lowering cost of digital cameras, acquisition in this way rather than using

standard film would permit the resource to be easily shared by researchers from disparate home institutions with little effort.

Secondly, lessons were learned about the factors that may confound analysis and introduce bias unless accounted or corrected for. Soil moisture effects and to a lesser degree solar zenith angle effects exert a noticeable influence on albedo measurements such that the observed spatial albedo variations were reproducible in a relative sense, but with shifts in absolute magnitude between different days. Soil moisture had a very significant influence on the albedo measurements preventing amalgamation of results for different days until a correction had been applied. The quantitative spatial modelling using the albedometers and hemispherical photography provides various lessons for the acquisition of ground measurements.

It is preferable that ground measurements are collected on the same day as the satellite overpass and ideally at the same time. Collection of ground measurements on another day could introduce significant bias such as that observed in this study due to differing soil moisture conditions given the influence of a modest precipitation event the previous day. While one approach would be to establish a means to characterise soil brightness to determine the effects of soil moisture variations, corrections for effects such as these will be at best rough approximations because the value of the correction will be determined by the proportions of the various scene elements for a given location. It is therefore suggested that all measurements be acquired on a single day and if possible not following rainfall the previous day which could lead to a change in brightness as the soil dries.

The results in this study and previous research (*e.g.* Barker Schaaf and Strahler, 1994; Lafleur *et al.*, 1997) suggest that the influence of solar zenith angle effects on broadband albedo measurements is minimal except at high solar zenith angles. Given that a short 100m transect consisting of 11 measurements can be measured in approximately thirty minutes it would be feasible to collect a complete data set of measurements along several transects in the couple of hours around solar noon. To remove any small residual solar zenith angle effect it would however be advisable, to operate several additional unattended fixed location and continuously recording albedometers to be able to derive a solar zenith angle correction.

These fixed location albedometers could also serve two further purposes. Firstly, they would provide a record of changes in downwelling conditions due to the influence of changing atmospheric corrections. For example such an approach could be used to monitor high thin cirrus moving over the scene. The “clear sky” conditions provide a ceiling in the albedo curves and dips can be associated with clouds passing over. To perform corrections it is important to accurately time tag all measurements.

Secondly, fixed location albedometers could be positioned at locations characterised as “pure” endmember sites to quantify the albedo of each of the individual land cover components. Collection of “pure” endmember albedos would assist in the definition of the linear mixture model and quantification of the relative influence of each on the composite signal. Model evaluation could be performed by testing whether the albedo could be derived for the cases for which only a single land cover component class occupies the entire scene. Given that it is unlikely to be able to find an area entirely composed of a single land cover component with a tripod height of 4.14 metres, it is suggested that a tripod height be reduced to the scale of a bare patch of soil,

large mesquite bush *etc.* In this way, although precluded in this study, spatial modelling of the landscape could be derived from a model relating ground based albedo measurements to scene elements extracted at the sub-pixel scale. However, if a land cover classification approach is taken, which is advised if the sub-pixel spatial modelling is not, to assess and account for the heterogeneity of the landscape, albedo measurements and transects should also be planned to acquire reliable estimates of typical albedos of the land cover classes identified in the landscape rather than just for individual scene elements at the sub-pixel scale.

Attention to seemingly small details would also minimise the influence of other sources of error. Especially if repeat measurements are planned to evaluate the change of albedo for a given site over time, care should be taken to locate the tripod over a clearly marked location with a consistent orientation of the albedometer / camera. For example, with the albedometer mounting pole parallel to the direction of the transect. Hemispherical photography should be acquired using a camera mounted on a separate tripod immediately after the albedo measurements. Obtaining it at a different time or on a different day with differing cloud cover would make it impossible to quantify the shadow component in the scene. Also, although the albedometers were mounted on a sturdy tripod, the set-up was susceptible to tipping over due to gusts of wind. Attention therefore needs to be given to devising a simple method to secure or weight down the tripod.

Hemispherical photography should be acquired using a 180° FOV fish eye lens such that the total area viewed by the albedometers is captured in the images to avoid any bias by omitting those pixels which are beyond the 75° limit of the lens. It may also be beneficial to use a NIR sensitive film to assist in separation of the photosynthetic and non-photosynthetic components in the photography. A sufficiently long camera trigger cord or infrared control should be used to

eliminate obstacles in the photograph and restrict the unclassified part of the scene to that occupied by the tripod. Several scale bars should also be placed radial to the centre of each photograph to provide a visual assessment of distances and distortions in the hemispherical photographs.

Thirdly, lessons were also learned with regard to the methodology used to perform narrowband to broadband albedo conversion. Based on the results from POLDER, it is suggested that more accurate results may be achieved by constraining an hyperspectral reflectance curve from high resolution data such as AVIRIS than by fitting a spline to a limited number of spectral albedo values, which was four in the case of POLDER. It is suggested that by constraining the AVIRIS reflectance curve using spectral albedos derived from POLDER, that the resultant profile is closer to the unknown truth of the actual spectral albedo profile than that achieved by splining. Further investigations into the relationship between a hyperspectral reflectance curve and a spectral albedo curve for the same surface would be valuable to assess this approach.

Locating a tower at a validation site should be carefully planned. To maximise the likelihood of a single albedometer characterising the landscape at the 1km scale of the MODIS albedo product, the location should be such that at coarse resolution the landscape can be considered homogenous. In the case of Jornada, such sites would be within an area entirely composed of a shrub and soil mixture, as to the west of the road shown in the TMS data (*figure 3.3*) or within the grass dominated area to the south-east of the tower. If the tower is located in a heterogeneous area, as at Jornada with shrub and soil to the north and west and a higher grass cover to the south and east, ground based albedo measurements to characterise the spatial variability of albedo and to enable spatial modelling to a coarser scale are strongly advised. At Jornada, the 44 transect

measurements which would likely sample the area viewed by an albedometer mounted at a higher elevation on a tower rather than on a tripod, happened to be located at a site which by chance integrated the signal from the shrub and soil and grassier areas to produce a mean albedo characteristic of the broader landscape. Therefore it is advised to work with scientists who have an intimate knowledge of the landscape and to consult high resolution hyperspectral imagery in deciding the location of a tower and the ground based sampling strategies required to capture the spatial variability of albedo.

APPENDIX A: FIGURES

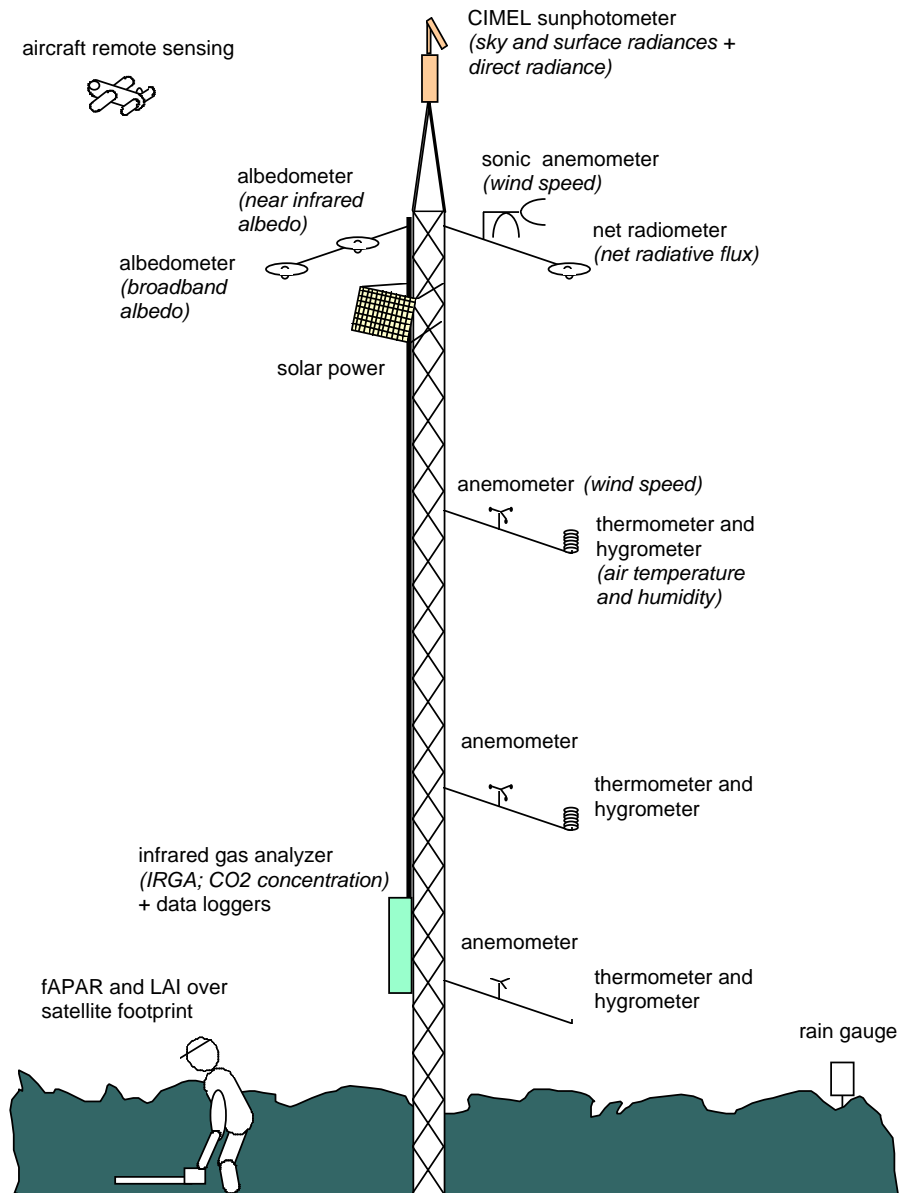


Figure 1.1: Schematic illustrating the continuous flux tower instrumentation that is planned for most Core Validation Test Sites and the periodic but less frequent transect sampling (requiring airborne and/or ground-based personnel). Source: Privette *et al.* (1997a).

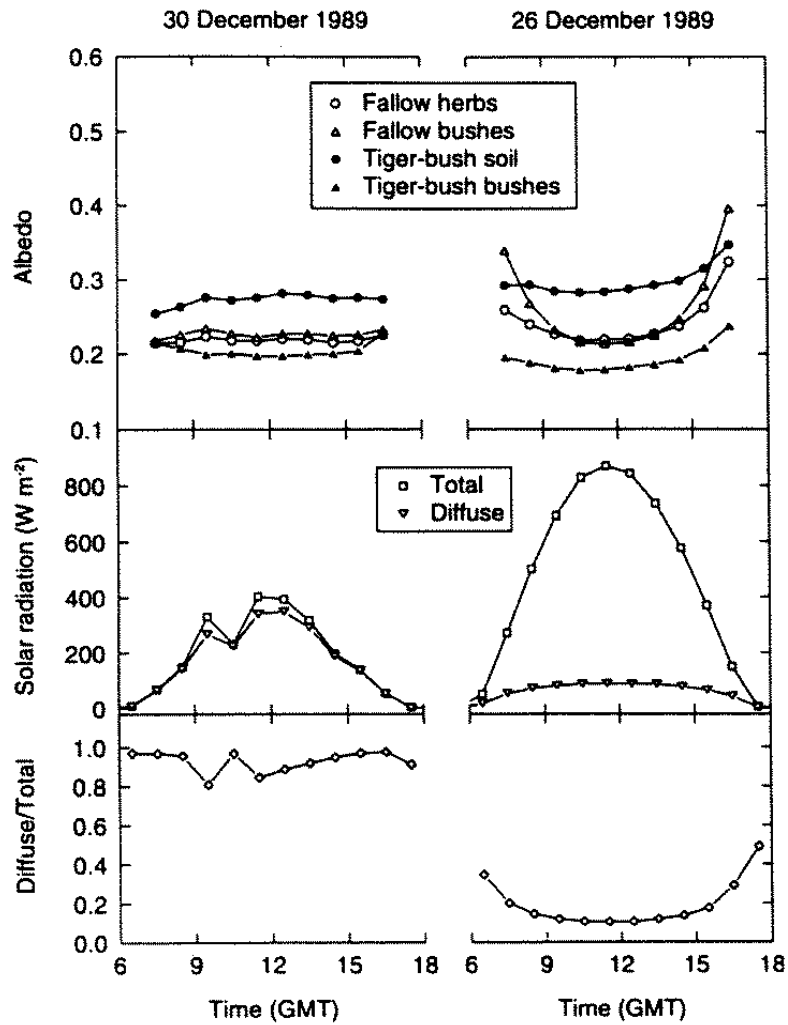


Figure 2.1: Diurnal variation in albedo over four surfaces at two sites in south-western Niger for a typical cloudy day (30th December 1989) and a typical clear day (26 December 1989) during the dry season. Incoming shortwave radiation and diffuse / total shortwave ratio is also shown for the fallow site. Source: Allen *et al.* (1994).



Figure 3.1: Location of Jornada Experimental Range study site (marked by JRN). Source: <http://jornada.nmsu.edu>



Figure 3.2a: View of the study site from the top of the transitional tower with the dirt road running north into the photograph. The landscape to the north and west of the tower is characterised by a mosaic of shrubs (mesquite and yucca) and soil with some grass and herbs. Photograph taken by Paul Hobson (University of Wales, Swansea).



Figure 3.2b: View of the study site from the top of the transitional tower with the dirt road running south into the photograph. The landscape to the south and east of the tower is characterised by a denser coverage of grass with some scattered shrubs. Photograph taken by Paul Hobson (University of Wales, Swansea).



Figure 3.2c: View of the study site from the top of the transitional tower looking to the south west. Note the two distinct surface coverages. The shrub and soil mosaic is replaced by a shrub devoid area to the south. This zone exhibits a transition from grass to a sparse grass and soil mixture from east to west. Photograph taken by Paul Hobson (University of Wales, Swansea).

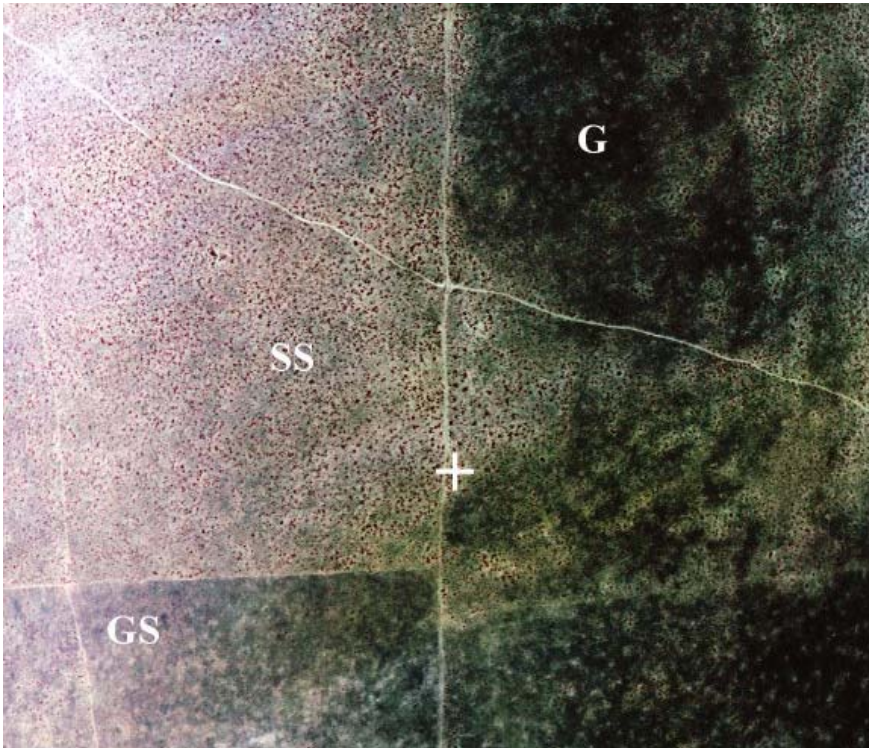


Figure 3.3: False colour composite derived from 4m resolution Thematic Mapper Simulator data using bands 7,5,3 (TM equivalent 4,3,2). The tower location is marked by a cross hair and examples of the land cover classes grass: (G), shrub and soil (SS) and grass and soil (GS) are identified. Note that view angle effects introduce brightness variations across this image.

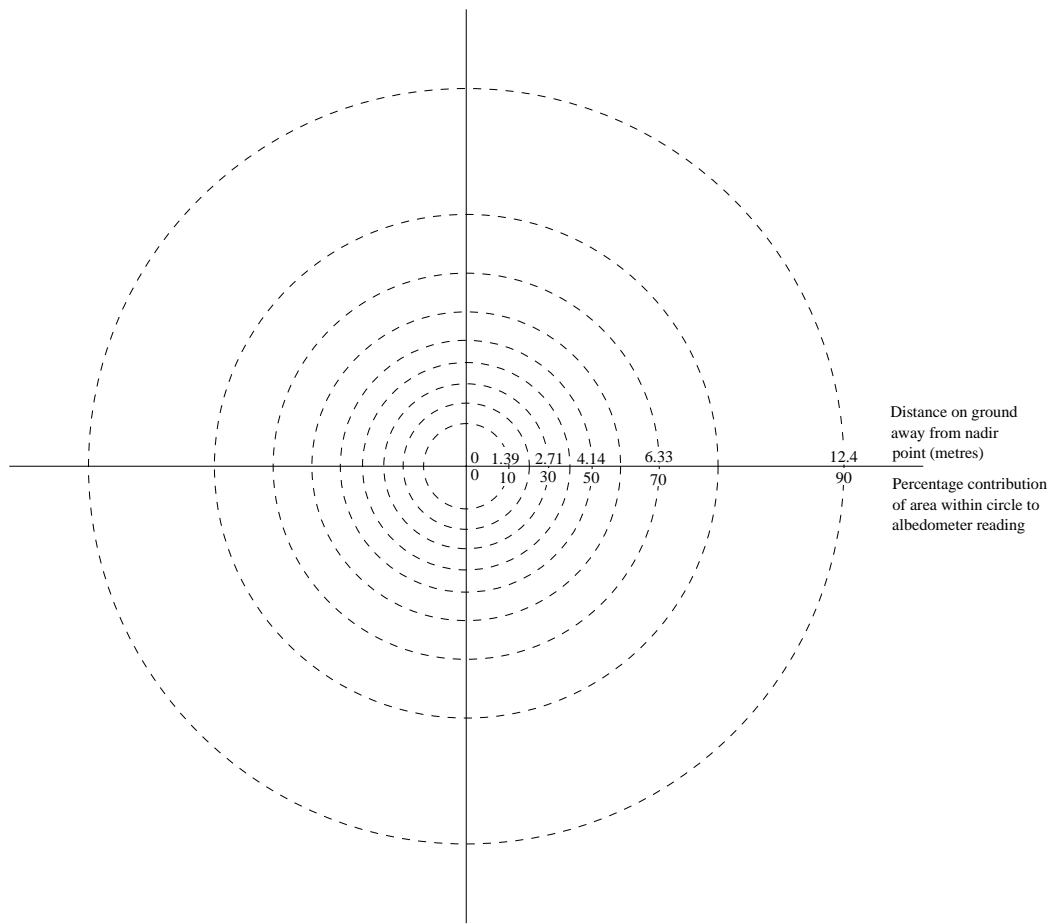


Figure 4.1: Spatial response function of albedometer with respect to a flat surface. The concentric circles are plotted at 10% increments, such that the pixels in the area between any two adjacent circles contribute 10% of the information content of the total signal recorded by the instrument. The assumed height of the albedometer above the surface is 4.14m.



Figure 4.2: Albedometer instrument setup: the total shortwave and NIR broadband albedometers mounted on either end of a pole secured to the top of a black tripod at a height of approximately 4 metres above the surface. The albedometer mounting was replaced by the camera with a fish eye lens for the acquisition of hemispherical photographs from the same height as the albedo measurements. Photograph taken by Paul Hobson (University of Wales, Swansea).

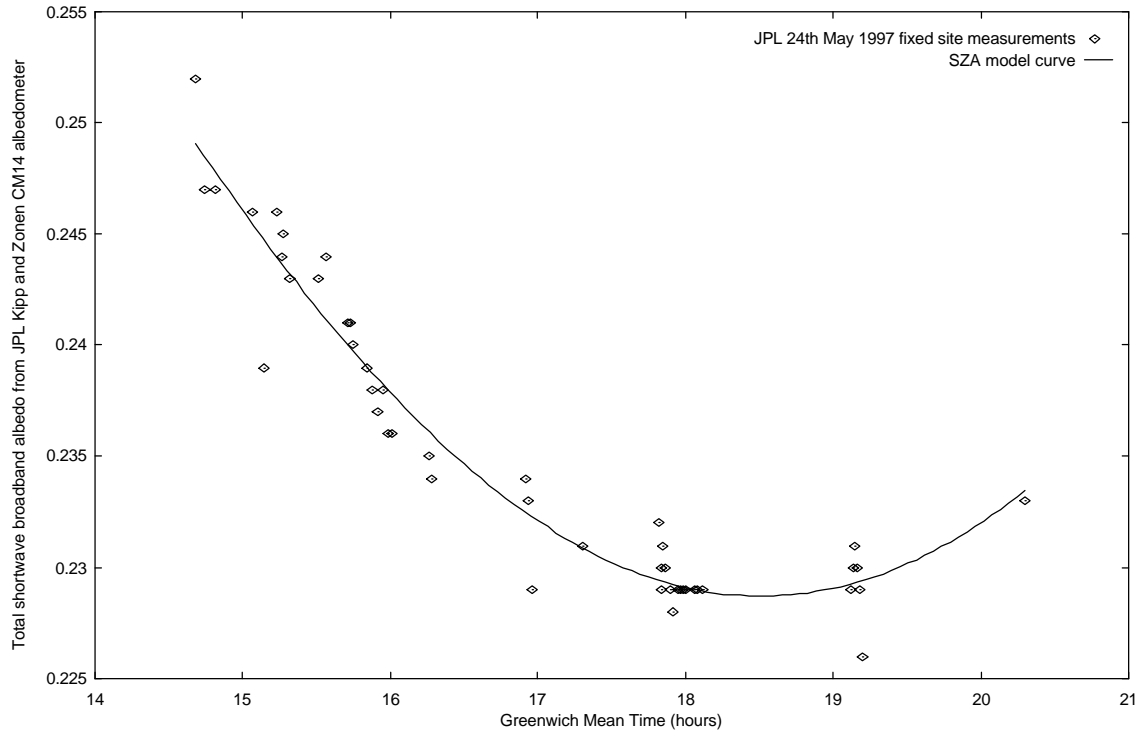


Figure 4.3: Derivation of solar zenith angle correction model by fitting a curve to a semi-diurnal time series acquired by the JPL team using their total shortwave broadband Kipp and Zonen CM14 albedometer for a fixed location at the transitional site on 24th May 1997. Local time at Jornada (MDT) was 6 hours earlier than GMT (*i.e.* GMT-6). The form of the model is: $0.2753 + (0.0466 * \sin(0.2546 * x))$, where x is decimalised Greenwich Mean Time.

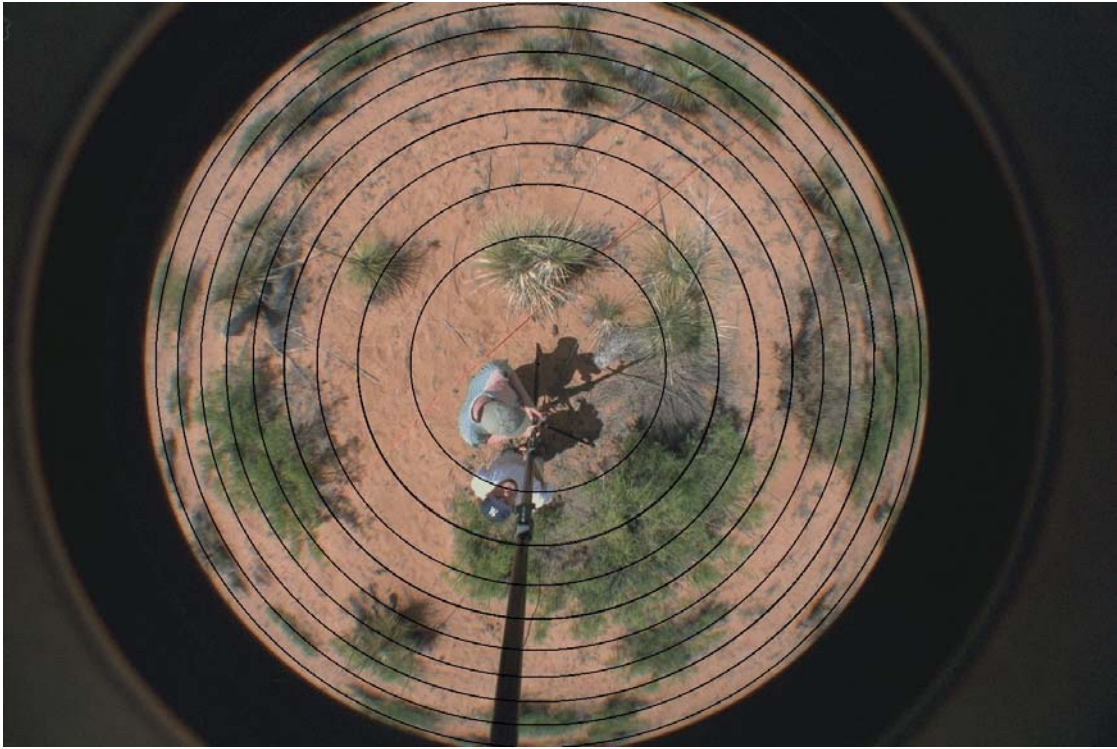


Figure 4.4: Spatial response function of the albedometer overlaid on a hemispherical photograph. The concentric circles are plotted at 10% increments, such that the pixels in the area between any two adjacent circles contribute 10% of the information content of the total signal recorded by the instrument.

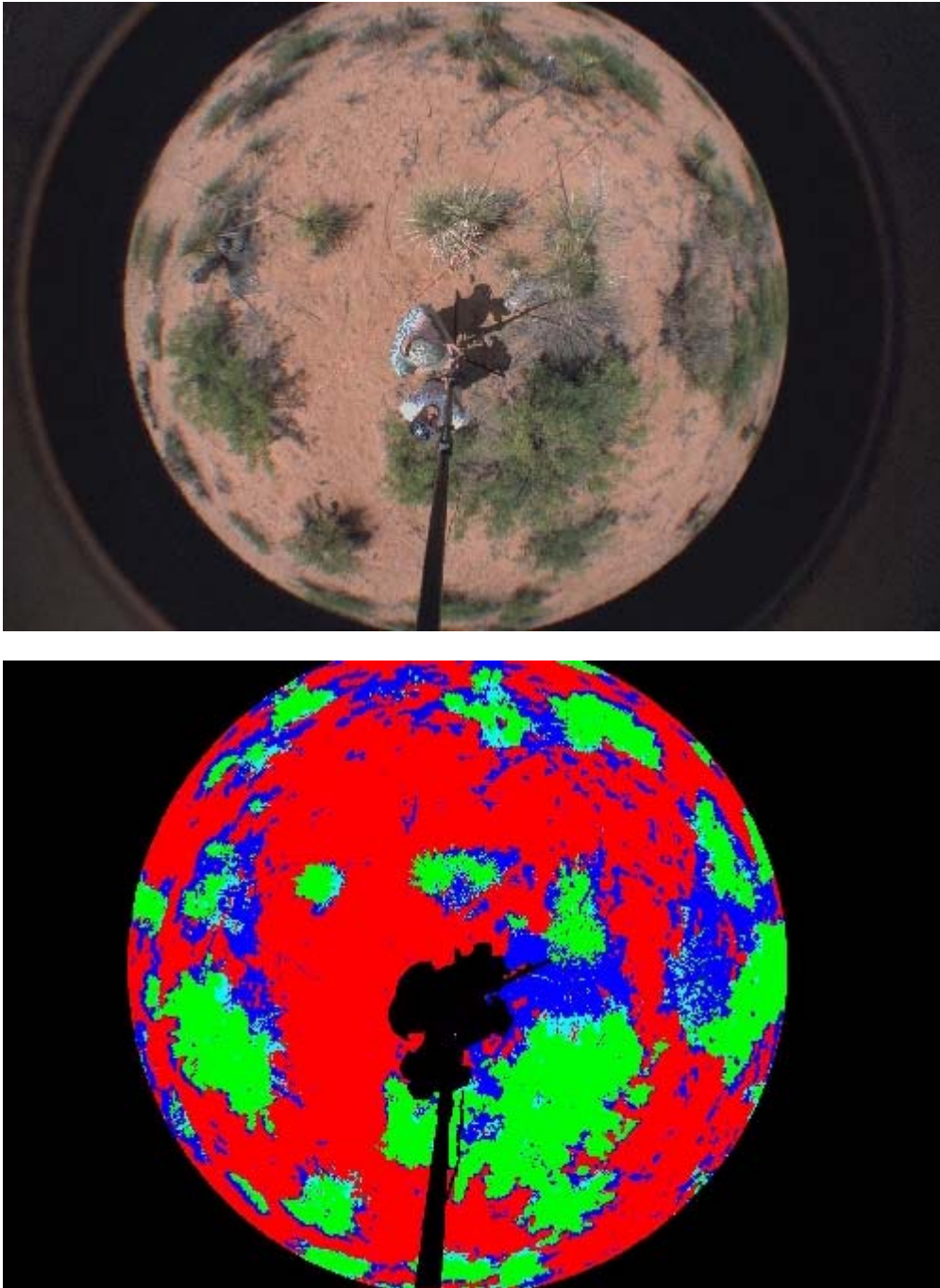


Figure 5.1a: Hemispherical photograph (top) and classified image (bottom) of site 9 on the north transect which is characteristic of a high vegetation location. Classification key: Red: soil, Green: live vegetation, Blue: grey vegetation, Cyan: dead / woody vegetation.

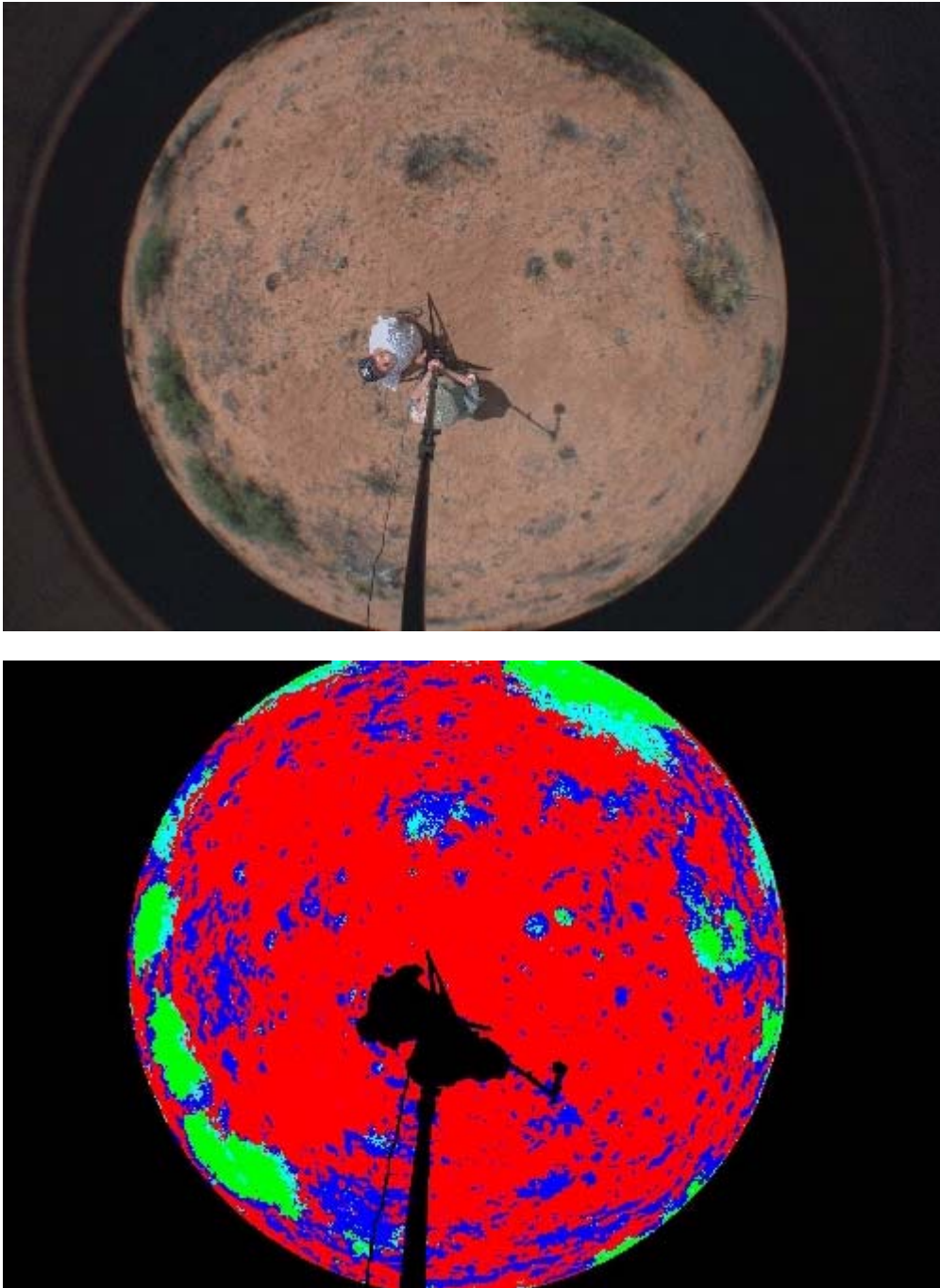


Figure 5.1b: Hemispherical photograph (top) and classified image (bottom) of site 6 on the north transect which is characteristic of a low green live vegetation location. Classification key: **Red:** soil, **Green:** live vegetation, **Blue:** grey vegetation, **Cyan:** dead / bare woody vegetation.

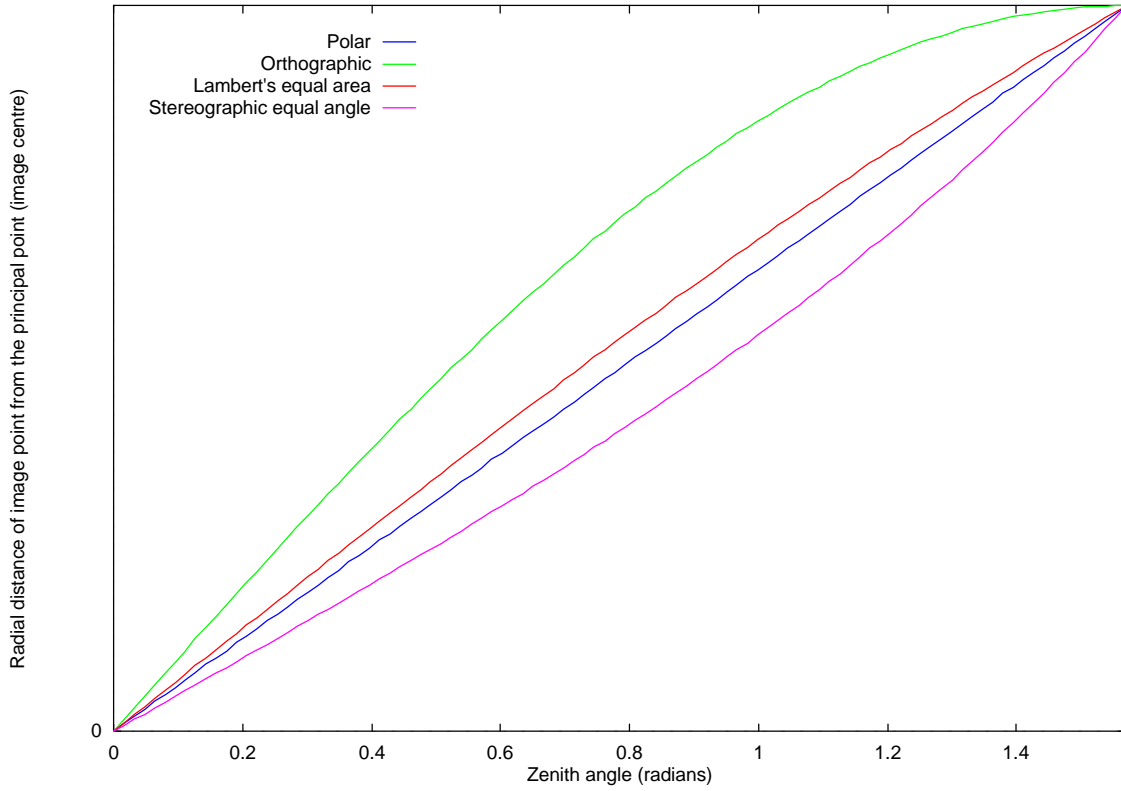


Figure 5.2: Four different types of projection that characterise fisheye lenses as identified by Herbert (1987 in Boulianne *et al.* 1997). The associated equations are: polar: $r = 2R\xi/\pi$, orthographic: $r = R \sin(\xi)$, Lambert's equal area: $r = (2R/\sqrt{2})\sin(\xi/2)$, stereographic equal angle: $r = R \tan(\xi/2)$, where R is the radius of the hemispherical lens, ξ is the zenith angle and r is the radial distance of the image point from the principal point (image centre).

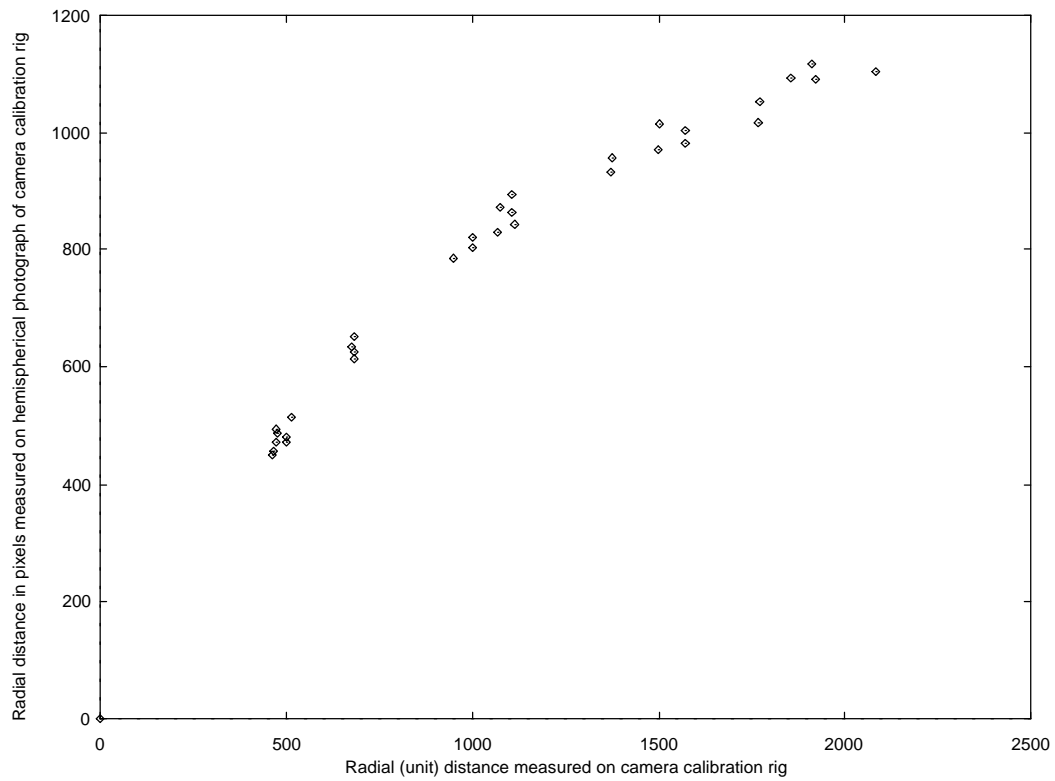


Figure 5.3: Plot of radial distance measured using high accuracy surveying equipment against distance derived from a hemispherical photograph for a camera calibration rig in the Department of Geomatic Engineering at UCL. The shape of the curve indicates that the lens is characterised by an orthographic projection.

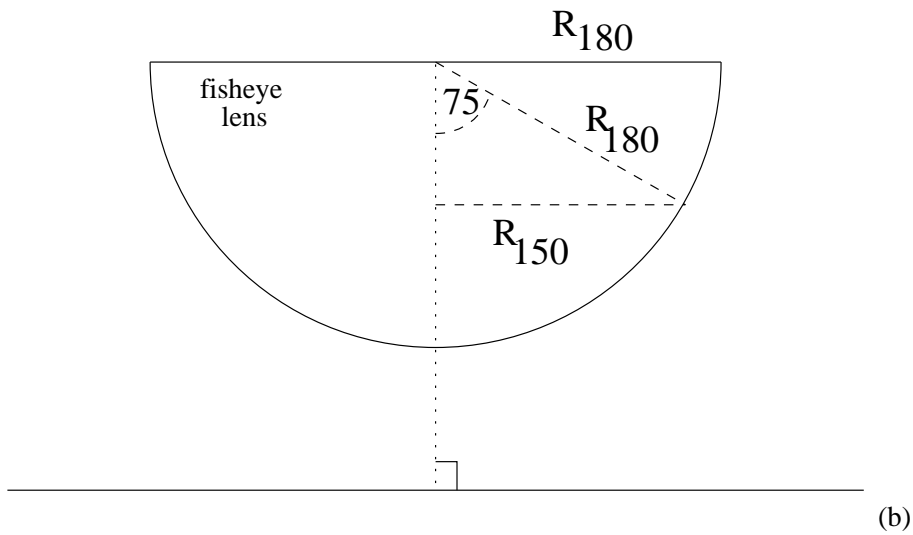
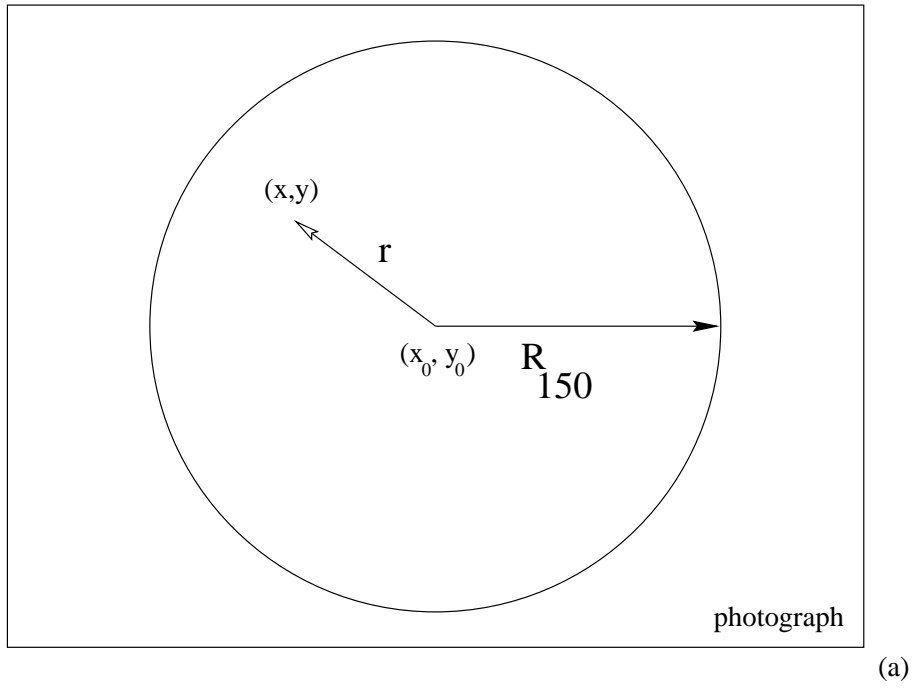


Figure 5.4: Definition of terms used in the derivation of the equation to determine R_{180} , the radius of the hemisphere / scene measured in pixels on a hemispherical photograph for a lens with a 180° FOV. Figure (a) shows a hemispherical photograph. The centre of the scene is at (x_0, y_0) and the radial distance (r) maybe be defined as the distance from the centre to any point in the scene (x, y) . R_{150} is the radius of a hemispherical lens with a 150° FOV. Figure (b) is a schematic of a hemispherical lens. The radius of the hemisphere of a 180° FOV may be calculated knowing the radius of a 150° FOV lens using the sine rule.

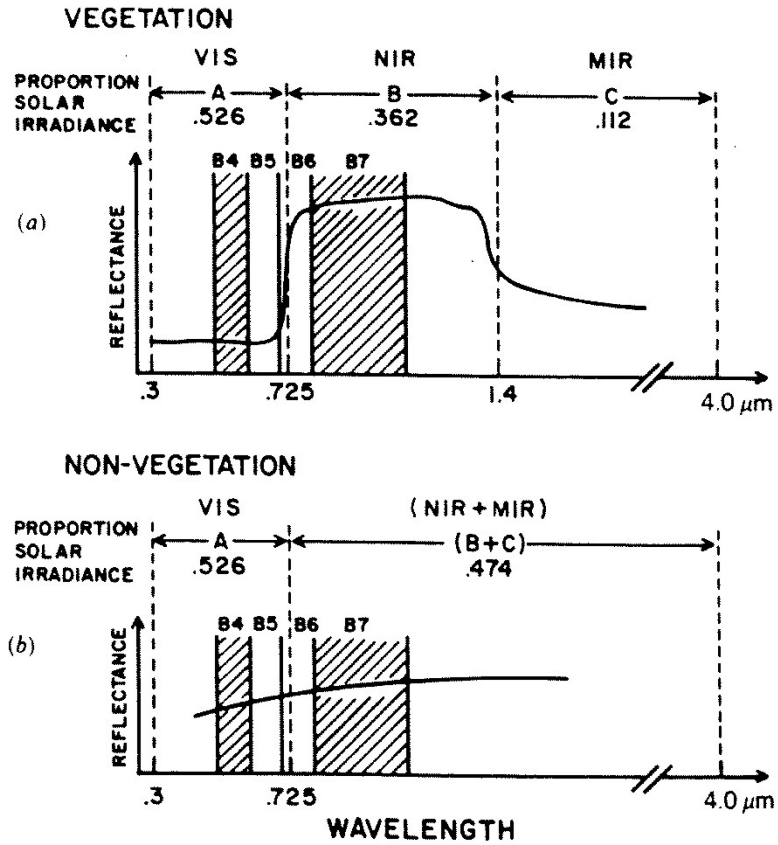


Figure 5.5: Simplified spectral reflectance curves for (a) vegetation and (b) non-vegetation surface showing location of Landsat bands and proportional weighting factors. Source: Brest and Goward (1987).

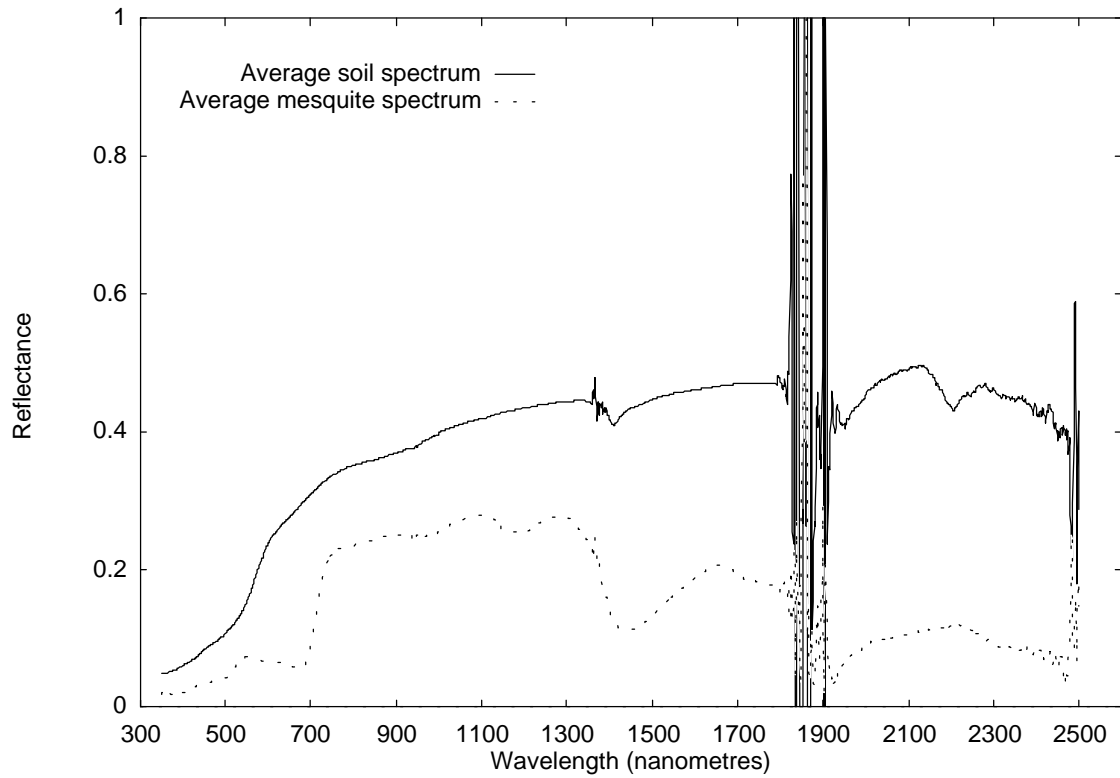


Figure 5.6: Reflectance spectra for mesquite live vegetation (mesquite) and soil recorded by Greg Asner (University of Colorado) using an ASD Fieldspec® FR Portable Spectroradiometer. Noise present in the spectra are caused by water absorption effects.

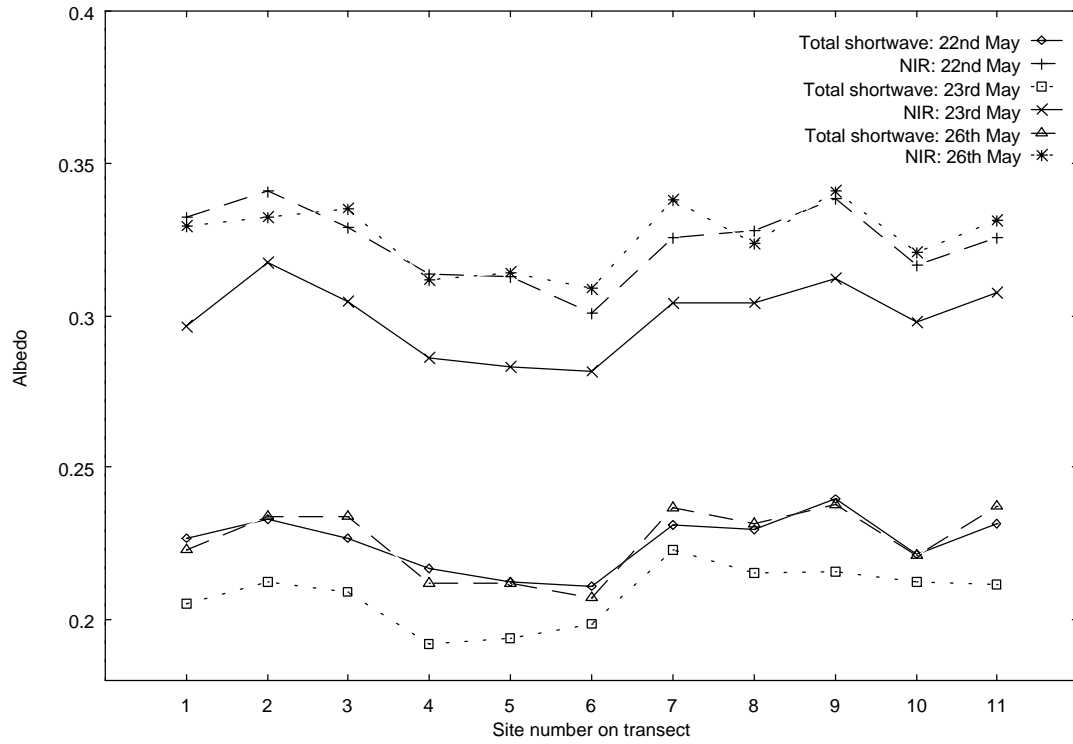


Figure 6.1: Total shortwave and NIR broadband, solar zenith angle corrected, albedo measurements along the north transect for the 22nd, 23rd and 26th May 1997.

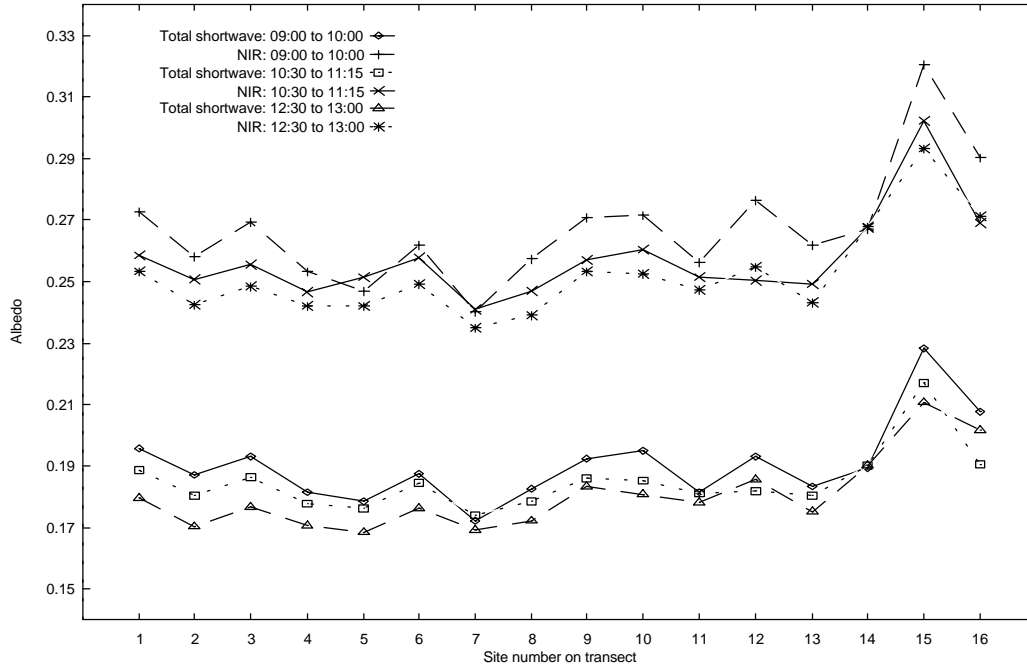


Figure 6.2(a): Total shortwave and NIR broadband albedo measurements without solar zenith angle correction along the grassland transect for three times on the 27th May 1997.

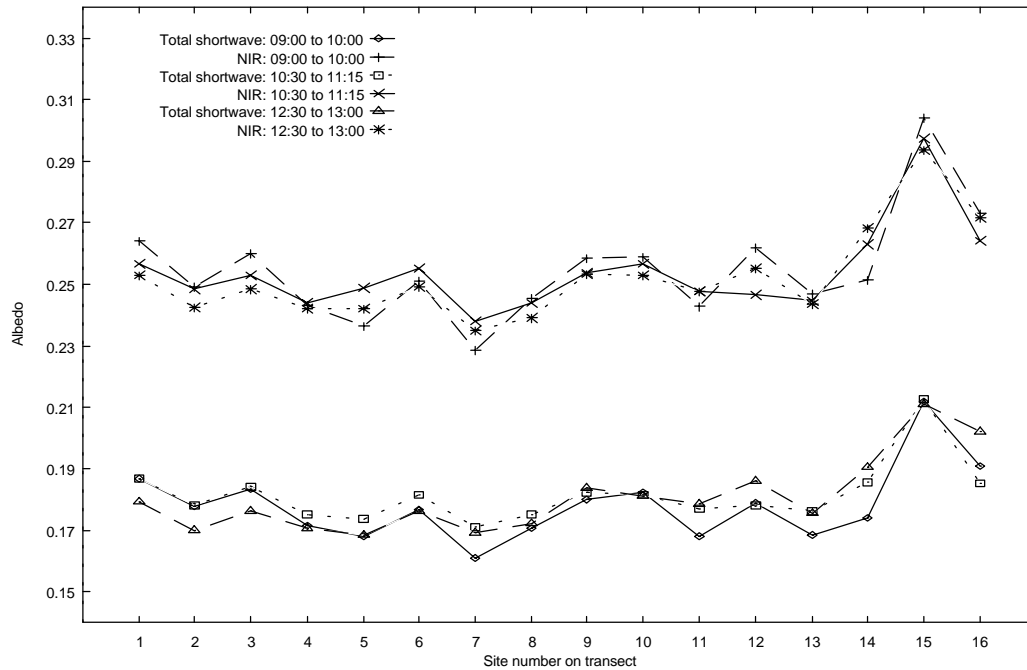
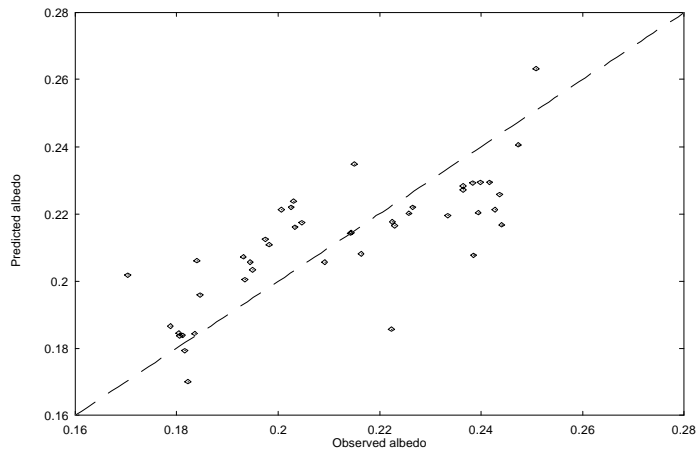
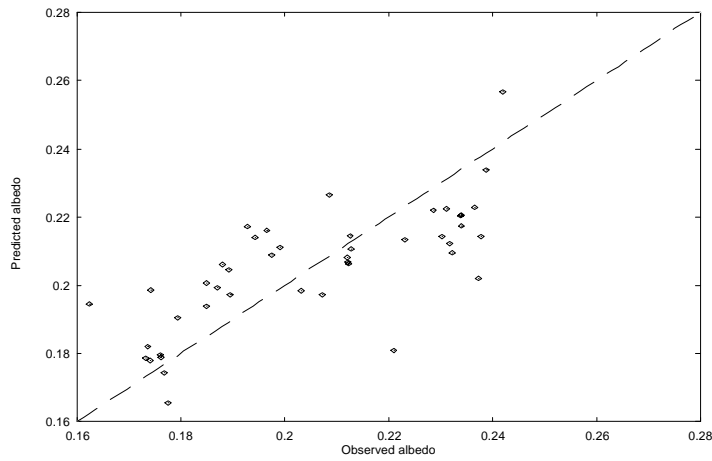


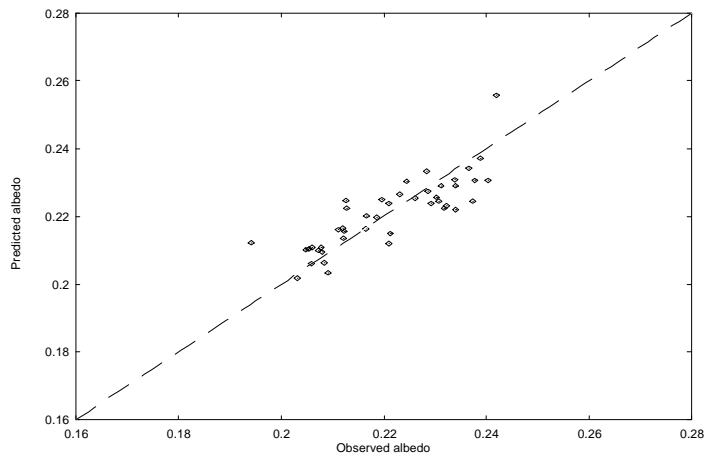
Figure 6.2(b): Total shortwave and NIR broadband, solar zenith angle corrected, albedo measurements along the grassland transect for three times on 27th May 1997.



(a)



(b)



(c)

Figure 6.3: Observed versus predicted values for total shortwave broadband albedo. (a) with corrections to observed values for solar zenith angle and soil moisture effects, (b) with corrections for solar zenith angle but not soil moisture effects, (c) with corrections for both solar zenith angle and soil moisture effects.

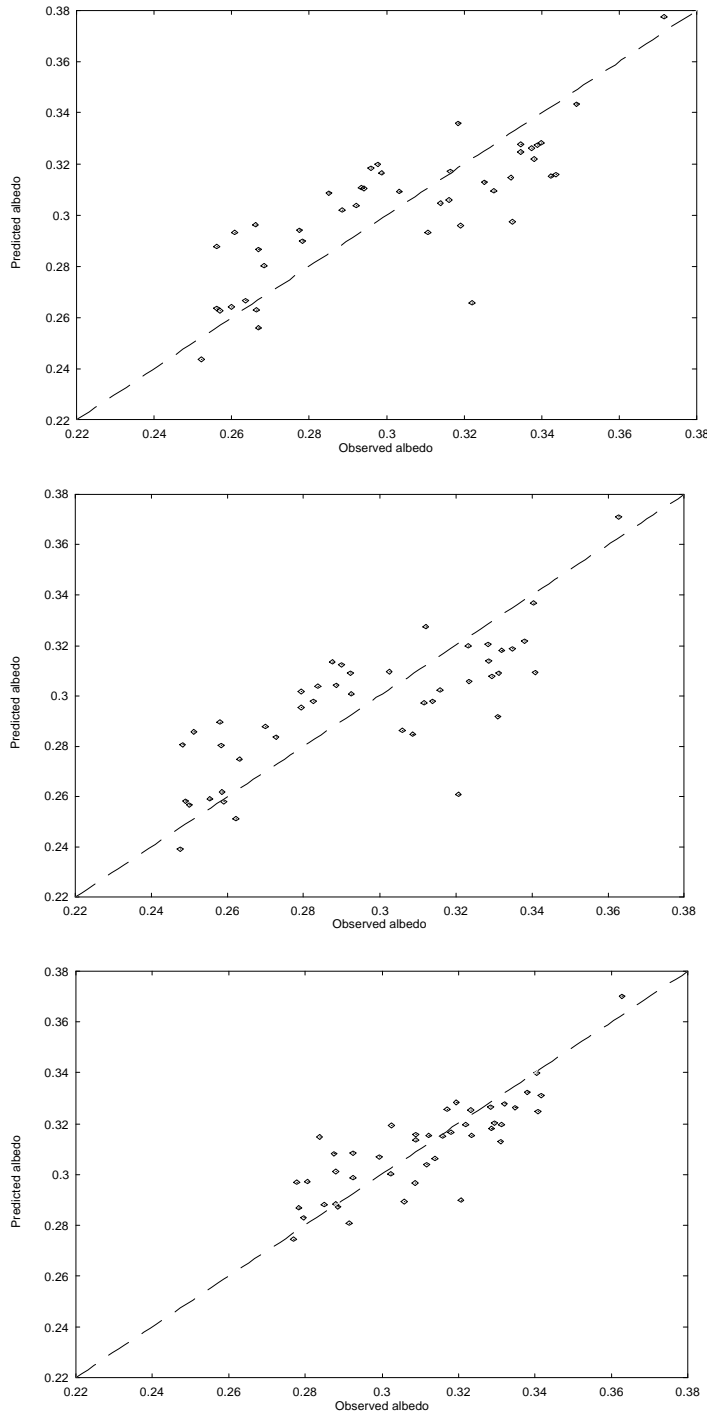


Figure 6.4: Observed versus predicted values for NIR broadband albedo. (a) with corrections to observed values for solar zenith angle and soil moisture effects, (b) with corrections for solar zenith angle but not soil moisture effects, (c) with corrections for both solar zenith angle and soil moisture effects.

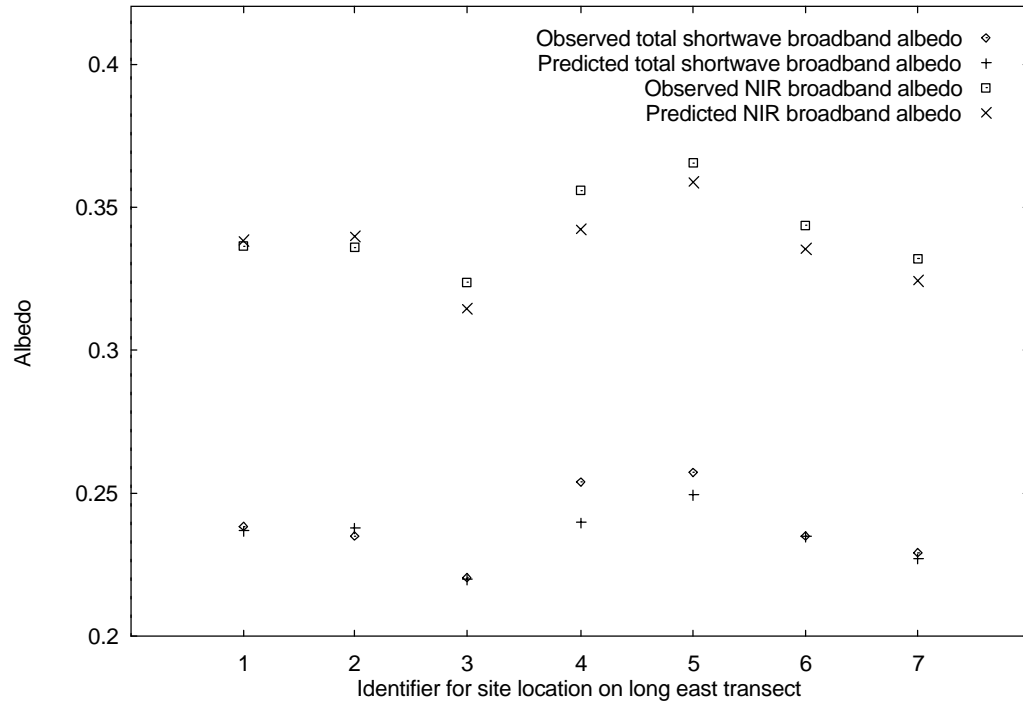


Figure 6.5: Observed and predicted values of total shortwave and NIR broadband albedo for seven locations at the end of a 1km transect to the east of the tower.

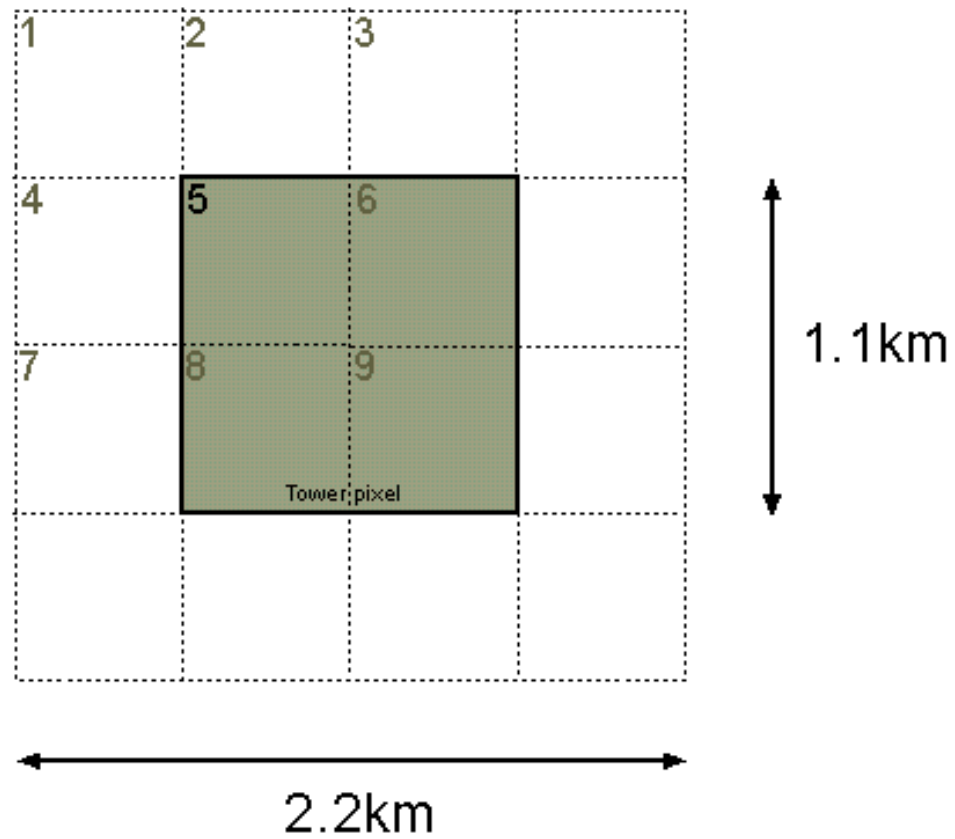


Figure 6.6: Identification of numbering of the nine 1.1km x 1.1km cells within a larger 2.2km x 2.2km area centered on the AVHRR pixel containing the tower. Cells are numbered at the upper left.

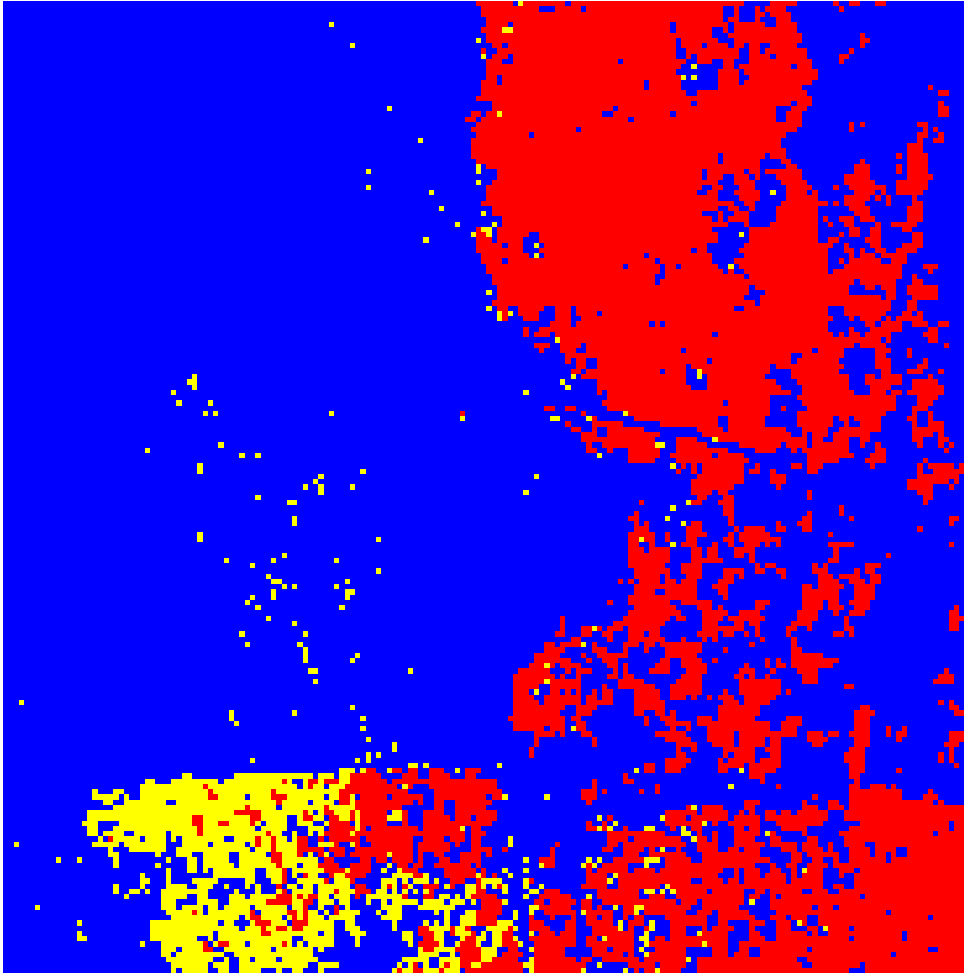


Figure 6.7: Classified 2.2km x 2.2km area centered on the AVHRR pixel containing the tower. The classification is performed on 12m resolution TMS data. The three classes are: blue: shrubs and soil, red: grass, yellow: grass and soil.

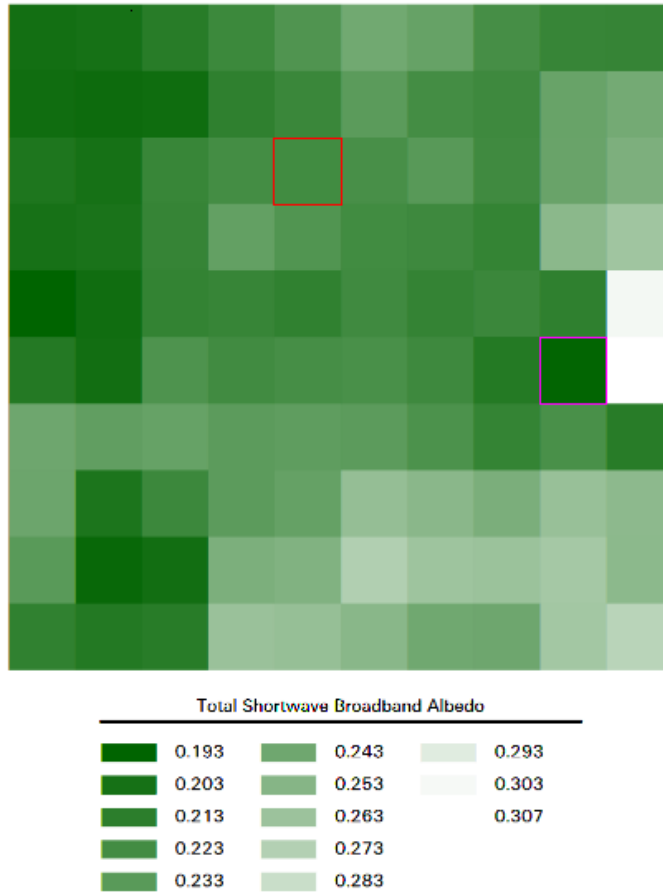


Figure 6.8: 10 x 10 1.1km x 1.1km AVHRR total shortwave albedo map. The pixel containing the tower is highlighted with a red border and the pixel which exhibits the most dominant grey vegetation / dormant grass cover is highlighted with a magenta border.

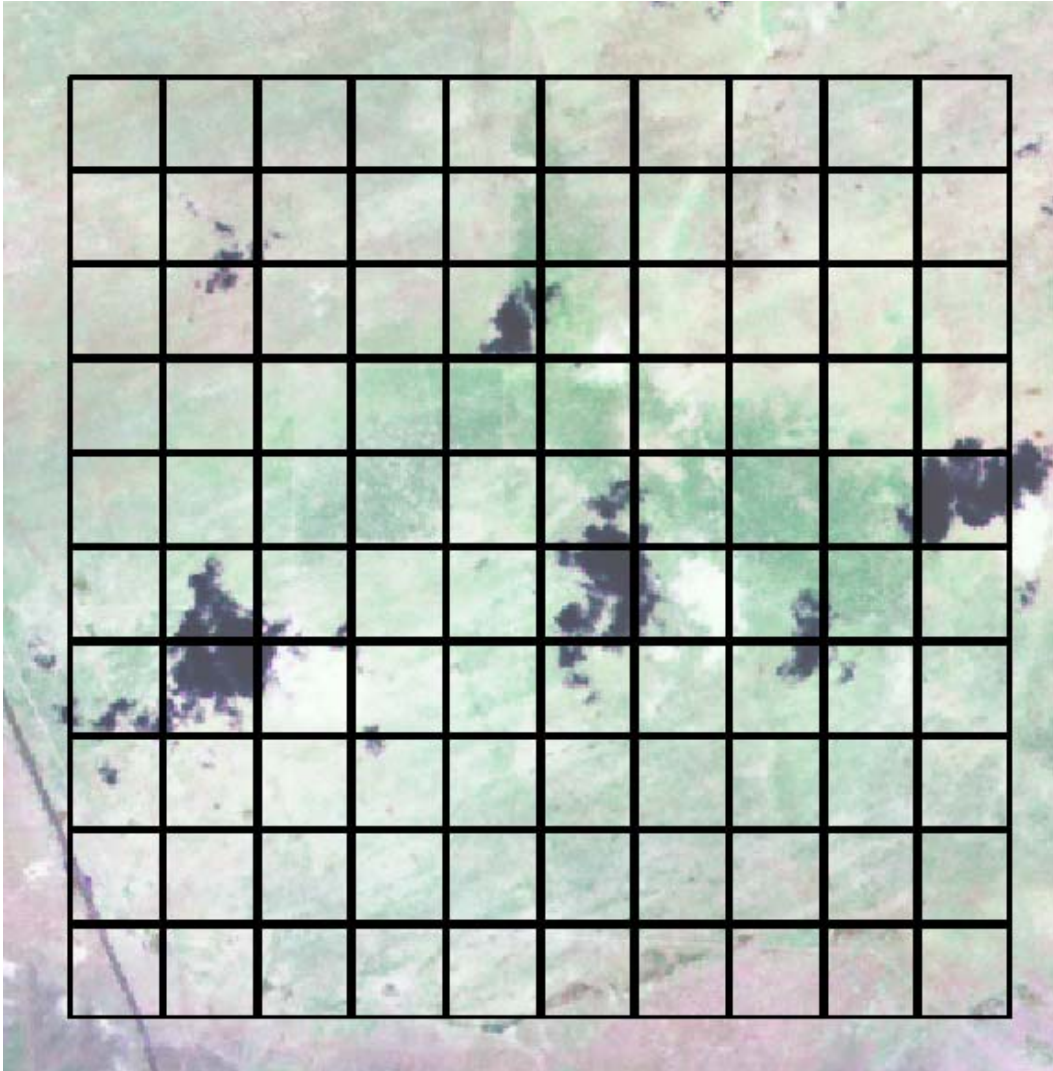


Figure 6.9: Landsat TM false colour composite, bands 4,5,3 with a 1.1km AVHRR grid overlayed. The pixel containing the tower is in the third row, fifth column from the top left, obscured by a cloud shadow.

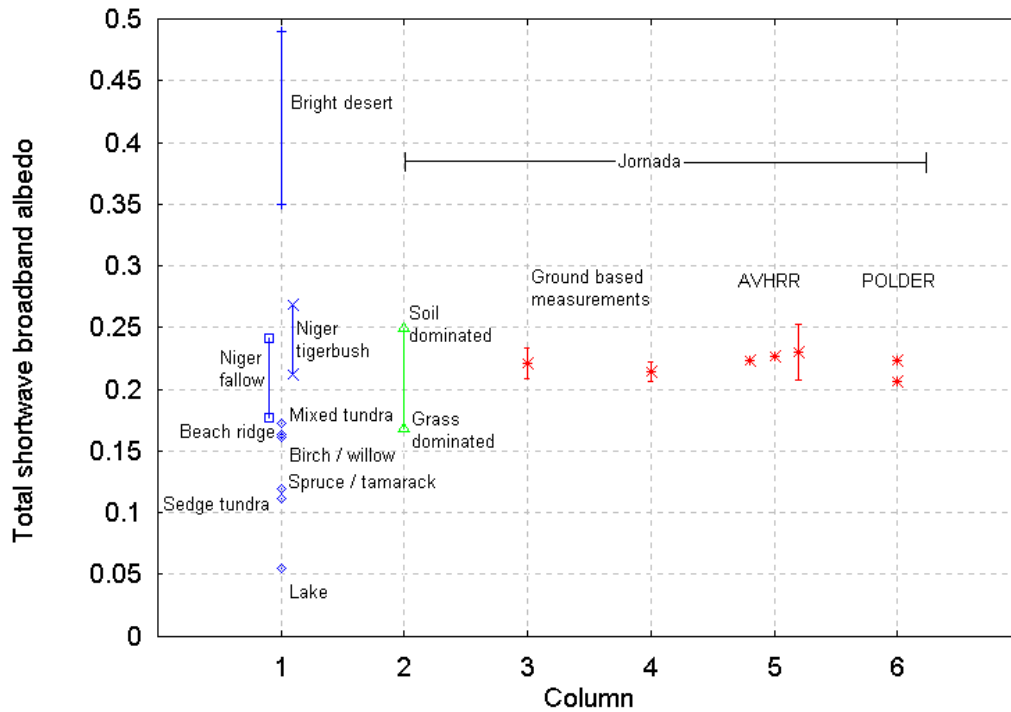


Figure 6.10: Summary graph of total shortwave broadband albedo at various spatial scales. Column 1 presents typical total shortwave broadband albedo values for a variety of surface types. Column 2 presents the range recorded at Jornada with sites that were soil dominated exhibiting the highest albedos and sites that were grey vegetation / dormant grass dominated the lowest. Columns 3 and 4 present albedos derived from ground measurements. Column 3 plots the mean of the 44 measurements on the short north, south, east and west transects and error bars representing one standard deviation. Column 4 presents albedo derived from 1.1km x 1.1km classified maps by assigning typical albedos to the land cover classes and weighting by their proportional cover. The error bars represent one standard deviation based on the sensitivity analysis to the location of the 1.1km x 1.1km area within a 2.2km x 2.2km area centered on the pixel containing the tower. Column 5 plots, from left to right, albedo derived through narrowband-to-broadband conversion for the AVHRR pixel containing the tower, a 2 x 2 block including the AVHRR pixel containing the tower, and the mean of the 10x10 AVHRR block with the error bars representing one standard deviation. The final column, 6, plots POLDER total shortwave broadband albedos with the lower value derived from estimating the spectral albedo profile through splining and the higher value through adjustment to fit the hyperspectral AVIRIS reflectance profile.

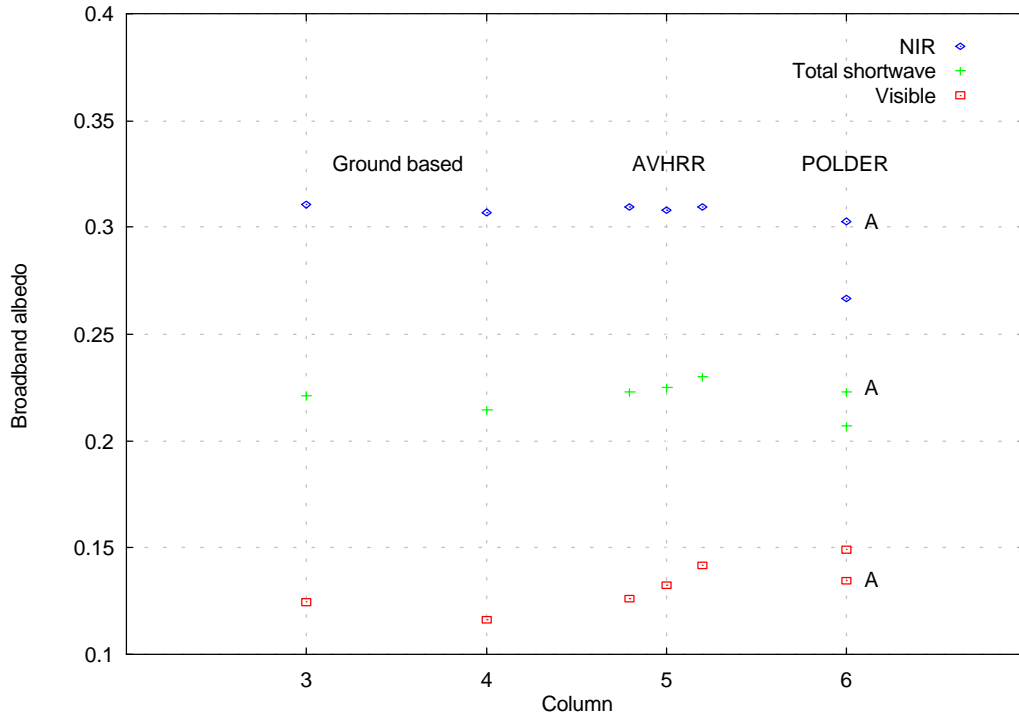


Figure 6.11: Total shortwave, visible and near-infrared broadband albedo at various spatial scales. Column numbering follows that established in *figure 6.10*. Columns 3 and 4 present albedos derived from ground measurements. Column 3 plots the mean of the 44 measurements on the short north, south, east and west transects while column 4 presents albedo derived from 1.1km x 1.1km classified maps by assigning typical albedos to the land cover classes and weighting by their proportional cover. Column 5 plots, from left to right, albedo derived through narrowband-to-broadband conversion for the AVHRR pixel containing the tower, a 2x2 block including the AVHRR pixel containing the tower, and the mean of the 10x10 AVHRR block. The final column, 6, plots POLDER total shortwave broadband albedos with the values derived through adjustment to fit the hyperspectral AVIRIS reflectance profile indicated by an “A”. The unmarked points are derived from estimating the spectral albedo profile through splining.

REFERENCES

Allen, S.J., Wallace, J.S., Gash, J.H.C and Sivakumar, M.V.K. 1994: Measurements of albedo variation over natural vegetation in the Sahel. *International Journal of Climatology*, 14, 625-636.

Analytical Spectral Devices, Inc. 1996: FieldSpec® FR measurements of spectral solar irradiance. [Online] Available: <http://www.asdi.com/apps/arm.html>

Barker Schaaf, C. and Strahler, A.H. 1994: Validation of bidirectional and hemispherical reflectances from a geometric-optical model using ASAS imagery and pyranometer measurements of a spruce forest. *Remote Sensing of Environment*, 49: 138-144.

Boer, K.W. 1977: The solar spectrum at typical clear weather days. *Solar Energy*, 19, 525-538.

Bouilanne, M., Nolette, C., Agnard, J.-P. and Brindamour, M. 1997: Hemispherical photographs used for mapping confined spaces. *Photogrammetric Engineering and Remote Sensing*, 63(9), 1103-1109.

Brest, C.L. and Goward, S.N. 1987: Deriving surface albedo measurements from narrow band satellite data. *International Journal of Remote Sensing*, 8(3), 351-367.

Brest, C.L. and Rossow, W.B. 1992: Radiometric calibration and monitoring of NOAA AVHRR data for ISCCP. *International Journal of Remote Sensing*, 13(2), 235-273.

Bruegge, C.J., Halthorne, R.N., Markham, B., Spanner, M. and Wrigley, R. 1992: Aerosol optical depth retrievals over the Konza Prairie. *Journal of Geophysical Research*, 97(D17), 18743-18758.

DeAbreu, R.A., Keu, J., Maslanik, J.A., Serreze, M.C. and LeDrew, E.F. 1994: Comparison of *in situ* and AVHRR-derived broadband albedo over Arctic sea ice. *Arctic*, 47(3), 288-297.

Deschamps, P-T., Bréon, F-M., Leroy, M., Podaire, A., Bricaud, A., Buriez, J-C. and Sèze, G. 1994: The POLDER mission: instrument characteristics and scientific objectives. *IEEE Transactions of Geoscience and Remote Sensing*, 32(3), 598-615.

Di, L. and Rundquist, D.C. 1994: A one-step algorithm for correction and calibration of AVHRR level 1b data. *Photogrammetric Engineering and Remote Sensing*, 60, 165-171.

Dick-Peddie, W.A. 1993: *New Mexico vegetation, past, present and future*. Albuquerque, NM: University of New Mexico Press. 244pp.

ERDAS 1997: *ERDAS Imagine V8.3 Tour Guides*. Atlanta, GA: ERDAS, Inc. 454pp.

Frew, J., 1990: The Image Processing Workbench. *PhD Thesis, Department of Geography, University of California, Santa Barbara, CA*, 382 pp.

Grainger, R.G, Basher, R.E. and McKenzie, R.L. 1993: UV-B Robertson-Berger meter characterization and field calibration. *Applied Optics*, 32(3), 343-349.

Haeffliger, M., Steffen, K., and Fowler, C. 1993: AVHRR surface temperature and narrow-band albedo comparison with ground measurements for the Greenland ice sheet. *Annals of Glaciology*, 17, 49-54.

Henderson-Sellers, A. and Wilson, M.F. 1983: Surface albedo for climate modeling. *Reviews of Geophysics*, 21, 1743-1778.,

Holben, B.N., Eck, T.F., Slutsker, I., Tanré, D., Buis, J.P., Setzer, A., Vermote, E., Reagan, J.A., Kaufman, Y.J., Makajima, T., Lavenu, F., Jankowiak, I., and Smirnov, A. 1998: AERONET - a federated instrument network and data archive for aerosol characterization. *Remote Sensing of Environment*, submitted.

Irons, J.R., Ranson, K.J. and Daughtry, C.S.T. 1988: Estimating big bluestem albedo from directional reflectance measurements. *Remote Sensing of Environment*, 25, 185-199.

Justice, C.O., Vermote, E., Townshend, J.R.G., Defries, R., Roy, D.P., Hall, D.K., Salomonson, V.V., Privette, J.L., Riggs, G., Strahler, A., Lucht, W., Myneni, R.B., Knyazikhin, Y., Running, S.W., Nemani, R.R., Wan, Z., Huete, A.R., van Leeuwen, W. Wolfe, R.E., Giglio, L., Muller, J-P., Lewis, P., and Barnsley, M.J. 1998: The Moderate Resolution Imaging Spectroradiometer (MODIS): land remote sensing for global change research. *IEEE Transactions on Geoscience and Remote Sensing*, 36(4), 1228-1249.

Kannenbergh, B. 1997: Grassland Prototype Validation Exercise (PROVE) at Jornada Experimental Range. *The Earth Observer*, 9(4), 16-18.

Kipp and Zoen, 1997: *Instruction manual CM11/14 Pyranometer*. Delft: Kipp and Zoen B.V.. 34pp.

Koepke, P. 1989: Removal of atmospheric effects from AVHRR albedos. *Journal of Applied Meteorology*, 28(12), 1341-1348.

Kriebel, K.T. 1978: Measured spectral bidirectional reflection properties of four vegetated surfaces. *Applied Optics*, 17, 253-259.

Lafleur, P.M., Wurtele, A.B. and Duguay, C.R. 1997: Spatial and temporal variations in surface albedo of a subarctic landscape using surface-based measurements and remote sensing. *Arctic and Alpine Research*, 29(3), 261-269.

Laine, V. and Heikinheimo, M. 1996: Estimation of surface albedo from NOAA AVHRR data in high latitudes. *Tellus*, 48A, 424-441.

Lewis, P. 1995: The utility of kernel-driven BRDF models in global BRDF and albedo studies. In, *Proceedings of 1995 International Geoscience and Remote Sensing Symposium (IGARSS95)*, 10-14 July 1995, Firenze, Italy. Piscataway, NJ: IEEE Geoscience and Remote Sensing Society, 1186-1188.

Lewis, P. and Barnsley, M.J. 1994: Influence of the sky radiance distribution on various formulations of earth surface albedo. In, *Proceedings of the 6th International Symposium on Physical Measurements and Spectral Signature in Remote Sensing. 17-24 January 1994, Val d'Iserre, France*. ISPRS Commission VII, 707-713.

Lewis, P., Disney, M.I., Barnsley, M.J. and Muller, J.-P. 1998: Deriving albedo for HAPEX-Sahel from ASAS data using kernel-driven BRDF models. *Hydrology and Earth System Sciences*, in press.

Li, Z.Q. and Garand, L. 1994: Estimation of surface albedo from space - a parameterization for global application. *Journal of Geophysical Research - Atmospheres*, 99(D4), 8335-8350.

Liang, S., Strahler, A.H. and Walthall, C. 1998: Retrieval of land surface albedo from satellite observations: a simulation study. *Journal of Applied Meteorology*, in press.

Markham, B.L. and Barker, J.L. 1985: Spectral characterization of the LANDSAT Thematic Mapper sensors. *International Journal of Remote Sensing*, 6(5), 697-716.

Minnis, P., Mayor, S., Smith, W.L., and Young, D.F. 1997: Asymmetry in the diurnal variation of surface albedo. *IEEE Transactions on Geoscience and Remote Sensing*, 35(4), 879-891.

Ohmura, A. And Gilgen, H. 1993: Re-evaluation of the global energy balance. In, McBean, G.A. and Hantel, M. (Eds) *Interactions between global climate subsystems: the legacy of Hann*, *Geophysics Monograph Series*, Washington D.C.: American Geophysical Union, 75, 93-110.

Popp, T. 1995: Correcting atmospheric masking to retrieve the spectral albedo of land surfaces from satellite measurements. *International Journal of Remote Sensing*, 16(18), 3483-3508.

Privette, J.L., Justice, C.O. and Running S.W. 1997a: *MODIS Land Validation Plan: MODIS Land Discipline Team*. [Online] Available: <http://eosps0.gsfc.nasa.gov/validation/valplans.html>, 23pp.

Privette, J.L., Eck, T.F and Deering, D.W. 1997b: Estimating spectral albedo and nadir reflectance through inversion of simple BRDF models with AVHRR/MODIS-like data. *Journal of Geophysical Research*, 102(D24), 29529-29542.

Rahman, H., Pinty, B. and Verstraete, M.M. 1993: Coupled surface-atmosphere reflectance (CSAR) model, 2, semiempirical surface model usable with NOAA Advanced Very High Resolution Radiometer data. *Journal of Geophysical Research*, 98, 20791-20801.

Rahman, F. , van Leeuwen, W., Privette, K., Wanner, W. and Asner, G. 1997: *La Jornada Prototype Validation Experiment, May 1997 (PROVE '97)*. NASA GFSC: Experimental plan, working document.

Ranson, K.J., Irons, J.R. and Daughtry, C.S.T. 1991: Surface albedo from bidirectional reflectance. *Remote Sensing of Environment*, 35(2-3), 201-211.

Rao C.R.N. and Chen, J. 1995: Inter-satellite linkages for the visible and near-infrared channels of the Advanced Very High Resolution Radiometer on the NOAA-7, -9 and -11 spacecraft.

International Journal of Remote Sensing, 16(11) 1931-1942.

Rao, C.R.N. and Chen, J. 1996: Post-launch calibration of the visible and near-infrared channels of the Advanced Very High Resolution Radiometer on the NOAA-14 spacecraft. *International Journal of Remote Sensing*, 17(14), 2743-2747.

Research System, Inc. 1995: *IDL user's guide, interactive data language, version 4*. Boulder, CO: Research Systems, Inc.

Rich, P.M. 1990:, Characterising plant canopies with hemispherical photographs. *Remote Sensing Reviews*, 5(1), 13-29.

Richards, J.A. 1993: *Remote Sensing Digital Image Analysis: An Introduction*. London: Springer-Verlag. 340pp.

Roujean, J.L., Leroy, M. and Deschamps, P.Y. 1992: A bidirectional reflectance model of the Earth's surface for the correction of remote sensing data. *Journal of Geophysical Research*, 97, 20455-20468.

Saunders, R.W. 1990: The determination of broad band surface albedo from AVHRR visible and near-infrared radiances. *International Journal of Remote Sensing*, 11, 49-67.

SAS Institute Inc. 1989: *SAS/STAT User's Guide, Version 6, Fourth Edition*. Cary NC: SAS Institute Inc. 1789pp.

Sellers, P.J. 1993: Remote sensing of the land surface for studies of global change. *NASA / GSFC International Satellite Land Surface Climatology Project Report*, Columbia, MD.

Sokal, R.R. 1973: *Introduction to biostatistics*. San Francisco, CA: W.H. Freeman. 368pp.

Starks, P.J., Norman, J.M, Blad, B.L., Walter-Shea, E.A. and Walthall, C.L. 1991: Estimation of shortwave hemispherical reflectance (albedo) from bidirectionally reflected radiance data. *Remote Sensing of Environment*, 38(2), 123-134.

Strahler, A.H., Wanner, W., Schaaf, C.B., Li, X., Hu, B., Muller, J.-P., Lewis, P. and Barnsley, M.J. 1996: *MODIS BRDF / Albedo product: algorithm theoretical basis document version 4.0*. MODIS Product ID: MOD43.

Stroeve, J., Nolin, A. and Steffen, K. 1997: Comparison of AVHRR-derived and in-situ surface albedo over the Greenland ice sheet. *Remote Sensing of Environment*, 62(3), 262-276.

Trimble Navigation Limited 1996a: *GeoExplorer II operation manual*. Sunnyvale, CA: Trimble Navigation Limited.

Trimble Navigation Limited 1996b: *Pathfinder Office Software Volume I*. Sunnyvale, CA: Trimble Navigation Limited.

Vane, G., Green, R.O., Chrien, T.G., Enmark, H.T., Hansen, E.G. and Porter, W.M. 1993: The Airborne Visible/Infrared Imaging Spectrometer (AVIRIS), *Remote Sensing of Environment*, 44, 127-143.

Vermote, E.F., Tanre, D., Deuze, J.L., Herman, M. and Morcrette, J.-J. 1997: Second simulation of the satellite signal in the solar spectrum, 6S: an overview. *IEEE Transaction of Geoscience and Remote Sensing*, 35(3), 675-686.

Wanner, W., Strahler, A.H., Hu, B., Lewis, P., Muller, J.-P., Li, X., Barker Schaaf, C.L. and Barnsley, M.J. 1997: Global retrieval of bidirectional reflectance and albedo over land from EOS MODIS and MISR data: theory and algorithm. *Journal of Geophysical Research*, 102(D14), 17143-17161.

Woodcock, C.E., Collins, J., Jakabhazy, V. and Macomber, S. 1993: *Technical Manual: Forest Vegetation Mapping Methods for Region 5 of the US Forest Service*. Boston University Center for Remote Sensing, Technical Paper Number 7, 105pp.

Zhang Y.-C., Rossow, W.B. and Lacis, A.A. 1995: Calculation of surface and top of atmosphere radiative fluxes from physical quantities based on ISCCP data sets. 1, Method and sensitivity to input data uncertainties. *Journal of Geophysical Research*, 100, 1149-1165.